Optoelectronic processes in 2D semiconductors and van der Waals interfaces

Ponomarev, Evgeniy

How to cite

PONOMAREV, Evgeniy. Optoelectronic processes in 2D semiconductors and van der Waals interfaces. Doctoral Thesis, 2019. doi: 10.13097/archive-ouverte/unige:129429

This publication URL: https://archive-ouverte.unige.ch/unige:129429
Publication DOI: 10.13097/archive-ouverte/unige:129429

UNIVERSITÉ DE GENÈVE FACULTÉ DES SCIENCES
DQMP AND GAP PROFESSEUR ALBERTO F.MORPURGO

Optoelectronic Processes in 2D Semiconductors and van der Waals Interfaces

THÈSE

présentée à la Faculté des Sciences de l'Université de Genève
pour obtenir le grade de Docteur ès Sciences, mention Physique

par

Evgeniy Ponomarev

de Vladimir, Russie

Thèse N° 5371

GENÈVE
Atelier d'impression ReproMail
2019

UNIVERSITÉ
DE GENÈVE
FACULTÉ DES SCIENCES

DOCTORAT ÈS SCIENCES, MENTION PHYSIQUE

Thèse de Monsieur Evgeniy PONOMAREV

intitulée :

«Optoelectronic Processes in 2D Semiconductors and van der Waals Interfaces»

La Faculté des sciences, sur le préavis de Monsieur A. MORPURGO, professeur ordinaire et directeur de thèse (Département de physique de la matière quantique), Monsieur C. RENNER, professeur ordinaire (Département de physique de la matière quantique), Monsieur T. MUELLER, professeur (Institute of Photonics, Vienna University of Technology, Austria) et Monsieur M. POTEMSKI, docteur (Laboratoire National des Champs Magnétiques Intenses - Grenoble, France), autorise l'impression de la présente thèse, sans exprimer d'opinion sur les propositions qui y sont énoncées.

Genève, le 23 juillet 2019

Thèse - 5371 -

Le Doyen

N.B. - La thèse doit porter la déclaration précédente et remplir les conditions énumérées dans les "Informations relatives aux thèses de doctorat à l'Université de Genève".

Résumé

L'isolation d'une couche de graphite d'un atome d'épaisseur, très bien connue aujourd'hui sous le nom de *graphène*, realisée par A.Geim et K. Novoselov (prix Nobel de physique 2010) en 2004, a été une véritable avancée révolutionnaire qui a ouvert un nouveau domaine de recherche et a eu un impact important sur de nombreux domaines allant de la physique de l'état solide à la cosmologie en passant par la chimie des surfaces. La principale raison pour laquelle un morceau de carbone obtenu avec cette technique, que même un élève du secondaire peut facilement maîtriser, a suscité tant d'attention, c'est qu'il permet d'étudier la matière à une échelle réellement 2D, ce qui n'avait jamais été atteint auparavant.

Le graphène est un allotrope 2D de carbone dans lequel les atomes sont disposés dans un plan de l'épaisseur d'un atome et organisés sur une structure en nid d'abeille. Le graphène et sa version multicouche, le graphite, appartiennent à la famille de matériaux dits de van der Waals (vdW). Ces matériaux sont composés de couches atomiquement minces qui sont maintenues ensemble par des forces de vdW très faibles. Dans chaque couche, cependant, les atomes sont étroitement liés par de fortes liaisons covalentes. Cette structure permet de cliver facilement ces matériaux en brisant les liaisons de vdW entre couches tout en laissant pratiquement intact la disposition des atomes dans chaque couche. De manière plus frappante, en principe, pour effectuer un tel clivage, aucun équipement sophistiqué n'est requis et cela peut facilement être réalisé en utilisant un rouleau de ruban adhésif. De plus, les liaisons intercouches vdW sont la raison pour laquelle une couche de matériau atomiquement mince est stable dans les conditions ambiantes et préserve sa composition chimique. La rupture des liaisons de vdW n'affecte en aucun cas la surface d'une couche 2D; elle reste donc chimiquement inerte et ne subit aucune dégradation. Une méthode de synthèse simple et robuste associée à la vitalité exceptionnelle du graphène sont les facteurs clés du boom des matériaux 2D.

La famille des matériaux 2D vdW n'est de loin pas limitée au graphène. C'était le premier, mais peu de temps après, une pléthore d'autres matéri-

aux s'est rapidement épanouie. Ces matériaux diffèrent sensiblement les uns des autres en termes de propriétés et de domaines d'applications potentielles. Parmi les plus étudiés figurent des isolants tels que le nitrure de bore hexagonal (h-BN), des semiconducteurs comprenant un groupe important de dichalcogénures de métaux de transition, des semimétaux représentés par le graphène ou WTe_2, ou encore des supraconducteurs tels que $NbSe_2$. Une telle variété de propriétés, appartenant à une classe de matériaux, est très prometteuse pour le développement de nouvelles technologies. Par exemple, disposer des trois composants principaux d'un transistor à effet de champ (c'est-à-dire un métal, un isolant et un semiconducteur) permet de construire des circuits intégrés entièrement à partir de matériaux 2D pouvant potentiellement concurencer la technologie du silicium qui prochainement atteindra sa limite et ne pourra plus suivre la loi de Moore.

La réduction de la dimensionnalité des matériaux de la 3D à la 2D entraîne des modifications qualitatives des propriétés des matériaux et l'émergence d'une nouvelle physique. L'exemple très connu est la quantification des niveaux d'énergie d'un matériau provoquée par le confinement spatial du mouvement des électrons le long d'une des dimensions du matériau. Cet effet se manifeste par l'apparition de niveaux d'énergie discrets dans la structure de bande électronique d'un matériau. Un autre exemple est la quantification de la conductance transverse, connue sous le nom d'effet quantique de *Hall* (K. Von Klitzing, prix Nobel de physique 1985). Pour les semiconducteurs, la transition de la 3D à la 2D a également des implications importantes. Par exemple, dans les semiconducteurs, les électrons chargés négativement et leurs homologues de charge positive, les trous, peuvent se lier par des interaction Coulombiennes, formant des quasi-particules à charge neutre, appelées *excitons*. Ces quasiparticules présentent un grand intérêt, par exemple dans la réalisation d'états quantiques cohérents, e.g. formation de condensat d'excitons de Bose-Einstein. Dans les semiconducteurs 3D, les électrons et les trous de ces paires sont généralement très faiblement liés, car le potentiel de Coulomb qui les maintiennent ensemble est considérablement affecté par la masse environnante, ce qui réduit leur durée de vie et limite leur utilisation à des fins de recherche. Dans le cas 2D, cependant, le potentiel de Coulomb est beaucoup moins affecté et la liaison de la paire électron-trou est fortement améliorée. L'énergie de liaison de ces excitons peut atteindre 0.5 eV, ce qui permet leur observation même à température ambiante.

Cette thèse se concentre sur les propriétés électroniques et optiques des semiconducteurs 2D de vdW et de leurs hétérostructures. En particulier, une grande partie de nos travaux est basée sur des expériences menées sur des couches atomiquement minces de dichalcogénures de métaux de transition du groupe 6 et de leur membre le plus étudié MoS_2 . Les propriétés de transport électronique de ces matériaux sont principalement étudiées à l'aide de grille électrique à base de liquide ionique. Dans cette technique, un matériau est intégré dans un transistor à effet de champ, dont le diélectrique de grille est un liquide ionique (connu sous le nom anglais de "ionic-liquid gate field effect transistor (IL FET)"), dans lequel la réponse du matériau est sondée en fonction de la tension de grille appliquée. L'utilisation d'une grille avec IL est particulièrement adapté à l'étude de matériaux 2D et permet de mesurer des caractéristiques telles que l'amplitude de la bande interdite de semiconducteurs dans la description de particule unique ou l'alignement de bande dans des hétérostructures semiconductrices. Les IL FET permettent également d'étudier les propriétés des matériaux sous une densité de porteurs de charge élevée, ce qui permet de sonder l'interaction électron-phonon dans les semiconducteurs 2D. De plus, les IL FET offrent la possibilité de réaliser des dispositifs fonctionnels tels que des transistors émetteurs de lumière ou des photodétecteurs, fréquemment utilisés au cours de nos travaux. Enfin, nous profitons de la flexibilité offerte par les matériaux van-der-Waals dans l'assemblage d'hétérostructures avec des propriétés réglables. En choisissant une combinaison appropriée de matériaux 2D, nous sommes capables de créer de nouveaux semiconducteurs artificiels avec l'amplitude et la nature de la bande interdite (directe ou indirecte) déterminée par conception.

Acknowledgements

It was long five years of my life a good part of which I dedicated to my phd work here in Geneva. It was a truly diverse journey full of ups and downs. Nowadays, doing research in experimental solid-state physics and particularly in the field of 2-dimensional materials can be rather tedious, arduous and by far not always intellectually rewarding job. Therefore, for the next generations of phd students I strongly suggest to think twice or even thrice before pursuing their studies in this direction. At the same time, I encourage a potential phd candidate who is strongly passionate about this domain, once entered, to be decisive enough to successfully complete his/her studies and not to withdraw in the middle.

At any rate, there were a number of people genuinely helping and supporting me all the way to my thesis defense whom I would like to warmly thank here. I would like to start with acknowledgments on the professional side (*i.e.,* people who supervised me and with whom I directly worked in the lab). First of all, I would like to thank Prof. Alberto Morpurgo for providing me the opportunity to do my thesis research here in Geneva. His constant rigorous supervision was definitely a key driver of my work in the lab. I would also like to mention Alberto's passionate and uncompromising (sometimes a bit too much) approach in doing research and writing scientific articles. Certainly, word constructions like "the mind of the reader" and "the referee will *cause a lot of problems to us*" will follow me for a long time. Next, I would like to thank Prof. Christophe Berthod who helped me to fill the gap in my formation in solid-state physics and prepared me for the candidacy exam. I am also grateful for Prof. Christoph Renner with whom I had a chance to work on a common project in scanning tunnelling microscopy and who also participated in the evaluation of my phd thesis. As for the committee members for my thesis defense, I would like to thank Dr. Marek Potemski and Prof. Thomas Mueller for their detailed and rigorous evaluation of the thesis manuscript and very friendly and fruitful discussion during the thesis defense.

I am incredibly grateful to the people with whom I worked directly in the lab doing experiments and from whom I have learned a lot. I was very lucky to collaborate on, actually, all my projects with Nicolas Ubrig – the master of the optical lab and by far not only. The majority of my knowledge in semiconductor optics is coming from Nicolas. I truly admire Nicolas' genuine urge to do research for the sake of pure science and not being obscured by any other poorly related needs. Furthermore, his continuous help in all stages of my phd research essentially enabled me to complete my degree. Another person who will never let you down and from whom you will always receive support in the lab is Ignacio Gutiérrez-Lezama (Nacho). I think it is more a part of Nacho's personality to help people and feel the responsibility for his younger colleagues. I am very grateful to Nacho for giving me a hand with writing scientific articles and with electronic transport measurements. Thank you, Nacho! I would also like to thank Aditya Reddy for his support with measurement systems and Hugo Henck for his help with the artwork. And, of course, all the members of our group for, basically, everything. On the personal side... The personal side I would like to keep it for me and say it in person, well, you know me, my dear reader. Anyway, I would like to thank my Mom (Anna) and Dad (Konstantin), and Yulia.

Contents

Chapter 1: Introduction

1.1 2D materials and van der Waals heterostructures

The isolation of single-atom-thick layer of graphite, very well known now as *graphene*, done by A.Geim and K.Novoselov (Nobel prize in physics 2010) in 2004[1] was a truly revolutionary breakthrough which opened up a new field of research and had a pronounced impact on multiple domains ranging from solid state physics and surface chemistry up to cosmology. This discovery was particularly outstanding because back at that time at the 2D limit graphite crystals were predicted to be thermodynamically unstable and hence not existing in nature. Nevertheless, several pioneering experimental works[2,3] demonstrated the opposite and since then research on graphene and other 2D materials has been thriving for almost 15 years and producing about ten thousand scientific publications every year.

The main reason why a piece of carbon obtained with the technique, which even a middle-school student can easily master, attracted so much attention is that it provided the possibility to study matter at the truly 2D length scale which was not attainable ever before. Structures replicating the behaviour of a 2D system have been previously known for several decades. For example, a 2-dimensional electron gas (2DEG), a system where electrons are tightly confined along one dimension and free to move along the other two, had been realized at the interfaces between a semiconductor and an insulator in field-effect transistors[4] in the 1960s, between two different semiconductors in quantum well structures[5,6] in the 1970s and between two different insulators from oxide electronics family[7] in the early 2000s. In all these cases, however, 2D-like behaviour persists only by bringing into contact two or more materials in composite structures, called *heterostructures*. Such a quasi-2D state exists only at the interfaces between 3-dimensional materials and cannot be observed separately from them. In contrast, truly 2D materials and graphene in particular are single component materials which are interfaces to themselves.

What is so special about graphene that ensured its incredible success? Graphene and its multilayered version graphite are members of the so-called van der Waals family of materials. These materials are composed of atomically-thin layers which are held together by very weak van der Waals forces. Within a single layer, however, atoms are tightly bonded by strong covalent bonds. This structure enables to easily cleave these materials across interlayer vdW bonds while leaving the arrangement of atoms within a layer virtually intact. More strikingly, in principle to perform such cleavage no sophisticated equipment is required and the main component that stood behind this astonishing discovery – apart from obviously strong scientific intuition and enormous dedication of graphene pioneers – was a roll of scotch tape – an ordinary consumable present in every office. A piece of graphite stacked between two scotch ribbons can be thinned down to monolayer thickness by multiple sequential attaching and detaching of one of the scotch ribbons. This method, coined as *scotch-tape exfoliation*, is incredibly simple and reproducible which determined such rapid development and expansion of the field of 2D vdW materials. Moreover, vdW interlayer bonds are the reason why an atomically thin layer of material is stable at the ambient conditions and preserves its chemical composition. Breaking vdW bonds do not affect anyhow the surface (*e.g.* do not create dangling bonds) of a 2D layer and therefore it remains chemically inert and does not experience any degradation. Robust and straightforward synthesis method together with graphene‘s outstanding vitality are the key factors behind the 2D materials boom.

The family of 2D vdW materials is by far not only limited to graphene. It was the first one but shortly after a plethora of other materials rapidly flourished. According to recent theoretical calculations[8] about 1800 compounds are thermodynamically stable and can be exfoliated from bulk crystals. These materials substantially differ from each other in terms of properties and domains of potential applications. Among the most studied ones are insulators such as hexagonal boron nitride (h-BN)[9], semiconductors including a large group of transition metal dichalcogenides[10], semimetals represented by graphene or WTe_2[11], superconductors such as $NbSe_2$[12]. Such a variety of properties reached within one class of materials holds a great promise for the development of new disruptive technologies. For example, having available all three principal components of a field-effect transistor (*i.e.,* a metal, an insulator, and a semiconductor) enables to build integrated circuits completely out of 2D materials which can potentially challenge the silicon technology which in a very recent future will reach its limit and will no longer be able to follow the Moore‘s law.

Reduction of material dimensionality from 3D to 2D leads to the qualitative changes of material properties and the emergence of new physics. The very well known example is the quantization of energy levels of a material caused by spatial confinement of electron motion along one of material dimensions. This effect is manifested in the appearance of discrete energy levels in the electronic band structure of a material seen in both quasi-2D systems like III-V quantum wells[13] and in 2D vdW layers[14,15]. Another example is the quantization of transversal conductance, known as *quantum Hall effect*, first also seen in quasi-2D structures[16] (K. von Klitzing, Nobel prize in physics 1985) and then observed in graphene[2,3,17] and other 2D materials[18]. Apart from these common effects of dimensionality reduction, graphene also has a unique property stemming from its linear low-energy dispersion relation $E(k)$. It accounts for the first experimental observation of massless Dirac fermions[2,3] which resembles the behaviour of relativistic particles in quantum electrodynamics.

For semiconductors the transition from 3D to 2D also has important implications. For example, in semiconductors a negatively charged electrons and their positively charged counterparts, holes, can bound through Coulomb interaction into charge-neutral quasiparticles, known as *excitons*[13]. These quasiparticles are of high interest, for example, for realization of coherent quantum states, *e.g.* Bose-Einstein condensate of excitons[19]. In 3D semiconductors electron and hole in such pair are typically very weakly bounded as the Coulomb potential holding them together is significantly screened by the surrounding bulk reducing their lifetimes and limiting their research use. In the 2D case, however, the Coulomb potential is screened much less and the bonding in the electron-hole pair is largely enhanced[20]. The binding energy of these excitons can be as large as 0.5 eV[21] which enables their observation even at room temperature.

Weak interlayer van der Waals forces is the key factor which enables isolation of atomically thin layers from bulk crystals. It also determines another prominent advantage that these materials offer – the possibility to build *van-der-Waals heterostructures*[22,23]. The ease with which an atomically-thick layer is detached from its bulk also implies that it can be further readily re-stacked on top of another vdW layer. In conventional heterostructures (*e.g.* III-V quantum wells, LAO/STO) strong covalent interlayer bonds allow to assemble together only materials with the same crystalline lattices and matching lattice constants greatly reducing the variety of combinations. Van der Waals bonding, however, induces no limitation on the parameters of materials which can be used in a heterostructure. It implies that all compounds from the rich library of vdW materials can be combined together which opens up immense opportunities for material property engineering. For example, the electronic band structure of graphene can be modified by putting it on-top of h-BN[24–26] or superconductivity can be induced to graphene by stacking two layers of graphene under the specific ’magic’ twist angle[27]. For heterostructures assembled from semiconductors the value of the heterostructure band gap as well as their optical properties can be varied in a large range by interchanging heterostructure constituents[28,29]. VdW heterostructures are a very powerful and flexible platform offering unprecedented opportunities to study new physical phenomena.

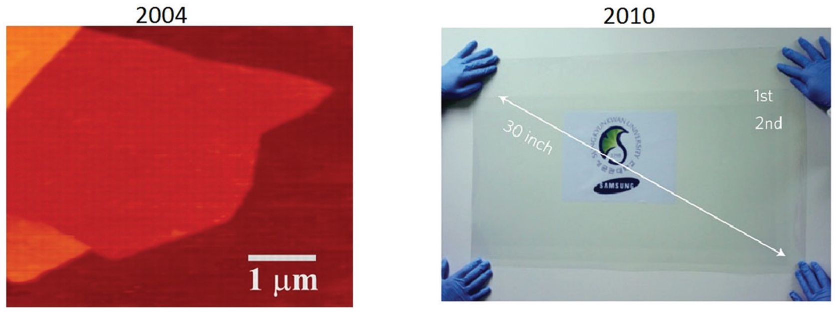

Figure 1.1: Evolution of graphene production: from micron-size laboratory samples in 2004[1] to industrially compatible meter-size rolls in 2010[30].

Shortly after the discovery and particularly after it got largely popularized with the Nobel prize award in 2010, graphene used to be viewed as a supermaterial capable of solving the vast majority of problems the humanity is facing. As time passed the hype has declined and graphene and other 2D materials started to be perceived more conservatively. Now it is a technology with still incredibly high potential but which is far from its maturity and which requires significant development. What is certainly impressive is how fast the production of graphene scaled up from a laboratory sample to an industrially compatible product. The first graphene flake obtained in 2004[1] had lateral dimensions of a fraction of a human hair while already in 2010 meter-size rolls of graphene were synthesized[30] (figure 1.1). Such rapid development of manufacturing technology obviously forced researchers to think about applications. Among the most realistic ones from today‘s standpoint are the use of 2D vdW materials for metrology[31], in bendable touch screens[32], flexible electronics[33] or wearable biosensors for personalized medicine[34]. However, since the fundamental research in this field is still progressing very rapidly a lot of more astonishing applications which are not obvious now will most likely come out soon. The lemma formulated by Herbert Kroemer motivated by the discovery in the field semiconducting heterojunctions (Nobel Prize 2000) fits also very well for 2D vdW materials: "*The principal applications of any sufficiently new and innovative technology always have been – and will continue to be – appli-*

cations created by that technology".

1.2 Thesis outline

This thesis focuses on electronic and optical properties of 2D van-der-Waals semiconductors and their heterostructures. In particular, large part of our work is based on experiments done on atomically thin layers of group 6 transition metal dichalcogenides (TMDs) and its most studied member MoS_2 . *Chapters 4 and 5* are solely dedicated to MoS_2 obtained with two different methods – chemical vapor deposition (*Ch.4*) and exfoliation (*Ch.5*) – and reveal a substantial difference in electronic transport properties depending the synthesis method used. *Chapter 6* include results obtained also with other TMDs such as WS_2 , WSe_2 and $MoSe_2$. In *chapters 7* and *8* vdW heterostructures assembled from TMDs (*Ch.7*) and from TMDs and InSe layers (*Ch.8*) are investigated.

To facilitate the understanding and interpretation of experimental results presented in this work we introduce *Theoretical background* chapter (*chapter 2*) where the required theoretical concepts are explained in details. In *section 2.1* we provide an overview on transition metal dichalcogenides, describe which materials belong to this group, what are their crystalline structure and chemical composition. We further demonstrate the effect of dimensionality reduction (*i.e.,* going from 3D to 2D) on the electronic band structure and optical properties of these materials. Discussing the optical response of TMDs we pay readers attention on the peculiarity of excitons in 2D materials and the conditions for their radiative recombination. We also mention types of defects present in TMDs and their effect on the properties of TMDs.

In *section 2.2* we discuss semiconducting van-der-Waals heterostructures and their prominent advantages as compared to conventional semiconducting heterojunctions based on covalently bonded materials. We explain such key aspects of heterostructures as band alignment, charge transfer, and band bending which in large extent determine their properties and the performance of semiconducting devices based on them. Next, we introduce the concept of an *interlayer exciton* which is viewed as one of the most important features of vdW heterostructures. We explain what makes these excitons so attractive and describe the factors that render them either optically bright or dark.

Chapter 3 provides an overview of the main experimental techniques used in this thesis as well as the details of sample fabrication including material synthesis protocol and the sequence of steps employed to build vdW heterostructures.

Four out of five experimental chapters of this thesis include measurements done with ionic-liquid field effect transistors (IL FETs). Ionic-liquid gating technique is a very powerful experimental method particularly suitable for investigation of 2D materials. For example, it allows to measure the value of a single-particle band gap of semiconductor or probe the band alignment in semiconducting heterostructures. We find it, therefore, useful to describe in details this technique in a separate section (*section 3.1*). There we first introduce the structure of a conventional field-effect transistor, explain its operation principle and operation regimes. We further discuss FETs with ionic liquid gate dielectric, their structure, and functioning mechanism. Finally, we explain the main principle behind IL FET spectroscopy.

In *Chapter 4* we study transport properties of large-area MoS_2 monolayers grown by chemical vapor deposition using IL FETs. Under electron accumulation, the performance of these devices is comparable to that of FETs based on exfoliated flakes. FETs on CVD-grown material, however, exhibit clear ambipolar transport, which for monolayers had not been reported previously. We exploit this property to estimate the bandgap Δ of monolayer MoS_2 directly from the device transfer curves and find $\Delta \approx$ 2.4–2.7 eV. In the ambipolar injection regime, we observe electroluminescence due to exciton recombination in MoS_2 , originating from the region close to the hole-injecting contact. Both the observed transport properties and the behavior of the electroluminescence can be consistently understood as due to the presence of defect states at an energy of 250–300 meV above the top of the valence band, acting as deep traps for holes.

The presence of the in-gap trap state in MoS_2 monolayer is further confirmed by the detailed transport characterization shown in *Chapter 5* where we investigate the ability of exfoliated monolayers of MoS_2 to support high-quality, well-balanced ambipolar conduction. Using ionic-liquid gated transistors, we demonstrate that, contrary to WS_2 , $MoSe_2$, and WSe_2 , hole transport in exfoliated MoS_2 monolayers is systematically anomalous, exhibiting a maximum in conductivity at negative gate voltage (V_G) followed by a suppression of up to 100 times upon further increasing V_G. To understand the origin of this difference, we have performed a series of experiments including the comparison of hole transport in MoS_2 monolayers and thicker multilayers, in exfoliated and CVD-grown monolayers, as well as gate-dependent optical measurements (Raman and photoluminescence) and scanning tunneling imaging and spectroscopy. In agreement with existing *ab-initio* calculations, the results of all these experiments are consistently explained in terms of defects associated with chalcogen vacancies that only in MoS_2 monolayers, but not in thicker MoS_2 multilayers nor in monolayers of the other common semiconducting TMDs, create in-gap states near the top of the valence band that act as strong hole traps.

In *Chapter 6* we report a combined experimental and theoretical investigation that reveals a new mechanism responsible for the enhancement of electron-phonon coupling in doped semiconductors in which multiple inequivalent valleys are simultaneously populated. Using Raman spectroscopy on ionic-liquid-gated mono and bilayer MoS_2, WS_2, and WSe_2 over a wide range of electron and hole densities, we find that phonons with a dominant out-of-plane character exhibit strong softening upon electron accumulation, while remaining unaffected upon hole doping. This unexpected – but very pronounced – electron-hole asymmetry is systematically observed in all mono and bilayers. By performing first-principles simulations, we show that the phonon softening occurs when multiple inequivalent valleys are populated simultaneously. Accordingly, the observed electron-hole asymmetry originates from the much larger energy separation between valleys in the valence bands –as compared to the conduction band– that prevents the population of multiple valleys upon hole accumulation. We infer that the enhancement of the electron-phonon coupling that drives the softening upon electron doping occurs because the population of multiple valleys acts to strongly reduce the efficiency of electrostatic screening for those phonon modes that cause the energy of the inequivalent valleys to oscillate out of phase.

In *Chapter 7* we study the transport and opto-electronic response of two different van-der-Waals heterostructure based on transition metal dichalcogenide monolayers, namely $WSe_2/MoSe_2$ and WSe_2/MoS_2. By exploiting the spectroscopic capabilities of IL FETs, we show how the conduction and valence bands of the individual monolayers determine the bands of the interface, and we establish quantitatively – directly from the measurements – the energetic alignment of the bands in the different materials, as well as the magnitude of the interfacial band gap. Photoluminescence and photocurrent measurements allow us to conclude that the band gap of the $WSe_2/MoSe_2$ interface is direct in $k-$space, whereas the gap of

WSe_2/MoS_2 is indirect. For $WSe_2/MoSe_2$ we detect the light emitted from the decay of interlayer excitons and determine experimentally their binding energy using the values of the interfacial band gap extracted from transport measurements. The technique that we employed to reach this conclusion demonstrates a rather general strategy to characterize quantitatively the interfacial properties in terms of the properties of the constituent atomic layers. The results presented here further illustrate how van der Waals interfaces of two distinct 2D semiconducting materials are composite systems that truly behave as *artificial semiconductors*, whose properties can be deterministically defined by the selection of the appropriate constituent semiconducting monolayers.

Finally, in *Chapter 8* we proceed with material property engineering using van-der-Waals heterostructures and provide a method to build a composite direct band gap semiconductor out of the two indirect band gap ones which is particularly relevant for the observation of bright interlayer excitons. Previous work done on interlayer excitons in vdW interfaces relied on a very limited combination of materials which has the same lattice symmetry, matching lattice constant and are rotationally aligned, as it is required to achieve radiative recombination of these excitons. In our approach indirect band gap semiconductors with either conduction or valence band edges lying in the center of the Brillouin zone – at the Γ-point – are combined yielding a direct band-gap heterostructures in which formed interlayer excitons, called Γ-Γ excitons, are always optically bright. A systematic study of multiple combinations of group 6 TMDs with InSe and GaSe enabled us to determine the band alignment in these heterointerfaces and establish the principle mechanism of charge transfer.

Chapter 2: Theoretical background

2.1 Transition metal dichalcogenides

2.1.1 Chemistry and crystalline structure

Transition metal dichalcogenides are compounds with general stoichiometric formula MX_2[10] where M is a transition metal (*i.e.,* an element with partially filled *d*-shell) and X is a chalcogen atom (sulfur, selenium or tellurium). The members of this class of materials are marked in the periodic table in figure 2.1a. Compounds with metals from group 4-7 form mainly layered structure while the ones of groups 9 and 10 are usually found to be nonlayered (*e.g.* NiS_2 has an apyrite structure). In layered TMDs atoms are covalently bonded within the plane while in the out-of-plane direction they are held together by weak van-der-Waals forces. Weak interlayer forces enable relatively easy isolation of atomically thin layers down to ultimate monolayer limit. A TMD monolayer is composed of a layer of transition metal atoms sandwiched between two layers of chalcogen atoms. Orbitals of a chalcogen atom in these materials terminate with *lone-pair* electrons which determine the absence of dangling bonds and make these materials chemically stable.

Apart from the chemical composition a crucial aspect determining the properties of a material is the relative arrangement of atoms in space. A TMD monolayer frequently adopts 2 different crystalline structures - the *1T* (figure 2.1b) and the *2H* (figure 2.1c) for which coordination of a metal atom is trigonal prismatic and octahedral respectively. In thicker TMD layers the 2H monolayer can be stacked either in an ABA (middle column 2.1d) or in an ABC (right column 2.1d) sequence, with the later configuration giving rise to the rhombohedral *3R* phase[35]. The vast majority of materials discussed in this thesis has 2H structure and we, therefore, consider only this structure in the following discussion, unless specifically indicated otherwise.

In figure 2.1e two unit cells representing a TMD bilayer are shown. In this configuration the lower unit cell is transformed exactly into the upper one upon an inversion transformation with respect to the inversion center[36] (marked with the *i* point in the figure 2.1e). This implies that these structures posses *inversion symmetry.* For a TMD monolayer, however, this is not the case. For example, upon selecting a transition metal atom as an inversion center the chalogen atoms of the bottom layer are mapped to an empty space and do not superimpose with the ones of the upper layer. Therefore, in 2H TMD monolayers inversion symmetry is broken. Through similar considerations one can see that the inversion symmetry is preserved for stacks composed of even number of layers and is broken for odd number of layers.

The TMDs that we will consider crystallize in a hexagonal lattice. The first Brillouin zone (BZ) of a 2D hexagonal lattice is shown in figure 2.1e. The center of the BZ, k_x=k_y=0, is conventionally referred to as the Γ point. The BZ corners consist of 2 inequivalent groups denoted as K and -K points[37]. Each one of the three points within one of the groups are equivalent, as they are related to each other by reciprocal lattice vectors. The K and -K points are linked by time-reversal symmetry (*i.e.,* they transform into each other upon time reversal transformation). At approximately halfway between Γ and K points lie the Q points. These points are important because of the corresponding band extrema in the electronic band structure of TMD multilayers as discussed in section 2.1.2.

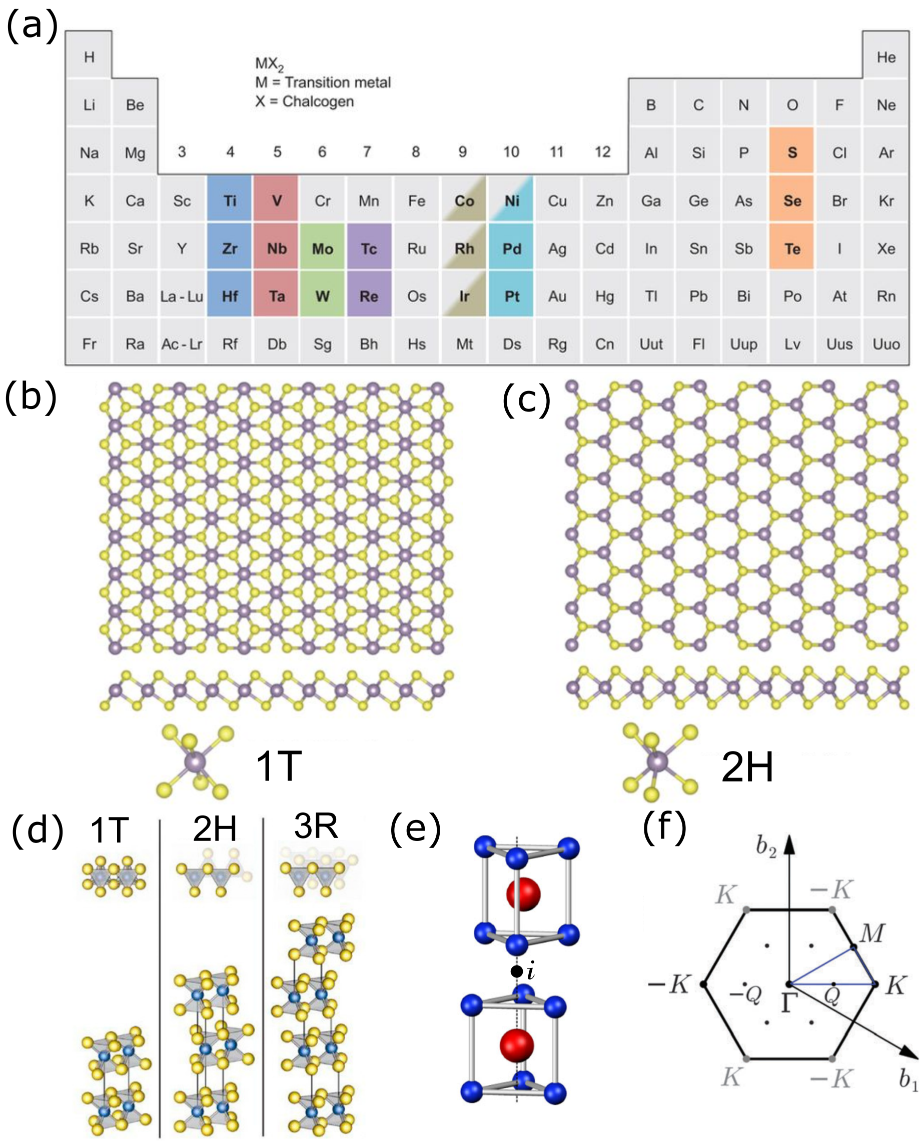

Figure 2.1: Chemistry and crystalline structure of TMDs. (a) The periodic table showing the transition metals (shaded with blue, pink, green violet) and the chalcogen elements (shaded with orange), taken from Ref. 10. (b,c) Crystalline structures of TMD monolayers representing the 1T (b) and the 2H (c) structures with trigonal prismatic and octahedral metal coordination respectively, taken from Ref. 10. (d) Stacking polytypes of bulk TMDs, adapted from Ref. 35. (e) Two unit cells representing 2H TMD bilayer with the inversion center i located in-between the cells, taken from Ref. 36. (f) The first Brillouin zone of a 2D hexagonal lattice, taken from Ref. 37.

The electronic properties are largely determined by the coordination environment of the transition metal and by the number of d-electrons involved in the bound formation. Table 1 shows the summary of electronic properties for many of these compounds. Depending on the filling of the non-bonding d bands TMDs can be semiconductors, metals, semimetals[10]. They can support superconductivity. In this thesis we study semiconducting TMDs and focus mainly on group 6 TMDs.

Table 1: Electronic properties of TMDs

Group	M	X	Properties
4	Ti,Hf,Zr	S,Se,Te	Semiconducting
5	V,Nb,Ta	S,Se,Te	Narrow band metals or semimetals. Superconducting. Charge density waves
6	Mo,W	S,Se,Te	Semiconducting, WTe_2 is semimetal
7	Tc,Re	S,Se,Te	Small-gap semiconductors
10	Pd,Pt	S,Se,Te	Sulfides and selenides are semiconducting Tellurides are semimetals.

2.1.2 Band structure of semiconducting TMDs

There is a number of important aspects in the band structure of semiconducting TMDs which largely determine the electronic and optical properties of these materials and are particularly relevant to interpret the experiments done in the context of this thesis. One is the effect of the spatial confinement on the band structure in different parts of the Brillouin zone (*i.e.,* how the band structure changes upon varying the thickness of the material). Another one is the strength of the spin-orbit coupling and its coupling to the valley degree of freedom, leading to the so-called *spin-valley locking.* These properties are similar for the different group 6 TMDs, and here we select MoS_2 as an illustrative example to showcase this behaviour.

Indirect-to-direct band gap crossover

With the development of modern micro- and nanofabrication techniques enabling the patterning of structures and devices at the nanometer scale material dimensionality has become a crucial design parameter. A very prominent example of the effect of dimensionality reduction is the quantization of the energy levels seen in quantum wells of III-V compounds[13]. In this case the size of a structure and, hence, confining potential along one of material dimension is considerably reduced. Such a spatial confinement of charge carriers makes the physical properties of the material to be entirely governed by quantum mechanical effects. In semiconducting TMDs dimensionality reduction also plays a pivotal role and governs the evolution of their electronic band structure in the crossover from 3D to 2D.

We start with discussing the band structure of bulk MoS_2 . In figure 2.2a the calculated band structure of MoS_2 is shown representing the energy bands as a function of lattice wave vector (*i.e.*, dispersion relation). The continuum of states forming the valence and conduction bands are separated in energy by a region with no electron states available. The lowest energy state that an electron can occupy in the conduction band is called conduction band minimum (CBM), while the highest energy state in the valence band – valence band maximum (VBM). The energy difference between CBM and VBM determines the size of *band gap*. Of particular interest are the different bands extrema present in the conduction and valence bands, at the Q, Γ and K points. For bulk MoS_2 (figure 2.2a) the global extrema of the conduction and valence bands lie at the Q and the Γ points respectively[38]. Having CBM and VBM at the different points in the momentum space implies that a material is an *indirect* band gap semiconductor.

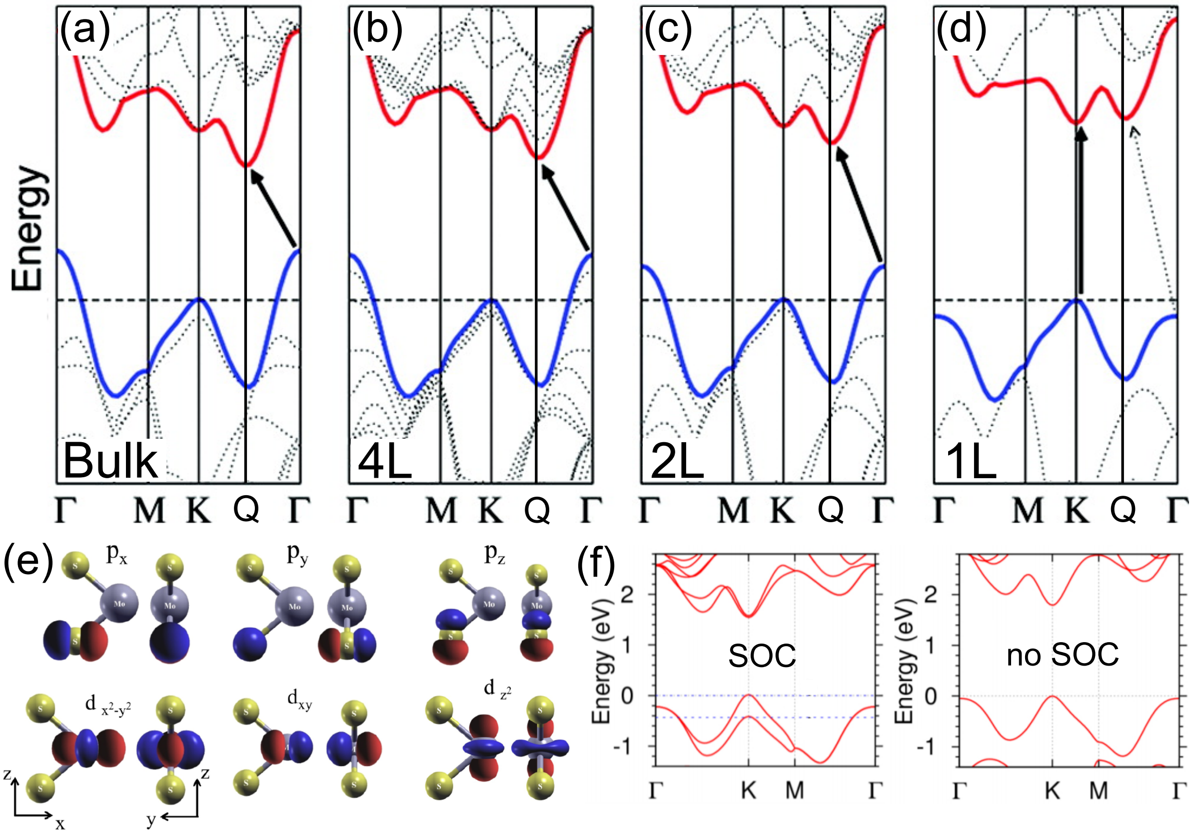

Figure 2.2: Calculated band structure of MoS_2 (a) bulk, (b) 4 layers, (c) 2 layers and (d) monolayer, taken from Ref. 38. (e) Schemes of the atomic orbitals primarily involved in the formation of the conduction and valence band edges of MoS_2 , taken from Ref. 39. (f) Calculated band structure of MoS_2 monolayer with (the left panel) and without (the right panel) spin-orbit coupling included, taken from Ref. 37.

Upon decreasing the thickness of MoS_2 down to few nanometers the position of band edges at the Q and the Γ points shifts in energy. In figures 2.2b,c the band structure for 4 and 2 layers are shown, where the

CBM and the VBM progressively increase their energy, resulting in an increase of the band gap. This change in energy originates from the nature of atomic orbitals involved in formation of these bands. In the case of the Γ point it is a combination of p_z orbitals of S atoms and d_{z^2} orbitals of Mo atoms, which have strong out-of-plane character as shown in figure 2.2e. Such orbital geometry leads to strong electronic coupling between TMD layers. The charge carriers in this system can be viewed analogously to the well-known particle in a box model. According to this model the energy of a particle E_n is inversely proportional to the interbarrier spacing L ($E_n = n^2h^2/8mL^2$). Accordingly, the energy of bands at the Q and the Γ points in TMDs increases with decreasing the number of layers.

The position of the local conduction and valence bands extrema at the K point – unlike the bands at the Q and Γ points – are almost not affected by the change in thickness. These bands are formed by the $d_{x^2-y^2} + d_{xy}$ orbitals of Mo atoms and the $p_x + p_y$ orbitals of S atoms with mainly in-plane character[39] and therefore weak interlayer coupling. That is why the energy of the bands at the K/-K points almost does not change upon varying the thickness of MoS_2 . As a result, when the thickness is reduced down to the monolayer limit (figure 2.2d), the energy separation between the bands edges at Q and Γ becomes larger than the one at the K point. Thus, bands extrema at the K point become global and the band gap becomes *direct*. This indirect-to-direct band gap crossover is a very remarkable property of group 6 TMDs making them particularly attractive for novel opto-electronic applications.

Spin-orbit coupling

Spin-orbit coupling (SOC) is a relativistic effect caused by the interaction between the particle spin with its motion in a potential. A prominent example of this phenomenon is the coupling between electron spin ($\boldsymbol{S}$) and its orbital angular momentum ($\boldsymbol{L}$) due to its motion around a proton in an atom. In the electron reference frame it is the proton which rotates around it. This circulation of the positively charged proton creates a magnetic field which acts on the electron magnetic dipole moment generated by its spin. This coupling leads to the splitting of electron energy levels caused by the Zeeman effect. The strength of the SOC is proportional to the scalar product of the electron orbital momentum and its spin $\boldsymbol{L} \cdot \boldsymbol{S}$. In TMDs spin-orbit coupling is important to fully capture all the features of the electronic band structure. It is particularly strong for the band edges at the K/-K points as they originate from the d-orbitals of the heavy transition metal[36,40,41]. Strong SOC lifts the spin degeneracy of these bands and thus makes them spin-polarized (see figure 2.2f). In monolayers the magnitude of the bands splitting at the K/-K points is of the order of hundreds of meV in the valence band and of tens of meV in the conduction band.

Valley degree of freedom

The corners of the first Brillouin zone of TMDs are composed of two inequivalent groups of high symmetry points referred to as K and -K (see figure 2.1f). The energy of bands extrema at these points are the same. Such energy degenerate bands are called *electron valleys*. As discussed in section 2.1.1, K and -K points are related to each other by time reversal symmetry. Carriers in K and -K valleys should, therefore, have opposite spins (figure 2.3a). Having a particular spin rigidly linked to a particular valley is called *spin-valley locking*.

In TMD monolayers, where the band extrema at the K/-K points are global, the optical selection rules for the interband transitions impose that the carriers in K and -K valleys couple to circularly polarized light of opposite helicity[37]. It is, therefore, possible to selectively populate these valleys by illuminating a monolayer with laser having either σ_+ or σ_- polarization as shown in figure 2.3b. Thus, K and -K valleys having the same energy can be distinguished due to the spin-valley locking and be separately addressed with σ_+/ σ_- photon. The possibility to discriminate between energy degenerate valleys provide TMD monolayers with the *valley degree of freedom*[42–44]. This property enables the observation of new phenomena. For example, the new type of Hall effect – the *valley Hall effect* has already been reported in TMD monolayers, where the transversal voltage is generated by imbalanced valley currents at device edges[45,46].

2.1.3 Optical properties of semiconducting TMDs

The emergence of a direct band-gap in monolayers together with the spin splitting of bands and the valley degree of freedom make TMD particularly attractive to study optoelectronic phenomena. In addition, the reduced dimensionality suppresses screening of interactions between charge carriers, which differentiate the properties of 2D TMDs from those of conventional 3D semiconductors. It is, therefore, important to understand the essential aspects of light-matter interaction in atomically thin TMDs.

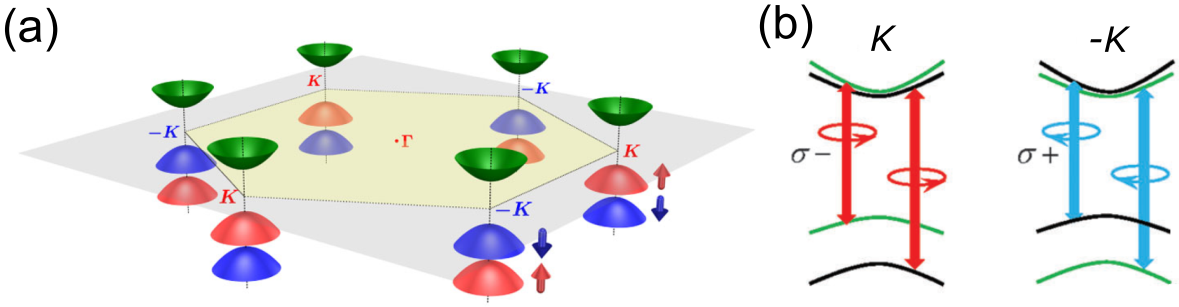

Figure 2.3: (a) Scheme of K/-K valleys with corresponding spins in a TMD monolayer. (b) Optical selection rules for the interband transitions in TMD monolayers, taken from Ref. 37

In semiconductors light-matter coupling is responsible for such phenomena as reflection, transmission, absorption and scattering of light. Upon illuminating a semiconductor with a beam of light an electron in the valence band is excited to a state in the conduction band leaving a hole in the valence band. This process, in the absence of interaction between electron and hole (*i.e.,* having independent electrons and holes), is governed by material absorption cross section determined by the joint density of states. In the presence of interaction, instead, the formation of an electron-hole complex with correlated motion occurs. This complex is an elementary excitation of the semiconductor called *exciton*.

Excitons in 2D

An exciton is a two-body quasiparticle whose motion can be decomposed into two components – the motion of an exciton center-of-mass (CM) and the relative motion of the electron and hole. Within the effective mass approximation[13] the degree of freedom associated to the CM is analogous to that of a free particle with kinetic energy $E_{ke} = \hbar^2 Q_{ex}^2/2M$ where M=$m_e + m_h$ and $Q_{ex} = k_e + k_h$ – exciton wave vector. In 3D the relative motion of electron and hole can be well approximated by the motion of an electron around a proton in a hydrogen atom. The quantized series of energy states – known as the *Rydberg series* – is defined according to $-13.6eV\frac{\mu}{m_0\varepsilon^2 n^2}$ where $\mu = \frac{m_e m_h}{m_e+m_h}$ is the reduced exciton mass, n – principal quantum number which is integer. Summing these two components and adding the semiconductor band gap yields the exciton dispersion relation:

$$E_{ex}(n, Q_{ex}) = E_g - 13.6eV\frac{\mu}{m_0\varepsilon^2 n^2} + \frac{\hbar^2 Q_{ex}^2}{2M} \tag{2.1}$$

which is depicted in figure 2.4b. A series of discrete levels is followed by continuum of states at the $n \rightarrow \infty$ limit. The onset of this continuum is defined as the *free-particle* band gap and the lowest energy excitonic state (*i.e.,* with n=1) is the *optical* band gap. The difference between these two energies gives the *exciton binding energy* E_b^{ex} which is governed by the second term in (2.1).

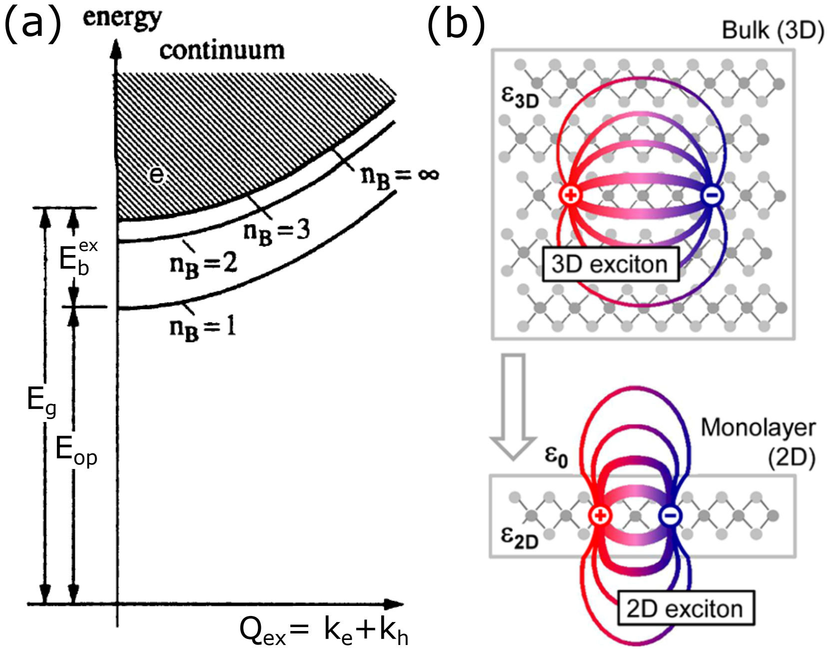

Figure 2.4: (a) Dispersion relation of an exciton, taken from Ref. 13. (b) Schematic representation of excitons in 3D and 2D, taken from Ref. 20. Screening of the Coulomb potential is largely reduced in the 2D case due to the change of dielectric environment.

In the 2D case[20,21] the solution of the hydrogen atom problem yields the energy spectrum given by $-13.6eV\frac{\mu}{m_0\varepsilon^2(n-1/2)^2}$. As compared to the 3D solution the n^2 term in the denominator is replaced by $(n-1/2)^2$. For the 1S exciton state (*i.e.,* with n=1) it implies 4 times increase in the exciton binding energy. Another important distinction comes from difference in size of excitons in 2D and 3D. In 2D semiconductors excitons are confined within atomically thin layers of material, which considerably reduces their radius. The electric field induced by electron-hole Coulomb interaction extends outside the material where it experiences much less screening due to the dielectric environment as compared to the 3D case where the field is largely attenuated by material[20] (see figure 2.4c). The enhanced Coulomb interaction leads to the increase of the exciton binding energy which in 2D TMDs can be as large as several hundreds of meV. A large E_b^{ex} value also implies a very sizeable difference between the free particle band gap and the optical gap. Values of E_g and E_{op} are usually determined by different experimental techniques and their precise assignment is getting particular important for TMDs.

A neutral electron-hole pair can also acquire an additional electron or hole and form the three-particle state (analogous to hydrogen ions H^- or H_2^+). This charged exciton state is called *trion*. It is formed in the presence of finite density of charge carriers. Adding an electron or a hole to an exciton increases the binding energy of this state. The optical band gap of a trion is therefore lower than the one of the respective exciton. In TMD monolayers the difference between these two gaps, called the *trion binding energy* E_b^{trion}, is as large as 20-40 meV[47–49] which enables to observe trions even at room temperature.

Bright and dark excitons

After its formation, an exciton can recombine either by emitting a photon (*i.e.,* being optically bright) or through a non-radiative path like impurity-assisted recombination (*i.e.,* being optically dark). For the radiative recombination to occur the exciton and the resultant photon momenta have to match as required by momentum conservation. This condition is visualized in figure 2.5a, where the exciton dispersion is combined with the free-space photon dispersion c*$q_\|$ ($q_\|$ is the projection of photon wave vector on material plane). In this representation an exciton is bright if its CM wave vector Q_{ex} lies within the area delimited by c*$q_\|$, called the *light cone*, and dark if K_{ex} is outside this cone (*i.e.,* $Q_{ex} >$ c*$q_\|$)[21]. The photon momentum is a very small quantity and the condition for the radiative recombination to occur can be approximated with $Q_{ex} \approx 0$. This condition is met for excitons in direct band gap semiconductors as the electrons and holes of which they consist are residing at the CBM and VBM with the same momentum and hence $Q_{ex} = 0$. For indirect band gap semiconductors, the CBM and the VBM are displaced in momentum space and $Q_{ex} > 0$. In this case, nevertheless, the exciton can still recombine radiatively if the momentum conservation is satisfied by involving a phonon with the required momentum.

Apart from momentum conservation whether an exciton is bright or dark is also determined by the presence of optical selection rules[50,51]. As mentioned before carriers in TMD monolayers posses valley (τ) and spin (σ) degrees of freedom. Exciton states having the same spin and with electron and hole occupying the same valley (K or -K) are bright, while states with different spins or different valleys are dark (figure 2.5b).

Interestingly, in TMD monolayers the spin configuration of bands is dif-

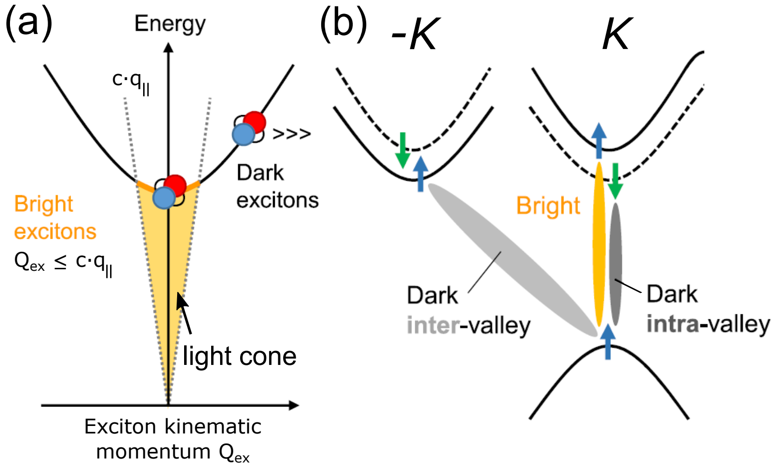

Figure 2.5: (a) Exciton dispersion matched with the free-space photon dispersion (*i.e.,* light cone). Excitons with kinematic momentum Q_{ex} inside the light cone are optically bright, while those with Q_{ex} outside the cone are dark. (b) Schematic representation of spin and valley dependent optical selection rules for TMD monolayers. Figures are taken from Ref. 21

ferent in Mo- and W-based compounds. For MoS_2 and $MoSe_2$ the highest energy conduction band and the lowest energy valence band have the same spin, whereas for WS_2 and WSe_2 spin values are opposite[52,53]. Therefore, the lowest energy transition in W-based TMDs is spin-forbidden and the excitons formed from the carriers residing in these bands are optically dark. However, as it was discussed in section 2.1.2, the spin splitting in the conduction band of TMD is significantly smaller than the one of the valence band. For example, in WSe_2 this splitting is $\approx$ 30meV. At room temperature the higher energy conduction band can be populated due to thermal excitation of carriers from the lower energy one, thus enabling radiative exciton recombination. Upon decreasing temperature, however, the intensity of this process decreases and nearly vanishes at T=4K[53]. In Mo-based compounds the opposite trend is observed – the intensity of exciton recombination increases upon cooling down.

2.1.4 Defects in TMDs

The properties of an ideal material are mainly determined by its chemical composition and its crystalline structure. In reality, however, ideal materials do not exist as imperfections of the crystalline structure and in the chemical composition, such as crystalline defects or impurities, are always present. These imperfections, depending on their type and concentration, can have a profound effect on the material properties. For semiconductors, in particular, impurities play a key role. For instance, dopants (*i.e.,* intentionally induced chemical impurities) can drastically change the conductivity of a semiconductor and turn it into a metal. The possibility to modify the conductivity of a semiconductor lies at the heart of the MOSFET technology where the doping profile of a silicon wafer defines its semiconducting and metallic (*i.e.,* source and drain contacts of a FET) regions. Often, however, defects can affect the material properties in a detrimental way. It is therefore crucial to characterize defects that are typically present in a material and to be able to control them.

In TMDs several types of defects can be present such as stacking faults, line defects (*e.g.* dislocations or grain boundaries), point defects (*e.g.* chalcogen vacancies and divacancies, transition metal vacancies and their complexes), antisite defects (*e.g.* when a Mo atom is substituted by a S atom in MoS_2)[54]. One of the most abundant ones, however, are chalcogen vacancies/divacanies. They have the lowest formation energy[55] which determine their high concentration in naturally occurring crystals. The density of sulfur vacancies in MoS_2 monolayer, for example, can be as high as $1*10^{13}$ cm^{-2}[56].

Chalcogen vacancies impact the electronic band structure and induce additional density of states. Depending on their energy, these states can have radically different effects on the material properties. If a defect-induced state is situated inside the valence or conduction bands, it can hybridize with delocalized states present at the same energy and has a limited influence on the material property. When, however, the energy of these states falls into the band-gap, the defect can act either as dopant or as trap for free charge carriers. The presence of traps can considerably deteriorate carrier mobility as carriers get localized at defect sites causing transport to occur in the hopping regime rather than in the band-like regime[57]. Indeed, the presence of in-gap states can hinder ambipolar conduction, as observed in MoS_2 monolayers discussed in more details in *Chapter 5.*

Another type of defects relevant for TMD layers synthesized with chemical vapor deposition (CVD) are grain boundaries. Grain boundaries are usually absent in exfoliated TMD layers. Formation of grain boundaries occurs due to merging of crystallites originating from multiple nucleation sites. Usually the crystalline orientation of these grains are random and lattices of neighbouring crystallites are misaligned. Electronic transport across such large angle grain boundaries is significantly deteriorated as compared to the single crystal case. One approach to overcome this problem is the use of the appropriate growth substrates enabling epitaxial film growth. In this case the orientation of crystallites is determined by the growth substrate, so that upon merging they do not form large angle grain boundaries. For example, for the CVD growth of MoS_2 a sapphire substrate[58] can be successfully employed for this purpose as discussed in *Chapter 4*.

2.2 Semiconducting van-der-Waals heterostructures

Semiconducting heterostructures are one of the key components of modern microelectronic industry which find application in different types of functional devices. For example, heterojunctions based on III-V compounds are largely used in high-electron-mobility transistors enabling high-frequency operation, a functionality critical for such fields as satellite communication, radio astronomy or mobile telecommunication. In a particularly efficient type of solar cells – multi-junction solar cells – stacks of semiconductors with different band gaps are key to allow efficient light absorption in a large range of wavelengths. In quantum cascade lasers, intersubband transitions across periodic series of semiconducting heterostructures allow to emit in the long wavelength range (from 2 to 250 μm), a feature that is exploited for remote chemical sensing or collision avoidance radar. Besides this plethora of applications, semiconducting heterostructures are also at the heart of fundamental discoveries such as the integer and fractional quantum Hall effect.

Despite all these impressive achievements, the field of semiconducting heterostructures faces serious limitation because of the very limited materials that can be effectively combined together. This limitation stems from the fact that constituent materials forming these heterostructures are connected by strong covalent bonds. For this to happen over a large area the materials have to have the same lattice symmetry and matching lattice constants. Even though there are a number of techniques to adjust the lattice parameters of junction constituents (*e.g.* using pre-strained substrates) they do not significantly enlarge the possible combinations and can lead to defect formation (*e.g.* edge or screw dislocations) degrading the properties of a heterostructure.

For heterostructures formed out of vdW materials, however, the limitation of lattice compatibility is no longer present. In this case, the interlayer bonding is realized through very weak van-der-Waals forces (the strength of a vdW bond is about two orders of magnitude lower than the one of a covalent bond). Therefore, a vdW heterostructure can be easily created by selecting the desired combination of components from the rich library of known vdW materials irrespective of their lattice constants and crystal symmetry[22,23]. Furthermore, vdW heterostructures provide a *rotational degree of freedom.* Lattices of constituent layers can be freely rotated with respect to each other to match the required alignment angle which has already led to the emergence of very remarkable phenomena including superconductivity in twisted bilayer graphene[27] or satellite Dirac peaks in graphene-boron nitride stacks[24–26]. Such flexibility makes vdW heterostructures highly attractive as a powerful playground to study new physical phenomena of fundamental interest.

In this thesis we will focus on heterostructures assembled from semiconductors. To correctly interpret experimental results discussed in the following chapters, in this section we introduce a key aspect of semiconducting heterostructures, namely the band alignment. We further consider a special type of excitons present in these heterostructures – *interlayer excitons* – and discuss the features which make them particularly appealing both for fundamental studies and for novel applications in photonic circuits.

2.2.1 Band alignment

The majority of properties of a semiconductor is determined by the electronic states having energy in the vicinity of conduction and valence band edges. Similarly, for semiconducting heterostructures the relative position of CBM and VBM in the constituent materials, *i.e.,* the relative alignment of the bands in the two materials, is of primary importance. There are 3 types of possible band alignment[13] as shown in figure 2.6a-c. Here we consider the relative alignment between two different semiconductors – A and B – for which the conduction and valence bands are pictured in green and orange respectively.

Type I

In this type of alignment (figure 2.6a) the conduction band edge of a semiconductor A has lower energy than the one of a semiconductor B, and at the same time the valence band edge of A lies above that of B. Thus, the band gap of semiconductor A is completely inside the band gap of semiconductor B. Let us now consider a structure where the material A is placed in-between two layers of material B, as shown in figure 2.6d. The energy difference between conduction and valence bands of the heterostructure components – called *band offset* – creates potential barriers which confine both electrons and holes within material A. Thus, this structure can be viewed as two potential wells – for electrons and for holes – the depths of which are determined by the respective band offsets. Charge carriers in such well can be considered analogously to the particle in a box model with, however, finite barrier height. According to this model, the energy of charge carriers inside the well increases with decreasing the thickness of material A, which is a well-known consequence of *quantum confinement*. Hence we can effectively increase the size of the band gap by changing the material thickness in a heterostructure.

This type of band arrangement is used in applications that require both types of charge carriers to be localized within the same semiconductor. For example, it has successfully been employed in *double heterostructure lasers*[59,60]. This type of lasers are very notable as they greatly impacted our modern world since their invention and their importance was marked by the physics Noble Prize of 2000 (H. Kroemer and Zh. Alferov). In this laser a smaller band gap material (*e.g.* GaAs) is sandwiched between two layers of larger band gap material (*e.g.* AlGaAs) which are n- and p-doped. Under forward bias electrons and holes from the n- and p-doped AlGaAs layers are injected respectively into the conduction and valence bands of the GaAs layer. Electrons and holes simultaneously present in the same material recombine and emit photons. Such localization of charge carriers within a thin layer largely enhances radiative recombination rate and hence increases the laser efficiency.

In 2D TMDs charge carriers are naturally confined within the distance determined by the thickness of the material which can be as thin as a monolayer. Therefore, the effects related to the quantum confinement can be readily observed in single component materials without the need to assemble heterostructures. One of these effects is the increase of the band gap of MoS_2 with decrease of its thickness discussed in section 2.1.2. VdW heterostructures with type I band alignment, nevertheless, also have some advantages. For example it is possible to significantly enhance light absorption in the smaller band gap material as it was shown, for example, for MoS_2 - ReS_2 system[61].

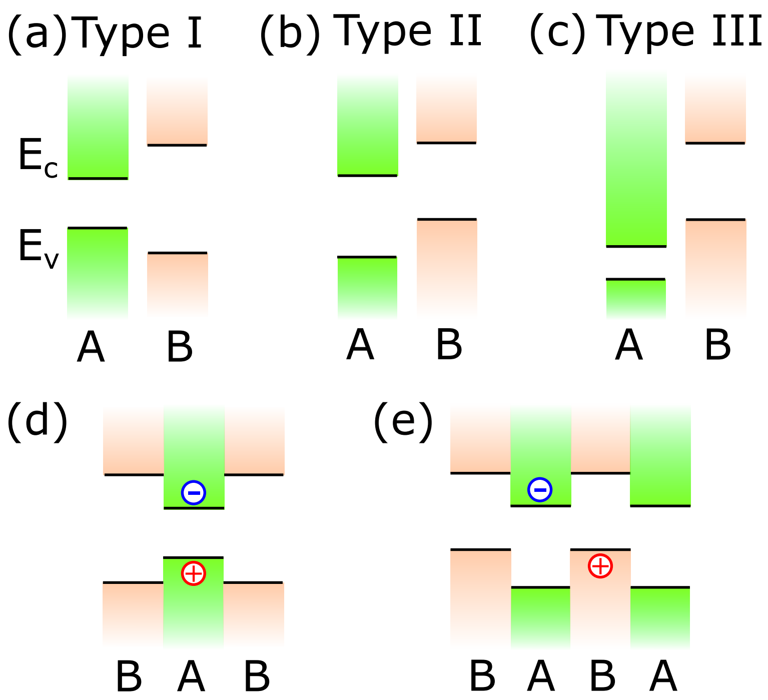

Figure 2.6: Types of band alignment in semiconducting heterostructures representing type I(a), II(b), and III (c). Heterostructure stacks enabling charge carriers confinement in type I (d) and type II (e) heterostructures.

Type II

In this case (figure 2.6b) the conduction band minimum of material A lies inside the band gap of material B (*i.e.*, the energy of the CBM of A is lower than that of B), but for the valence band edge the situation is the opposite: the VBM of B falls inside the band gap of A. Similarly to the type I case, sandwiching semiconductor A between two layers of semiconductor B results in a potential well for electrons in A. Holes, in turn, can be confined in a potential well in the opposite case, *i.e.*, if a layer of B is clamped between two layers of A (see figure 2.6e). The effective band gap of this heterostructure is determined by the energy separation between the CBM of A and the VBM of B. This is a noteworthy feature of this staggered alignment, as it opens up the possibility to engineer the band gap of a heterostructure by selecting an appropriate combination of materials, with the desired CBM to VBM energy spacing.

Type III

In this alignment (figure 2.6c) the conduction band edge of semiconductor A lies below the valence band edge of semiconductor B. Heterostructures with such alignment effectively do not have a band gap, which implies that there are states available for electron or hole conduction at all energies. It is particularly remarkable that the combination of two nominally insulating materials yields a conducting heterostructure. Materials in which conduction and valence bands overlap are called *semimetals*. In type III heterostructures such overlap is determined by the choice of the constituents and they can be, therefore, viewed as *artificial semimetals*.

Charge transfer and band bending

The picture of band alignment presented above forms the basis to describe the band diagram of heterostructures as we show here. We first discuss the case of conventional 3D heterojunctions and then address the important aspects which accompany the formation of 2D vdW heterostructures. In figure 2.7a we show the position of bands of two different 3D semiconductors (A and B) before the contact. Although the discussion here is based on type II heterostructure the most considerations made hold true also for type I and III alignment.

We consider the specific situation in which the two materials – A and B – have their chemical potentials close to the conduction (*i.e.,* n-doped) and valence (*i.e.,* p-doped) bands, respectively. When the heterostructure is formed (figure 2.7b) the electrochemical potential μ aligns across the whole volume, leading to the redistribution of charge carriers in the interface region[4,62]. Electrons diffuse from the n-doped semiconductor towards the p-doped one, while holes move in the opposite direction. This charge redistribution creates, in turn, a potential difference – the built-in voltage – which generates drift current of opposite direction. At the thermal equilibrium these diffusive and drift currents balance each other. The built-in voltage established in the interface region causes the formation of the *space-charge regions* where the position of conduction and valence bands varies in space. This spatial variation of bands is called *band bending*. In conventional 3D heterojunctions, depending on the initial doping, the space-charge region can extend over several hundreds of nanometers.

In 2D vdW heterostructures the alignment of the electrochemical potential also leads to charge transfer between the two materials. The important distinction from the 3D case arises, however, from the heterostructure dimension. The characteristic thickness of a 2D heterostructure is of the order of a few nanometers, even less than 2nm for a heterostructure built from two TMD monolayers. This thickness is so small, that it prevents the formation of any sizeable band bending (*i.e.,* there is simply not enough

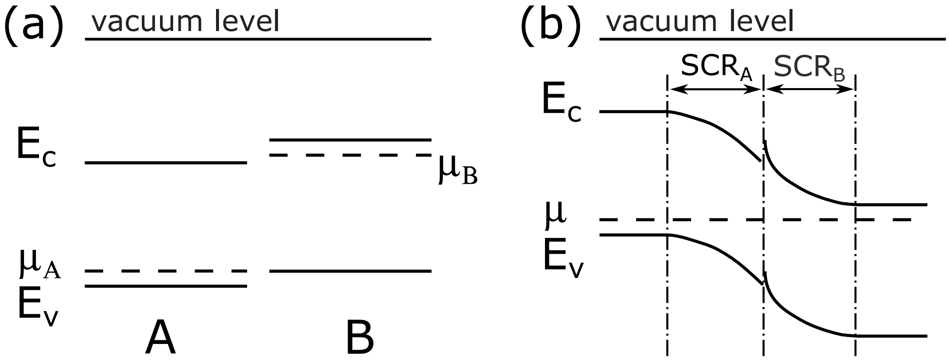

Figure 2.7: Energy-band diagrams of two isolated 3D semiconductors (a) and their heterostructure at the thermal equilibrium (b). The alignment of electrochemical potential μ leads to charge transfer between the semiconductors and formation of built-in voltage in the interface region. The established potential changes the position of the bands resulting into band bending.

space for the bands to vary continuously with position). Therefore, a simple band diagram shown in figure 2.6b is sufficient to illustrate the position of the bands across the whole heterostructure. Another related implication of atomic-size thickness of vdW heterotructures is that now there is no longer distinction between surface and bulk properties. A 2D vdW heterostructure is an interface by itself.

2.2.2 Interlayer exciton

In section 2.1.3 we have introduced the concept of exciton as a bound electron-hole pair. In TMD monolayers excitons have remarkably large binding energy which makes them stable even at room temperature. These materials are, thus, a powerful platform to study excitons. Semiconducting vdW heterostructures extend these possibilities even further.

In vdW heterostructures, in the same way as in single component materials, electrons and holes can bound by Coulomb force and form excitons. In this case, however, there are two possibilities. If both electrons and holes are confined within the same heterostructure constituent, as shown in the upper panel of 2.8a, then the resultant excitons are called *intralayer excitons*. *Interlayer excitons* – bound states formed by charge carriers residing in different layers of a heterostructure (figure 2.8a lower panel) – are another possibility. Interlayer excitons can be readily observed in type II heterostructures where an electron from the material with the lower lying conduction band edge bounds to a hole in the material with the higher lying valence band edge as it is shown in figure 2.8b. In the further discussion on properties of interlayer excitons we will consider heterostructures with this type of band alignment.

The spatial separation of charge carriers in interlayer excitons has two important implications. The first one is the increased exciton radius a as compared to an intralayer exciton. In addition, in interlayer exciton the parameter a can be controlled by introducing an insulating spacer (*e.g.* a layer of h-BN) between the semiconducting layers in order to bring electrons and holes further apart[19,63,64]. The possibility to tune a is advantageous because it allows to control and increase the exciton lifetime[65] τ ($\tau \sim a^2$). The enhancement of τ can be very dramatic. For example, from time-resolved measurements[66] the lifetime of an intralayer exciton in WSe_2 monolayer is estimated to be at the order of tens of ps, while the results obtained for an interlayer exciton in $WSe_2/MoSe_2$ heterostructure provide the value of τ of about 100 ns. The long lifetime allows interlayer excitons to propagate over large distances before recombination, which is critical, for example, for optoelectronic applications where these excitons can be used as information carriers[67]. The second consequence of interlayer carrier separation is the formation of an out-of-plane electric dipole moment D_{ex} as it is shown in figure 2.8a. The presence of D_{ex} allows to control the motion of interlayer excitons electrostatically and hence to build functional devices powered by these excitons, for example, exciton optoelectronic transistors[68].

To benefit from the discussed advantages of interlayer excitons, however, they are required to recombine radiatively. An interlayer exciton is optically bright if its kinematic momentum Q_{ex} lies within a photon light cone[70,71] and the optical selection rules, discussed in section 2.1.3, are met. Similarly to intralayer excitons, an efficient radiative recombination of interlayer excitons is achieved when Q_{ex}=0, which is the case for direct band gap semiconductors (*i.e.,* when CBM and VBM are matched in momentum space). In a heterostructure with type II band alignment the conduction and valence band edges originate from different heterostructure components. Their momentum-space coordinates are determined by the band structure and the size of the Brillouin zone of each of the components which, in turn, depends on the material lattice constant. Usually, it is very difficult to find the combination of materials with the same lattice symmetry and lattice constants and thus obtain a direct band gap heterostructure. For example, despite the fact that all group 6 TMD monolayers have their CBM and VBM at the K/-K points, being combined into a heterostructure their band extrema will be displaced relatively to

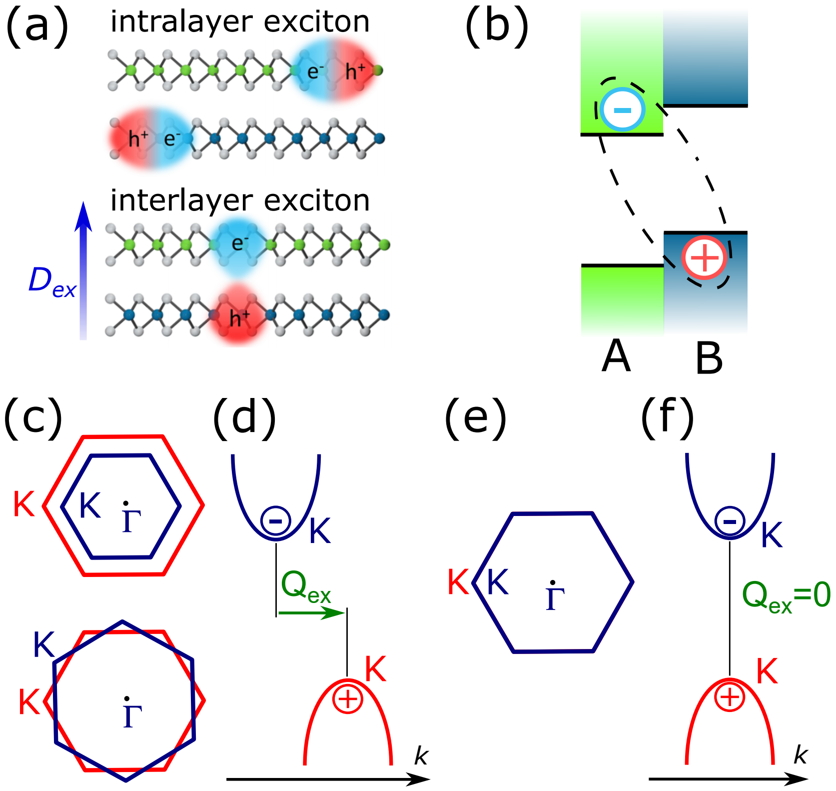

Figure 2.8: (a) Schematic real space representation of intra- and interlayer excitons, taken from Ref. 69. The interlayer carrier separation in an interlayer exciton creates an out-of-plane electric dipole moment D_{ex}. (b) Interlayer exciton in type II semiconducting heterostructures. (c) Brillouin zone alignment between two different TMD monolayers in a vdW heterostructure when the components have different lattice parameters (the upper panel) and when they are the same but the lattices are rotationally misaligned (the bottom panel). In both of these cases the CBM and VBM, lying at the K/-K points, are displaced in the momentum space and interlayer excitons formed in these heterostructures acquires finite kinematic momentum Q_{ex} as shown in (d). When the lattice parameters are the same, as it is the case for $WSe_2/MoSe_2$ heterostructure, and the lattices are aligned (e) then the CBM and VBM match and $Q_{ex} = 0$ (f).

each other in the majority of combinations because of the difference in their lattice constants as shown in figures 2.8c,d. Only for $WSe_2/MoSe_2$ heterostructure, where the lattice mismatch between the constituents is negligible, it is possible to match the CBM and VBM and in which the existence of radiative recombination due to interlayer exciton has been solidly proven experimentally[28,69](see figures 2.8e,f). In the other combinations the lattice difference is large and hence $Q_{ex} \gg 0$ which suppresses radiative interlayer recombination. Furthermore, even if the lattice-matched components are chosen the heterostructure‘s CBM and VBM can be still displaced in the momentum space due to rotational misalignment of the constituent lattices during heterostructure assembly (figure 2.8c bottom panel). So far, achieving radiative recombination of interlayer excitons in vdW heterostructures remains rather challenging and relies on a very limited combination of materials.

The situation can be changed radically if the exciton kinematic momentum Q_{ex} is always zero irrespective of material lattice constant mismatch or rotational twist. That can only be attained when both conduction and valence band edges of a heterostructure are situated in the Brillouin zone center – at the Γ point. Among vdW materials potential candidates for the valence band edge are layers of group 6 TMDs with thicknesses larger than monolayer, in which the VBM is at the Γ point. For the conduction band edge layers of InSe or GaSe can be employed. These heterostructures are discussed in details in *Chapter 8*.

Chapter 3: Experimental techniques and device fabrication

3.1 Ionic liquid FETs

A field effect transistor is a key component of all modern electronic devices. Apart from powering our everyday gadgets a field effect transistor itself can be used as research tool for characterizing materials. One remarkable type of transistors used for purposes of our research is the ionic-liquid gate field effect transistor (IL FET). The vast majority of electronic transport measurements presented in this thesis take advantage of IL FETs. In this section we, therefore, provide an explanation of the operation principle of ionic-liquid gating, discuss details of ionic liquid gated FETs, and the possibility to use them to perform spectroscopy.

3.1.1 Field-effect transistor

To introduce IL FETs we first discuss the operation principle of conventional FETs. Even though there exist several different types of FETs, the common principle behind all these devices is the modulation of the electrical conductance of a device channel with an electric field. A schematic representation of one of these transistors – the metal-insulator-semiconductor field-effect transistor (MISFET) – is shown in figure 3.1a. The main component enabling the change of the FET conductance is the MIS stack composed of a metal gate, a gate insulator, and a semiconductor. This MIS stack acts as a parallel plate capacitor in which charge carriers can be electrostatically accumulated at the gate/insulator and the insulator/semiconductor interfaces[4,62]. Two metal electrodes – the source and the drain electrodes – are deposited to contact the semiconductor layer from two sides. Upon applying a bias voltage V_{DS} between the source and the drain contacts a potential difference is established across the semiconductor which, in the presence of mobile charge carriers, enables the flow of current. The amount of charge carriers present is controlled by the voltage V_{GS} applied between the metallic gate and the source contact (kept at the ground potential) as shown in figure 3.1a.

The mechanism of charge accumulation in a FET can be readily understood by looking at the band diagrams of a MIS stack shown in figures

3.1b,c. Here a p-doped semiconductor (*i.e.*, with the electrochemical potential μ close to the valence band) is considered, but an equivalent mechanism holds also true for the n-doped semiconductor. For V_{GS}=0V (figure 3.1b) no charge accumulation occurs in the semiconductor and the transistor is in the off state. When a negative V_{GS} is applied (figure 3.1c) positive charge carriers are accumulated at the semiconductor/insulator interface. Such local increase in the concentration of charge carriers bends the valence band edge up and brings it closer to μ. The formation of conducting channel occurs once the VBM reaches μ which brings the transistor into the on state. The value of V_{GS} corresponding to the opening of the channel is called the *threshold voltage* V_{th}.

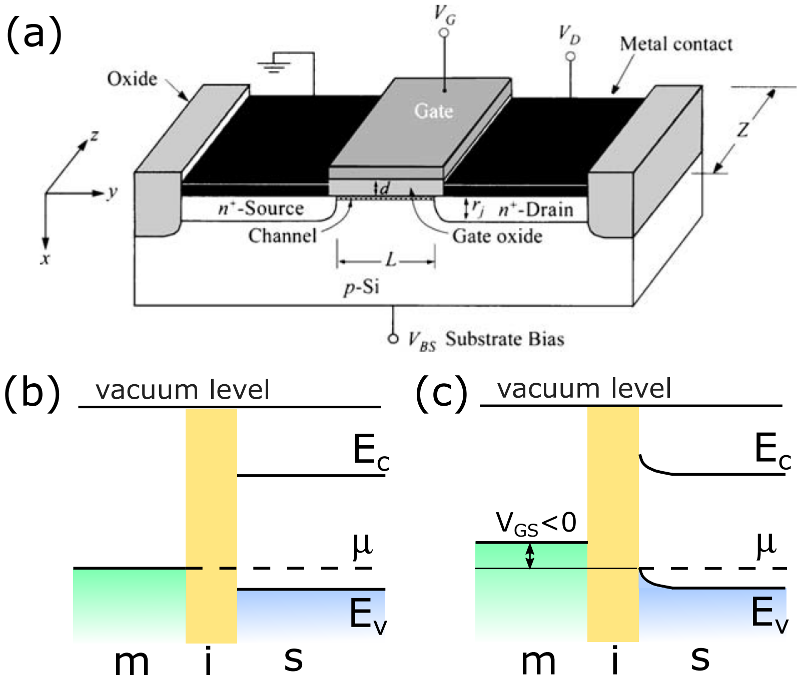

Figure 3.1: (a) Schematics of a MISFET which includes a metal gate separated from a semiconductor channel by a gate insulator and two metal electrodes – the source and the drain electrodes, taken from Ref. 4. The schematics also shows a typical bias configuration enabling MISFET operation. Energy band diagrams for V_{GS}=0V (b) and upon applying a finite negative V_{GS} (c).

When the value of V_{GS} is below V_{th} certain amount of charge carriers are still present in the channel and transistor operates in the *subthreshold regime*. This regime determines how sharply a transistor can be turned on or off. An important figure of merit describing this regime is the *subthreshold swing* defined as:

$$S_{s-th} = ln(10)\frac{k_B T}{q}(1+\frac{C_{ac}}{C_{in}}) \tag{3.1}$$

where C_{ac} and C_{in} are accumulation region and gate insulator capacitance respectively. S_{s-th} represents value of gate voltage required to change the value of source-drain current by one order of magnitude. At room temperature the ultimate limit of S_{s-th} (with $C_{ac} \rightarrow 0$ and $C_{in} \rightarrow \infty$) is equal to 60mV/dec[4].

FET operation regimes

To understand how a FET operates it is important to also look at its current-voltage characteristics (I_{DS}-V_{DS}) which are called *FET output curves.* These curves are obtained by varying the source-drain potential V_{DS} and measuring the source-drain current I_{DS} with fixed value of the gate-source potential V_{GS}. Depending on the values of V_{DS} and V_{GS} a FET can operate in three regimes – *linear*, *saturation* and *ambipolar injection.* To better visualize these regimes we will use a simple but illustrative approach based on diagrams of FET channel potential[72].

To start let us write the Ohm's law in the form of

$$J = \mu^e enE \tag{3.2}$$

where J is the current density, E is the electric field across a FET channel, μ^e and n are the electron mobility and density respectively. For the moment, we discuss electron transport and the hole transport will be treated later. The electric field E can be represented as the derivative of the channel potential V$_{ch}$ with the respect to position in the channel, $E = \partial V_{ch}/\partial x$. For simplicity we consider the linearly varying potential plotted as a solid blue line in figure 3.2b, equal to zero at the source contact and reaching V_{DS} at the drain contact. Even though in real transistors V$_{ch}$ has a more complex spacial dependence the linear approximation is sufficient for the purposes of this chapter. Next, applying a gate voltage V$_{GS}$ between FET source and gate contacts changes the effective potential in the channel which is now determined by V$_{GS}$-V$_{ch}$(x) as shown in figure 3.2c. The 2-d carrier density n accumulated with the gate voltage can be determined from the insulator capacitance and the difference between V_{GS} and the electron threshold voltage V^e_{th}, according to $n(x) = C(V_{GS} - V_{ch}(x) - V^e_{th})/e$. Taking J=$I_{DS}$/W and substituting n and E in (3.2) we obtain the expression for the current in the channel as:

$$I_{DS} = W\mu^e C(V_{GS} - V_{ch}(x) - V^e_{th})\frac{\partial V_{ch}}{\partial x} \tag{3.3}$$

Integrating (3.3) over the channel length L yields:

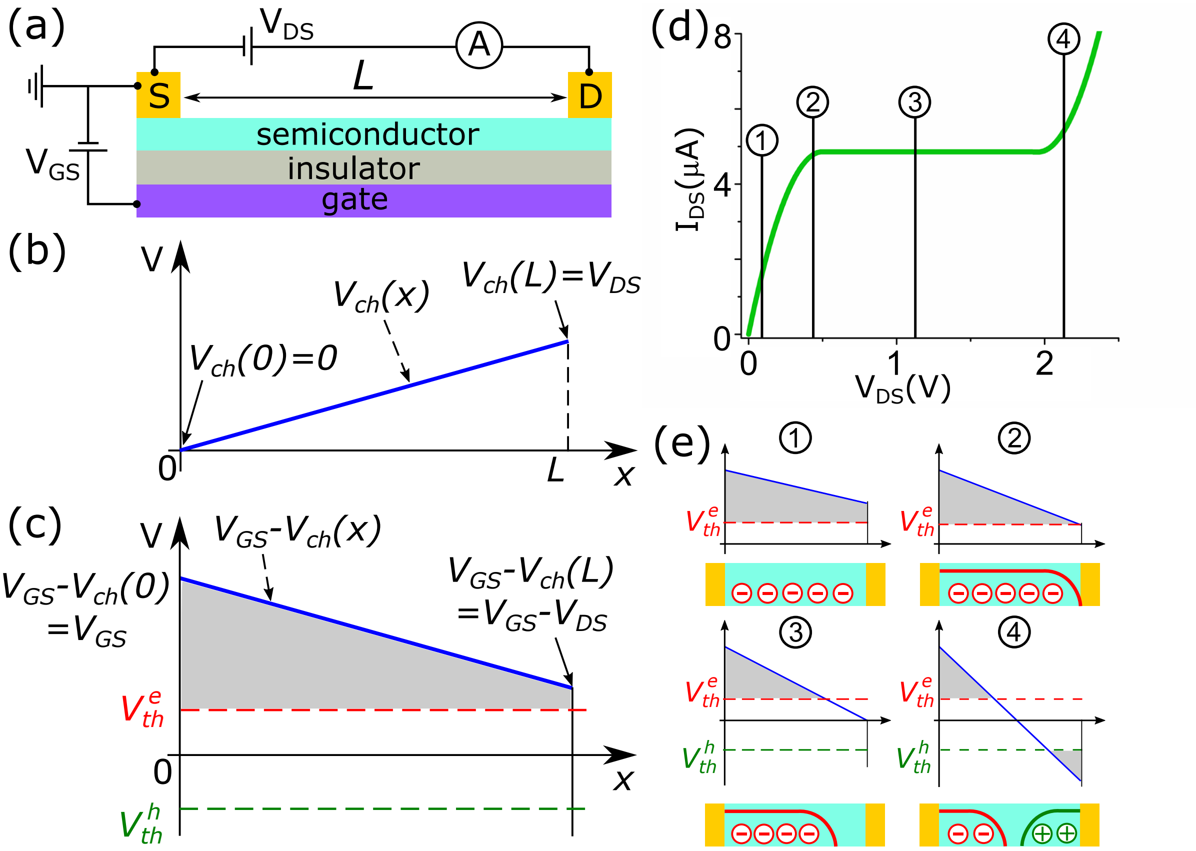

Figure 3.2: (a) Schematics of a MISFET. (b) Variation of channel potential V_{ch} across the channel length when V_{DS} bias is applied between the source and drain contacts. Here we assume linearly varying potential. (c) The effective potential established across the channel when a gate voltage V_{GS} is applied between the source and the gate electrodes. This bias condition ($V_{GS} - V_{DS} > V^e_{th}$) enables accumulation of electrons in the FET channel. The accumulated carrier density is proportional to the shaded gray area. (d) A typical FET current-voltage characteristic (I_{DS} vs V_{DS}). Upon increasing V_{DS} value the FET is brought sequentially into linear, saturation and ambipolar injection regimes. (e) Schematic diagrams of FET channel potential corresponding to FET linear (1), pinch-off (2), saturation (3) and ambipolar injection (4) regimes.

$$\int_0^L I_{DS}dx = \int_0^L W\mu^e C(V_{GS} - V_{ch}(x) - V^e_{th})\frac{\partial V_{ch}}{\partial x}dx \tag{3.4}$$

Linear dependence of $V_{ch}(x)$ on x implies that $\frac{\partial V_{ch}}{\partial x} = \frac{V_{DS}}{L}$. The current is constant across the channel and therefore $\int_0^L I_{DS}dx = I_{DS} \times L$. Thus:

$$I_{DS} = \frac{W}{L} \times \mu^e \times C \int_0^L (V_{GS} - V_{ch}(x) - V^e_{th})dx \times V_{DS} \tag{3.5}$$

The third term in (3.5) is the average induced charge density which can be readily determined from the channel potential diagram from figure 3.2c. We first consider such bias conditions in which the applied effective gate voltage (solid blue line in figure 3.2c) is larger than the electron threshold voltage ($V_{GS} - V_{DS} > V^e_{th}$). In this case the whole blue line lies above the red dashed line marking V^e_{th} and the integral in the third term of (3.5) is simply the area delimited by these two curves $\int_0^L (V_{GS} - V_{ch}(x) - V^e_{th})dx = L(V_{GS} - V^e_{th} - 1/2V_{DS})$, shaded in grey in figure 3.2c. From equation (3.5) we have:

$$I_{DS} = \frac{W}{L}\mu^e C((V_{GS} - V^e_{th})V_{DS} - \frac{V^2_{DS}}{2}) \tag{3.6}$$

When $V_{GS} - V^e_{th} \gg V_{DS}$ the quadratic term in (3.6) can be disregarded. I_{DS} thus varies linearly with V_{DS} and the FET operates in the *linear regime*. In a typical FET output curve, represented in figure 3.2d, this regime is manifested in a linear increase of current at low values of V_{DS}. The corresponding FET channel potential diagram is marked with (1) in figure 3.2e. Under this bias condition only electrons are present inside the channel.

Increasing further V_{DS} brings the effective channel potential closer to the electron threshold voltage. Once the blue line intersects the red dashed line (*i.e.,* when $V_{DS} \geq V_{GS} - V^e_{th}$) the transistor reaches the *pinch-off* (diagram (2) figure 3.2e). Past this voltage the electron channel detaches form the drain contact. The transistor is now brought into the *saturation regime* (diagram (3)) and I_{DS} stays constant:

$$I_{DS} = \frac{W}{2L}\mu^e C(V_{GS} - V^e_{th})^2 \tag{3.7}$$

If V_{DS} is increased even more the effective potential at the drain contact changes its sign. When it becomes more negative than the hole threshold voltage V^h_{th} the transistor enters the *ambipolar injection regime.* Under these conditions both electrons and holes are simultaneously present in the FET channel (see diagram (4) in figure 3.2e) and their spatial distribution can be modulated by V_{DS}. The source-drain current is no longer constant and starts to increase again with V_{DS} as seen in figure 3.2d.

3.1.2 Ionic liquid FETs

In a conventional MISFET a metal gate is separated from the semiconducting channel with a solid insulator, which is typically a SiO_2 layer thermally grown on top of a degenerately doped silicon wafer. In FETs with an ionic liquid gate dielectric – as it becomes clear from its name – the solid gate insulator is replaced by the liquid one. This liquid dielectric is composed of oppositely charged ions which are free to move in the presence of an electric field. A scheme of an IL FET is shown in figure 3.3a. As in the case of a MISFET source and drain electrodes are lying on top of a semiconductor layer. The gate electrode is now, however, displaced from the channel region to the side of the device substrate. An additional electrode, called the reference electrode, is introduced into the device structure. The role of the reference electrode is explained below. A layer of ionic liquid covering the semiconductor channel, the gate and the reference electrodes completes the device.

In this transistor configuration, the modulation of the channel conductivity also occurs through the electrostatic accumulation of charge carriers driven by the potential difference between the source contact and the gate electrode. The applied gate-source voltage V_{GS} attracts ions of opposite charge to the gate/IL and IL/semiconductor interfaces forming two *electric double layers (EDLs)* at these interfaces[73–75]. For example, positive gate voltage brings positive ions at the channel area resulting in the accumulation of electrons in the semiconductor. These EDLs can be thought of as two capacitors with a thickness of about 1 nm. While in MISFETs the potential drop throughout the operation occurs across the whole thickness of the solid insulator in IL FET it happens only at these two EDLs with the rest of the liquid dielectric staying as a neutral mixture of ions. The exact voltage applied to the FET channel is probed with the reference electrode, which eliminates the effect of the potential drop at the gate/IL interface and only measures the drop at the IL/semiconductor interface.

The nanometer thickness of the EDL implies a tremendous increase in the gate capacitance C_G as compared to more conventional devices (*e.g.* the gain compared to a typical MISFET with 300 nm SiO_2 layer is more than two orders of magnitude). The very large gate capacitance is one of the crucial properties of IL FETs, advantageous for a number of applications. For example, it enables to accumulate high density of charge carriers upon applying rather small V_{GS} . The electrochemical potential of a semiconductor can, therefore, be tuned over the large range which is particularly beneficial, for example, for studying ambipolar transport properties in large band gap semiconductors[76,77]. In conventional MISFETs the range of charge carriers that can be accumulated and, hence, the range in which the electrochemical potential of a semiconductor can be tuned is limited by the maximum gate voltage that can be applied determined by the breakdown voltage of the solid insulator. Usually, in these devices it is possible to study transport properties of only one type of charge carriers in a semiconductor (either electrons or holes, depending on the initial doping

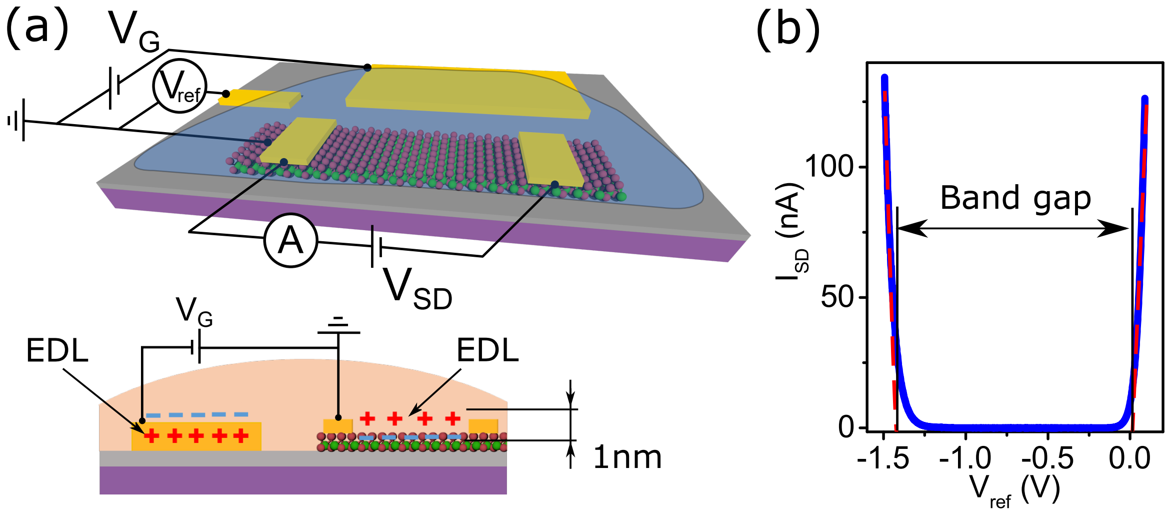

Figure 3.3: (a) Schematics of an ionic-liquid gated FET showing the source and drain contacts, the side gate, and the reference electrode. The diagram also shows the typical bias configuration required for the device operation. The applied gate voltage creates two electric double layers which act as two capacitors at the gate/IL and IL/semiconductor interfaces. (b) Source-drain current I_{DS} as a function of reference voltage V_{ref} acquired from a multilayer MoS_2 IL FET used as an example to demonstrate how value of band gap is determined with IL FET spectroscopy. The red dashed lines are an extrapolation of the FET linear regime to $I_{DS} = 0$ V, as needed to extract the values of electron V_{th}^{e} and hole V_{th}^{h} threshold voltage. The difference between V_{th}^{e} and V_{th}^{h} provides the value of the single-particle band gap.

of a material). In IL FETs the magnitude of the applied gate voltage is also restricted. In this case the allowed V_{GS} values, called the *electrochemical window*, is determined by the chemical stability of the ionic liquid[78]. V_{GS} values outside this window decompose the ions and largely degrade IL FET performance. The electrochemical window strongly depends on the ionic liquid used and it is, therefore, important to properly select the liquid according to the purposes of an experiment. The ionic liquid exploited in this thesis enabled to sweep μ over the conduction band, the band gap and the valence band of the vast majority of the investigated materials and, thus, probe transport characteristics (*e.g.* mobility or charge density) of both electrons and holes.

Another beneficial aspect of ionic-liquid gating is the possibility to realize novel functional devices. For example, IL FETs can be employed as *light-emitting transistors*[77]. As it is discussed in section 3.1.1 under certain bias conditions, hardly reachable in FETs with solid dielectrics, it is possible to simultaneously inject electrons and holes into a FET channel thus creating a *p-n* junction. Electrons and holes upon arriving at the junction can recombine with each other and emit photons. Remarkably, the position of the p-n junction and hence the light-emitting region can be electrostatically controlled with the source-drain bias.

3.1.3 Spectroscopy with IL FETs

As it was mentioned earlier an IL FET is a research tool in itself, because it enables the characterization of different aspects of the electronic properties of the semiconductor integrated into it. In particular, it allows to do spectroscopy of energetic levels of a material and determine, for example, the value of the single particle band gap Δ of a semiconductor[76,77,79,80] or the band alignment in 2D vdW heterostructures[29]. The method is based on the acquisition and analysis of FET transfer characteristics (*i.e.,* I_{DS}-V_{GS} curves). To illustrate the principle of the IL FET spectroscopy we recall that in a FET the change of the gate voltage ΔV_{GS} and the change of the material chemical potential $\Delta\mu$ are linked by the relation[76]:

$$e\Delta V_{GS} = \Delta\mu + e\Delta\phi = \Delta\mu + \frac{e^2 n}{C_G} \tag{3.8}$$

where n is the density of charge carriers, C_G – gate capacitance.

Sweeping the gate voltage V_{GS} in a transistor leads to the change of μ and the variation of the electrostatic potential $\Delta\phi = en/C_G$. For the transistor off-state (*i.e.,* when μ is inside the band gap) value of n corresponds to the density of in-gap states induced by defects or impurities. In high quality materials n is usually low making the numerator in $\frac{e^2 n}{C_G}$ also low. The denominator is the gate capacitance which for IL FETs is extremely large. We can, therefore, neglect the second term in (3.8). This yields $e\Delta V_{GS} = \Delta\mu$, *i.e.,* the change of the gate voltage is directly equal to the change of the position of μ inside the gap. Tuning V_{GS} from the conduction to the valence bands, thus, directly gives the distance in energy between the bands‘ edges which is the value of single particle band gap. The exact value is calculated according to $\Delta V_{gap} = V_{th}^{e} - V_{th}^{h}$. To determine precisely values of electron and holes threshold voltages the FET transfer curve should be measured as a function of reference voltage rather than applied gate voltage V_{GS}. That is because plotting data in this way enables to account only for the potential drop occurring in the FET channel and exclude the one at the gate/IL interface. Values of V_{th}^{e} and V_{th}^{h} are determined by interpolating respective FET linear regimes to I_{DS}=0 as it is shown in figure 3.3b.

3.2 Photoluminescence

In this type of spectroscopy a material is illuminated with a beam of monochromatic light and the resultant emission spectrum is recorded. In simple terms, a sufficiently high-energy photon incident on a semiconductor excites an electron from the valence to the conduction band leaving its positively charged counterpart – a hole – in the valence band. Within a very short time the charge carriers relax to their respective bands‘ extrema (CBM for electrons and VBM for holes). Electron further relaxes back into the valence band (*i.e.,* recombines with hole) and the system returns into the ground state. The recombination can be accompanied by radiative emission or occur via a non-radiative path, as discussed in section 2.1.3. Photoluminescence spectroscopy relies on the measurement of radiative recombination processes, that determine the emission spectrum of the semiconductor.

In TMDs, due to strong Coulomb interaction, an excited electron and a hole in the valence band form a bound exciton state already at room temperature. The photoluminescence output of TMDs is, therefore, mainly dominated by the recombination of excitons rather than unbound electron-hole pairs. In figure 3.4a a typical PL spectrum of a monolayer MoS_2 at room temperature is shown. The spectrum reveals two Lorentzian-like peaks marked with A (the lower energy peak) and B (the higher energy peak). These peaks are due to recombination of excitons composed of carriers residing in the K/-K valleys. The emergence of two peaks is caused by the large spin splitting of the valence band at the K/-K points. PL spectroscopy also allows to resolve transitions due to indirect excitons. These transitions have, however, much lower intensity as it is seen, for example, for the indirect Γ-Q exciton in MoS_2 bilayer marked with I in figure 3.4a.

Photoluminescence excitation spectroscopy

In a typical PL experiment the excitation energy of a laser is adjusted to probe the transition of interest in resonance in order to maximize the number of outcoming photons. In the presence of several distinct transitions responsible for radiative recombination it appears useful to be able to continuously vary the energy of excitation to establish their relative contributions. The technique in which the PL spectrum is acquired as a function of the laser excitation energy is called *photoluminescence excitation spectroscopy* (PLE). This type of spectroscopy is particularly beneficial for studying interlayer excitons in type II heterostructures. The intensity of the interlayer exciton is largely determined by the amount charge carri-

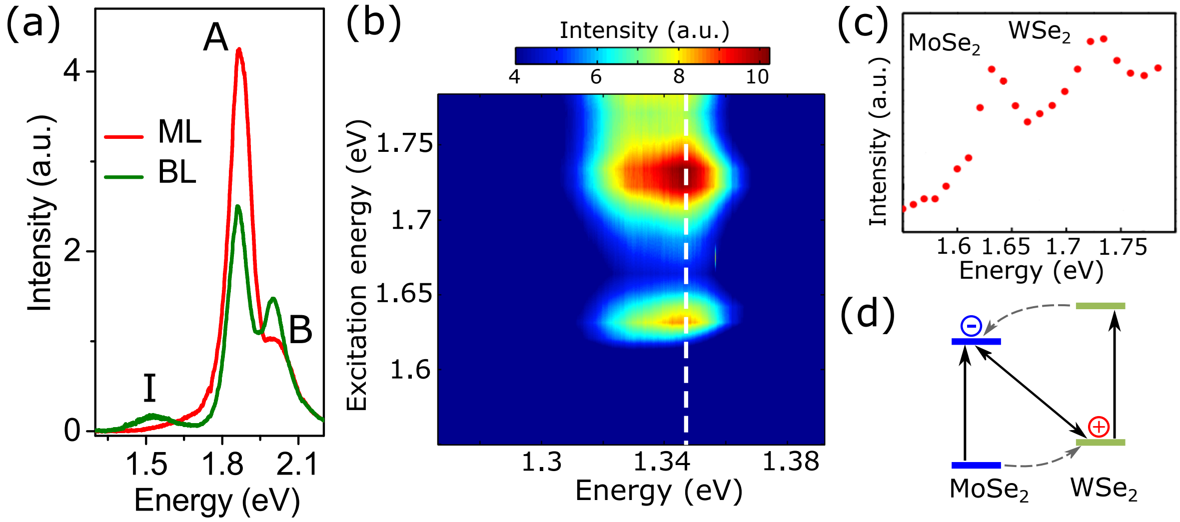

Figure 3.4: (a) Photoluminescence spectra of mono- and bilayer MoS_2 showing peaks due to A and B excitons for the monolayer and additional low energy peak due to indirect Γ-Q exciton for the bilayer. (b) Photoluminescence intensity of interlayer exciton as a function of laser excitation energy (PLE map) for $WSe_2/MoSe_2$ heterostructure. The enhancement of the interlayer peak occurs at energies corresponding to the intralayer excitons of WSe_2 (1.74 eV) and $MoSe_2$ (1.64 eV) as it is seen in (c) where the PL intensity along the white dashed line is plotted. (d) Band alignment diagram of $WSe_2/MoSe_2$ heterostructure. Figures (b)-(d) are adapted from Ref. 28.

ers at the respective conduction and valence band edges of heterostructure constituents. The resonant population of these bands, in turn, occurs at the excitation energies matching the band gaps of the constituents. An example of a PLE plot is shown in figure 3.4b where PL spectral intensity of the interlayer exciton is mapped as a function of excitation energy for $WSe_2/MoSe_2$ system[28]. The pronounced increase of the interlayer exciton peak intensity (see figure 3.4c, d) occurs at the energies corresponding to the intralayer exciton states of WSe_2 (1.74 eV) and $MoSe_2$ (1.64 eV) which serves as a solid indication that this peak is indeed due to interlayer recombination.

3.3 Photocurrent

In this technique current in a semiconductor generated by the photoexcitation (*i.e.*, the photocurrent) is probed as a function of energy of the incoming light. Unlike PL spectroscopy, where the investigated sample acts as an emission source and the outcoming photons are detected with an external instrument, in photocurrent spectroscopy the sample itself is the detecting device. A photocurrent experiment is done by attaching two metallic contacts to a sample as shown in figure 3.5a. There exist several ways to measure photocurrent. One of the possibilities, which is used in experiments described in this thesis, is to put both electrodes at the same ground potential. In this configuration the contacts are short-circuited and the resultant photogenerated current is called the *short-circuit current* I_{SC}. Throughout the measurements a laser beam is positioned close to one of the contacts and the value of I_{SC} is recorded while changing the laser excitation energy.

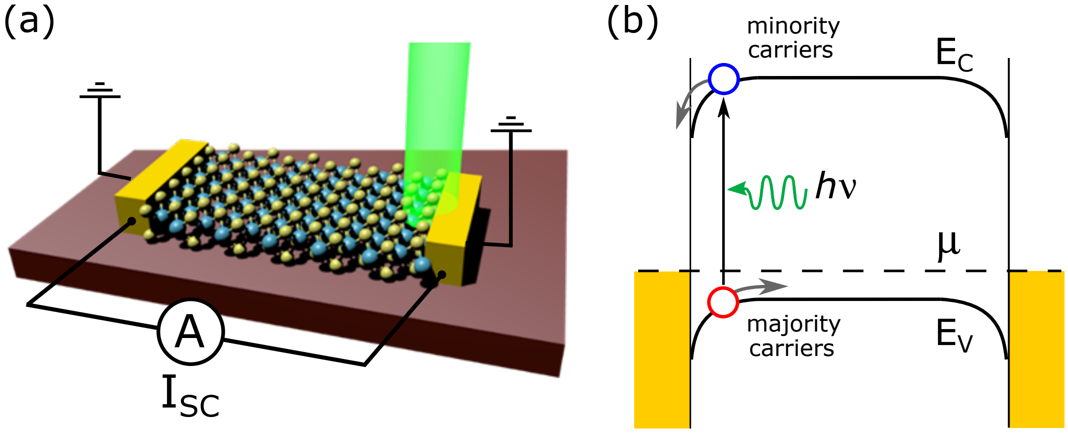

Figure 3.5: (a) Schematics of a device for a photocurrent experiment. The photocurrent I_{SC} is measured in the short-circuit configuration where both of electrodes are put at the same ground potential. (b) Energy band diagram of a metal/semiconductor junction. The potential barrier established at the junction interface favours the drift of the minority carriers towards the contact and opposes the majority carriers from entering the contact.

The common microscopic picture to understand the emergence of photocurrent is the spatial separation of photoexcited charge carriers by an electric field. For the sake of simplicity here we discuss only the case of photocurrent generated by an electric field at the metal/semiconductor interface. Let us first recall the band alignment at this interface. Bringing a metal and a semiconductor into contact leads to the alignment of the electrochemical potential on both sides of the junction. In the semiconductor, this results in bending of the valence and conduction bands at the interface as discussed in section 2.2.1 and depicted in figure 3.5b. In this specific case, and if we consider a p-doped semiconductor, band bending creates a potential barrier (the Schottky barrier), for holes (the majority carriers), which prevents them from entering the metal contact. For electrons (the minority carriers), however, such band bending favours their drift into the contact. Thus, upon optical excitation, it is the minority charge carriers that exit the semiconductor and contribute to the photocurrent[81]. The picture of carrier extraction is equivalent for n-doped semiconductors (with the only difference that the minority carriers in that case are holes).

This quantitative discussion is based on the idea that photoexcited states consist of separate electrons and holes. In TMDs, however, it is not the case because the vast majority of optically excited carriers are bound into excitons already at room temperature. To identify contribution of excitons to the photocurrent they are required to dissociate. In the discussed experimental set-up splitting of excitons is achieved due to the built-in voltage present in the contact area. Note that photocurrent is generated irrespectively of whether an exciton is optically bright or dark. It is the major advantage of this technique as compared to the photoluminescence spectroscopy.

3.4 Raman spectroscopy

Raman spectroscopy measures inelastic scattering of monochromatic light that, in the case relevant for our work, is caused by molecular or crystalline vibrations in the material investigated. Raman scattering includes three steps as shown in figure 3.6a. In the first stage, an incident photon with energy $\hbar\omega_i$ excites an electron in the sample into a virtual electronic state. The particle in the excited state can interact with vibration of the crystalline lattice, so-called *phonons*, upon gaining or losing energy $\hbar\omega_{Ph}$ where ω_{Ph} is the frequency of the excited vibrational mode. Finally, the excited electron collapses back into the ground state by emitting a photon. The difference in energy between the incident and the emitted photon gives rise to the Stokes (when $\hbar\omega_i - \hbar\omega_{Ph}{>}0$) and anti-Stokes (when $\hbar\omega_i - \hbar\omega_{Ph}{<}0$) lines in the Raman spectrum. The intensity of Raman-scattered light is usually plotted as a function of Raman shift Δk:

$$\Delta k = \frac{1}{\lambda_i} - \frac{1}{\lambda_{sct}} \tag{3.9}$$

where λ_i and λ_{sct} are wavelengths of incident and scattered photons respectively. The emission line at Δk=0, called the Rayleigh line, corresponds to elastic scattering *i.e.,* the one that does not involve any energy loss or gain (see figure 3.6b). Typically, the Rayleigh scattering dominates as only 1 out 10^6 photons are inelastically scattered.

Phonons in a material can be either Raman active or not depending on the symmetry of the crystalline lattice. In TMDs several phonon vibrational modes are resolved with Raman spectroscopy. For example, for 2H monolayer MoS_2 there are two characteristic modes[82] marked with E_{2g} and A_{1g} in the spectrum of figure 3.6c. The E_{2g} mode correspond to the in-plane oscillation of atoms while the A_{1g} mode – to the out-of-plane vibrations as depicted in the inset of figure 3.6c. The positions of these peaks can be used to detect thickness[82] and quantify strain present in the material[83].

In this thesis the Raman spectroscopy is primarily used to probe the electron-phonon interaction in TMDs as a function of accumulated charge carrier density. A simple picture of the electron-phonon interaction can be represented in the following way. In solids ions of crystalline lattice oscillates around their equilibrium positions creating, thus, locally an electrostatic potential. This potential, known as deformation potential, affects the mobile charge carriers present in the material. In turn, changing the number of free carriers also influence the vibration frequency of a lattice

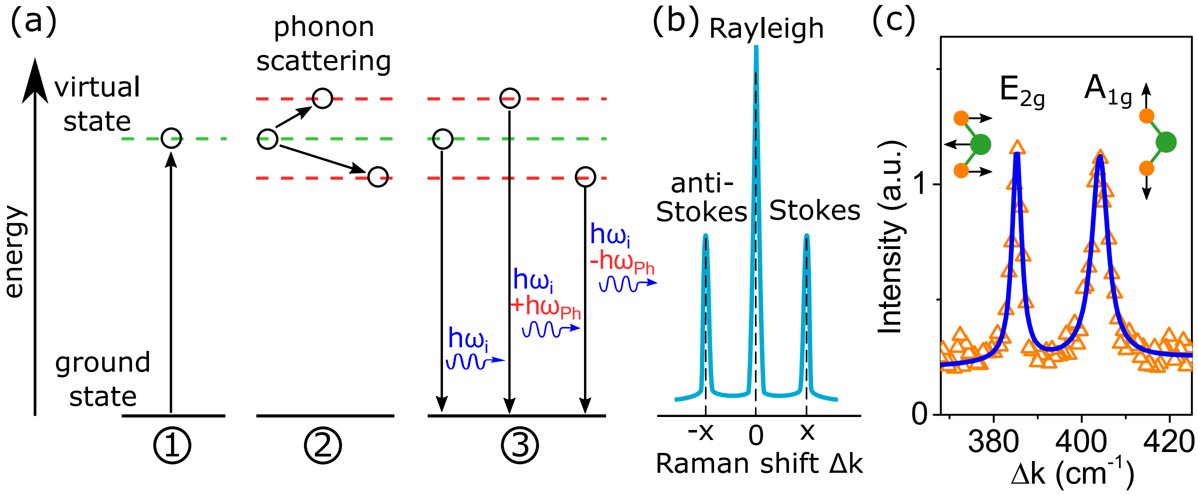

Figure 3.6: (a) The sequence of Raman scattering process which includes the excitation of an electron in a sample into a virtual electronic state, subsequent inelastic scattering with lattice vibration and the final collapse of the excited state back into the ground state with emission of a photon. (b) Schematic representation of Raman spectrum showing Rayleigh, Stokes and anti-Stokes lines. (c) Raman spectrum of MoS$_2$ monolayer showing the characteristic E_{2g} and A_{1g} vibrational modes.

and thus shifts the energy of phonon vibrational modes. The change in frequency of the Raman modes $\Delta\omega$ due to electron or hole accumulation is linked to the magnitude of the electron-phonon coupling (EPC) g according to:

$$\Delta\omega_\nu \approx -N(\varepsilon_F)\langle g_\nu^2\rangle_{FS}. \tag{3.10}$$

where $N(\varepsilon_F)$ is the density of states at the Fermi energy, ε_F, and $\langle g_\nu^2\rangle_{FS}$ is the screened electron-phonon coupling (squared) for the ν-th phonon mode averaged over the entire Fermi surface. The EPC in TMDs is discussed in details in *Chapter 6*.

3.5 Device fabrication

In this section we describe the sequence of fabrication steps employed to make samples used in optical and electronic measurements. We start with two synthesis approaches, micromechanical exfoliation and chemical vapor deposition, followed by the transfer technique used to assemble van-der-Waals heterostructures and the fabrication technique utilized to build actual devices.

Exfoliation

The first method which enabled to successfully obtain atomically thin layers of van-der-Waals materials is micromechanical exfoliation or simply exfoliation. This rather straight forward from today‘s standpoint technique opened up the complete experimental field of 2D materials and determined its fast expansion. Here, a piece of bulk crystal, which is either extracted from naturally occurring mines or synthesized with a chemical vapor transport, is attached to a stripe of scotch tape as shown in figure 3.7a. It is then thin downed by putting a second stripe of tape on the other face of the crystal and detaching it further (figure 3.7b). This step is iteratively repeated until the required crystal color, roughly corresponding to the thickness and density of material crystallites yielding atomically thin flakes, is achieved as shown in figure 3.7c. Such scotch tape is deposited on a Si/SiO_2 substrate, which is cleaned prior to use sequentially in nitric acid, deionized water and isopropanol. After rubbing the substrate/tape stack for approximately 5 minutes (figure 3.7d) the scotch stripe is slowly detached. The substrate is further inspected under an optical microscope to find flakes of the required thickness which is established using combination of optical contrast, atomic-force microscopy and photoluminescence measurements. Optical microscope images of a Si/SiO_2 substrate after exfoliation are shown in figures 3.7e,f.

Chemical vapor deposition

Exfoliation method despite its great success in obtaining high quality 2D materials, is facing a principal limitation that it cannot be scaled-up to produce large-area layers. An alternative approach to overcome this issue is chemical vapor deposition (CVD). In this technique a continuous film of a material is formed on a growth substrate via chemical reaction between precursors. For example, the growth of a CVD monolayer of MoS_2 , discussed in *Chapter 4*, occurs through the reaction of Mo-containing compound MoO_3 with sulfur. The exact protocol used in this thesis includes the following steps. Ceramic crucibles loaded with powders of MoO_3 and sulfur

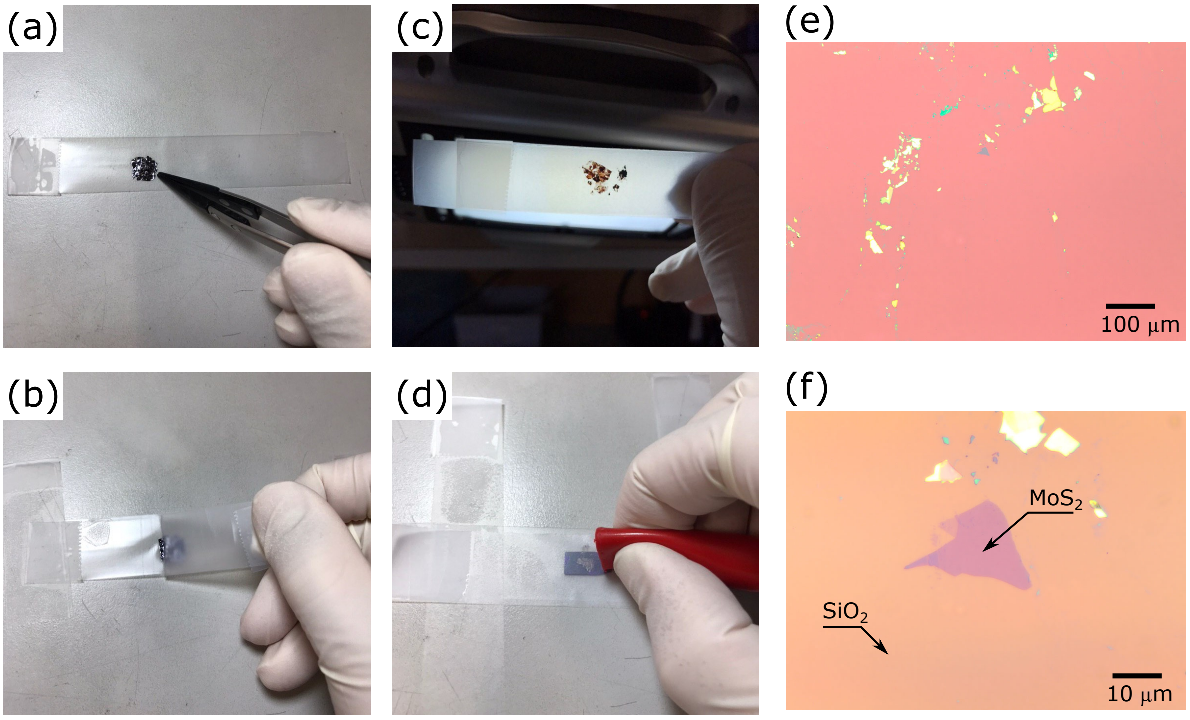

Figure 3.7: (a)-(d) Sequence of steps showing the process of exfoliation of vdW materials. (e),(f) Optical microscope images of Si/SiO$_2$ substrate after exfoliation containing MoS$_2$ flakes of different thickness.

are put into a tube furnace in the way that the one with MoO$_3$ is positioned in the middle of the furnace and the one with sulfur approximately 20 cm upstream as schematically depicted in figure 3.8a. As a growth substrate a polished c-plane sapphire is used which is placed "face-down" on a holder above the MoO$_3$-containing crucible. Sapphire substrate enables epitaxial growth of MoS$_2$ monolayers which significantly improves its properties as compared to the other growth substrates[58]. The synthesis is done under constant flow of Ar (75 sccm) with the temperatures of MoO$_3$ and sulfur reaching 700 and 250 °C, respectively. The growth of the CVD film starts from formation of multiple triangular-shaped crystallites distributed along the substrate. Their size increases continuously throughout the deposition until they eventually merge into a continuous film (figure 3.8b).

Transfer

2D van-der-Waals materials, as it is discussed in section 2, can be freely assembled into van-der-Waals heterostructures by stacking the required combination of components. In this work we exploit the so-called dry-transfer technique which is based on the use of polycarbonate (PC) transfer stamps[84]. These stamps are fabricated according to the following procedure. First, a solution of polycarbonate granules in chloroform with concentration of 50mg/ml is prepared, which is then spin coated on a glass

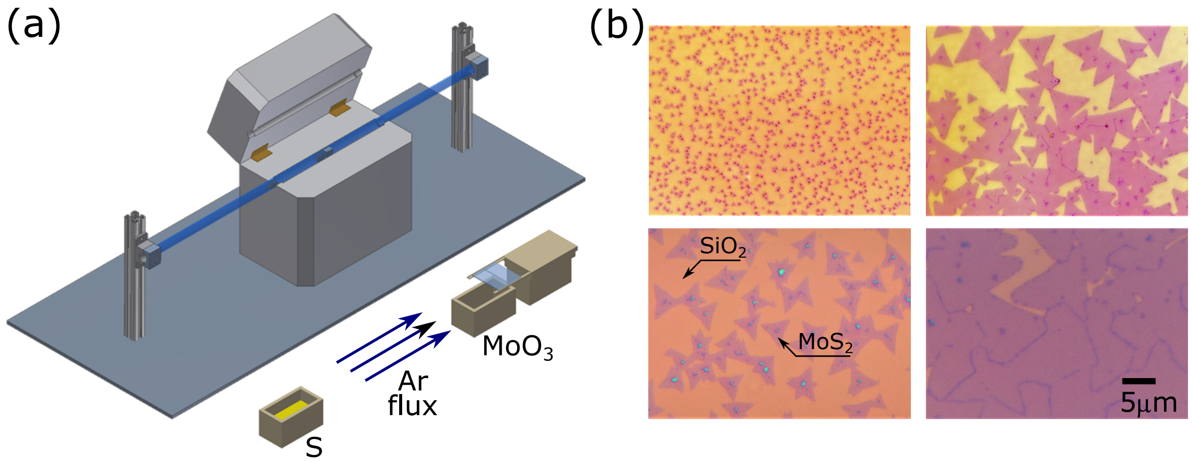

Figure 3.8: (a) Schematics of a CVD set-up. (b) Optical microscope images of CVD MoS$_2$ monolayers representing different growth stages.

plate at 3000 rpm for 60 seconds. The obtained PC film is detached from the substrate and positioned on top of a glass plate/PDMS stack where it is fixed with a scotch tape. The final stamp is baked at 100 °C for 60 seconds. The optical image of a typical PC stamp is shown in 3.9a.

The transfer itself is done on an in-house built transfer stage inside a glove box with controlled nitrogen atmosphere. The PC stamp is clamped in vacuum holder and positioned on top of the area of a substrate containing a flake to transfer. It is further brought to the contact with the flake using micromechanical manipulator and heated up to 120 °C. Right after reaching 120 °C the stamp is cooled down to 70 °C and lifted up. The flake is thus picked up from the substrate. In the next step, the stamp with the flake is aligned and brought to the contact with a target substrate and then heated up to 180 °. Immediately after achieving this temperature the stamp is lifted up leaving the flake covered with the PC film on the substrate (at T=180 °C the PC film detaches from PDMS). The substrate is then put into chloroform to remove PC residues.

Electron beam lithography and contact deposition

Patterning of a flake or a CVD layer into an actual device used in electronic transport measurements is done by electron-beam lithography. In this technique a film of positive e-beam resist (polymethyl methacrylate (PMMA)) is spin-coated on a substrate containing a flake and baked at 180 °C for 2 min. The substrate with the resist is patterned with electron beam according to the design and then developed in IPA/water solution. In the next step a metal film is deposited on top of the PMMA mask using electron beam evaporation. The final device is obtained after lift-off done

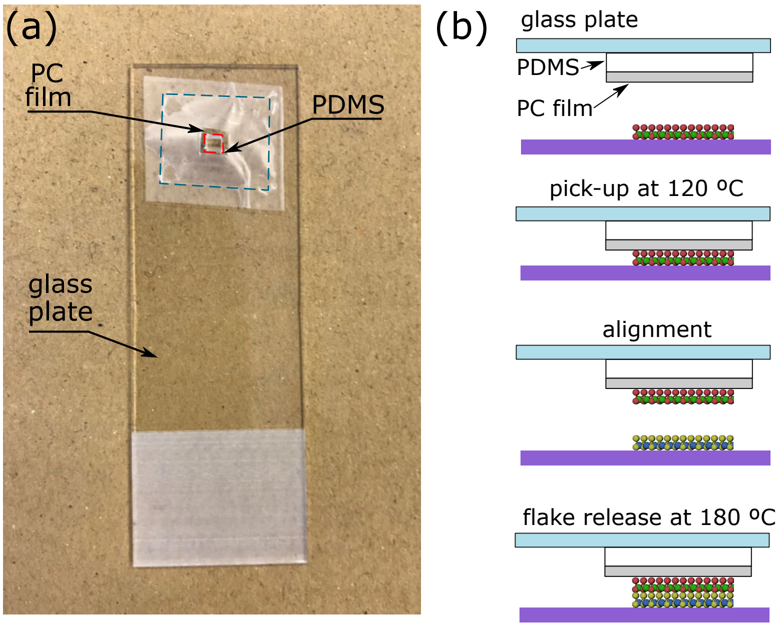

Figure 3.9: (a) Optical image of a PC stamp used to assemble vdW heterostructure with the dry-transfer technique. The PC film and the PDMS stamp are delimited by the blue and the red dashed rectangles respectively. (b) The main steps illustrating the transfer procedure.

by dissolving the PMMA mask in acetone.

Chapter 4: Ambipolar light-emitting transistors on chemical vapor deposited monolayer MoS$_2$

4.1 Introduction

Monolayers of semiconducting transition metal dichalcogenides (TMDs) based on molybdenum and tungsten are at the focus of considerable attention because their electronic properties enable the investigation of interesting physical phenomena and offer a significant potential for future applications[85,86]. These monolayers are direct band-gap semiconductors that interact strongly with light, properties that make them attractive for the realization of opto-electronic devices[87]. Indeed, a variety of structures – such as photodetectors[88], solar cells[89,90], light-emitting diodes[89–92] and light-emitting transistors[77] – has been investigated and shown to be promising either because of their particularly good performance (*e.g.* very high sensitivity of photo-detectors[88]) or of their rather unique functionality (*e.g.* the possibility to control the emission of circularly polarized light[93]).

So far, the vast majority of opto-electronic devices based on semiconducting monolayer TMDs has relied on individual flakes exfoliated from bulk crystals. Nevertheless, the development of a viable technology will require the realization of structures produced through a controllable and scalable process. Progress in this direction is well on its way, as the growth of large-area, high-quality atomically thin layers (down to monolayers) of MoS$_2$[58,94–100], MoSe$_2$[101,102], WS$_2$[103] and WSe$_2$[104] has already been demonstrated by means of chemical vapor deposition (CVD). CVD-grown atomically thin layers of semiconducting TMDs have indeed started to be used for the realization of integrated circuits[105], gas- and photosensors[106], and flexible transistors[107]. Only limited work, however, has focused on opto-electronic applications, possibly because most opto-electronic functionalities rely on the occurrence of ambipolar transport, which is extremely difficult to observe experimentally in CVD-grown monolayers of semiconducting TMDs. Indeed, ambipolar transport in CVD-grown mono-

---

The results presented in this chapter have been published as Evgeniy Ponomarev, Ignacio Gutiérrez-Lezama, Nicolas Ubrig, and Alberto F. Morpurgo, *Nano Lett.*, ***2015***, *15* (12) layers has been reported for the first time only recently in WSe_2,[108] and its observation required sweeping the gate voltage by approximately 200 V, a range by far not compatible with practical applications.

Here, we report on the use of high-quality, large area CVD-grown MoS_2 monolayers to realize ionic liquid (IL) gated field effect transistors (FETs) that work both in electron and hole accumulation. We exploit these ambipolar FETs to perform two different types of experiments. First, we take advantage of the very large capacitance of the ionic liquid gate to quantitatively estimate the single particle band gap Δ of MoS_2 monolayers directly from the FET transfer curve, a measurement that could not be done until now because – contrary to the case of thicker MoS_2 layers[109] – ambipolar transport in monolayer MoS_2 had not been reported yet. From measurements on different devices, we obtain values of Δ ranging from 2.4 to 2.7 eV. Secondly, we drive our ionic liquid gated FETs in the ambipolar injection regime, in which charge carriers of opposite polarity are injected at the source and drain contacts. In this regime, we detect electroluminescence at the energy corresponding to recombination of excitons in monolayer MoS_2, from the region close to the hole injecting contact. A detailed analysis of the spectra of the emitted light and of their evolution with applied bias shows – consistently with the result of gate-dependent transport measurements – that the confinement of the light emission near the contact region is caused by impurity states broadly distributed in an energy range of 250-300 meV above the top of the valence band, acting as deep traps for holes. Our results lead to an internally consistent microscopic scenario accounting for the observed transport properties and electroluminescence of monolayer MoS_2. Additionally, they demonstrate the possibility to employ large-area CVD-grown MoS_2 monolayers to realize ambipolar devices enabling light emission and operating on a voltage scale compatible with practical applications, a conclusion that has technological relevance for the development of opto-electronic devices based on atomically thin semiconducting TMDs.

4.2 Growth and characterization of CVD MoS_2 monolayers

Large-area MoS_2 monolayers are grown by CVD on sapphire substrates through chemical reaction of a molybdenum containing precursor (MoO_3) and sulfur, adapting a protocol reported in Ref. 18. In short (see Ref. 18 for details), crucibles with the precursors are loaded into a tube furnace, so that the MoO_3 powder is positioned in the middle of the furnace and the sulfur approximately 20 cm upstream. The substrate is placed 'face-down' on top of the crucible containing MoO_3. The growth is done under a constant flow of Ar (75 sccm) with the temperatures of MoO3 and sulfur reaching 700 °C and 250 °C respectively. As shown in Ref. 58, this process – in combination with the use of polished c-plane sapphire substrates – enables the epitaxial growth of MoS_2 monolayer with a very small number of tilted grain boundaries. An image of a synthesized MoS_2 monolayer is shown in figure 4.1a (the red arrows point to the edges of the film).

The monolayer nature and the uniformity of the material are assessed by optical characterization. Figure 4.1b shows a Raman spectrum of a CVD-grown MoS_2 monolayer (red curve) together with the spectrum of a bare sapphire substrate (blue curve). The peaks at 384.4 cm^{-1} and 404.6 cm^{-1} (see figure 4.1c), only visible after the growth process, correspond to the E^1_{2g} and the A_{1g} vibrational modes characteristic of crystalline MoS_2. Their precise energy provides a first indication that the material is indeed a monolayer[82]. This is confirmed by the photoluminescence (PL) spectrum shown in figure 4.1d[38,110] (purple curve). A peak at approximately 660 nm (1.88 eV) is seen, due to the recombination of so-called A-excitons, which matches the peak measured on exfoliated MoS_2 monolayers (green curve; similarly to what reported previously[58,100] the higher energy shoulder originating from the B-exciton transition that is seen in the exfoliated monolayer is not detected in the CVD-grown material). We conclude that both Raman and PL measurements show that the material grown is monolayer MoS_2.

To probe the material homogeneity we map the PL signal by illuminating as-grown monolayers locally with a laser beam (the spot size is approximately 1 μm in diameter). We focus on the energy of the A-exciton peak and its full width at half maximum (FWHM), which are sensitive to defects[111] and impurities[112]. Maps of these two quantities are shown in figure 4.1e, f. Except for individual points (originating from a glitch in the measurements), the A-exciton energy ranges from 657.3 to 662.6 nm (*i.e.,* from 1.871 to 1.887 eV) and the FWHM from 22.1 to 26.6 nm (*i.e.,* from 63.5 to 76.4 meV). We compare these ranges with the spread measured on five distinct exfoliated MoS_2 monolayers, for which the peak position varies in the range 657.8-672.5 nm (1.844-1.885 eV) and the FWHM ranges from 23.6 to 36.9nm (67.5-101.1 meV). Our large-area CVD-grown monolayers, therefore, exhibit smaller spread in optical properties than the sample-to-sample variations found in individual MoS_2 monolayers exfoliated from bulk crystals. We conclude that the homogeneity of our CVD-grown MoS_2

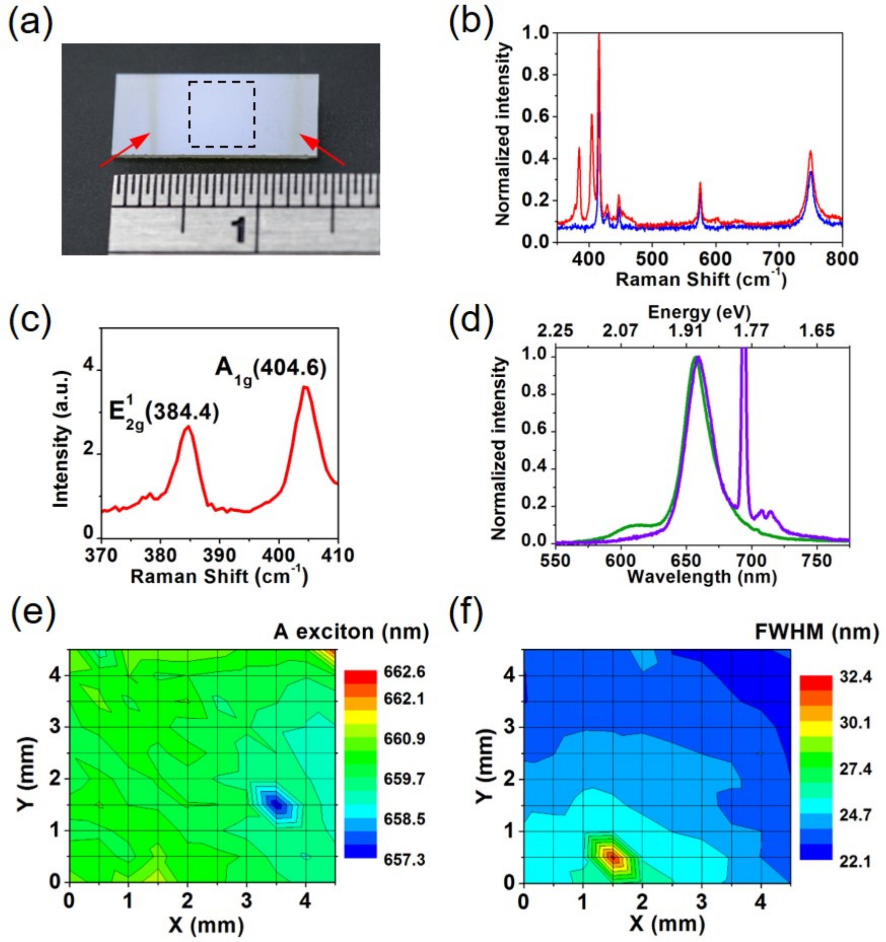

Figure 4.1: Raman and photoluminescence spectra of CVD-grown MoS$_2$ monolayers. (a) Optical image of CVD-grown MoS$_2$ on a sapphire substrate. The red arrows point to the edges of the MoS$_2$ monolayer; the dashed square delimitates the area on which the Raman and photoluminescence spectra shown in (e) and (f) were measured. (b) Raman spectra of a CVD-grown MoS$_2$ monolayer on sapphire (red) and of the bare sapphire substrate (blue). (c) Portion of the Raman signal originating from CVD-grown MoS$_2$, exhibiting the characteristic E^1_{2g} and A_{1g} peaks found in monolayers. (d) Comparison between the photoluminescence spectra of CVD-grown (violet) and exfoliated (green) monolayer MoS$_2$. The peaks observed in the CVD monolayer at about 1.78 eV and lower energies originate from the sapphire substrate (the peak at about 2.05 eV seen in exfoliated MoS$_2$ is due to B-exciton recombination). Maps of the A exciton position (e) and full width at half maximum (f) extracted from the photoluminescence spectra measured on CVD-grown MoS$_2$.

monolayers is satisfactory.

4.3 Ambipolar transport and band gap determination

Electronic transport measurements are done using FETs realized on as-synthesized material (see figure 4.2a for a schematic illustration of the devices and the inset of figure 4.2b inset for an optical microscope image of an actual device). The gold electrodes used to measure transport, a planar gate electrode and an additional contact acting as reference electrode are realized using electron-beam lithography, metal evaporation, and lift-off. A subsequent annealing step in an inert Ar atmosphere is performed at T = 200 °C to lower the contact resistance[113]. A small droplet of ionic liquid (EMI-TFSI) is deposited on top of the devices[73–75] just before loading the them into a vacuum chamber (p$\sim 10^{-6}$ mbar), where they are kept at room temperature overnight (to pump out humidity and oxygen) before starting the electrical measurements. Using FETs realized in this way allows us to measure transport without the need to mechanically transfer the MoS_2 monolayers onto a different substrate, a step that can easily introduce defects detrimental for the observation of ambipolar transport.

Figure 4.2b-d show representative transfer curves (current I_{SD} as a function of gate voltage V_G for different values of source-drain bias V_{SD}) and output curves (current I_{SD} as a function of V_{SD} for different V_G values) of our devices measured under electron accumulation. Virtually no hysteresis is observed upon increasing the gate voltage and sweeping it back, as long as the maximum value of V_G remains within a few hundreds milliVolts from threshold (see figure 4.2b). Increasing the range over which V_G is swept results in a larger hysteresis (see figure 4.2c) and is accompanied — upon repeated cycling of V_G — by a shift in threshold voltage to lower values, in complete analogy to what is commonly observed in IL-gated devices realized on exfoliated flakes. The value of the square resistance $R_\square$ for $V_G \sim 1$ V above threshold is approximately 10 kΩ, only slightly larger than the value measured on exfoliated MoS_2 monolayers at a comparable gate voltage. At this same gate voltage we measure the carrier density from Hall-bar shaped devices identical to the ones discussed here (see section 4.6.1 for details) and obtain $n \sim 10^{14}$ cm^{-2}, from which we extract the room-temperature electron mobility to be $\mu = 1/(R_\square ne) \sim 10$ cm^2 V^{-1}s^{-1}. This value is comparable to what has been reported earlier for exfoliated and (top-quality) CVD MoS_2 monolayers[98,99,114].

The current upturn seen past the saturation regime at large positive V_{SD} and small (to moderate) V_G values is worth commenting (see figure

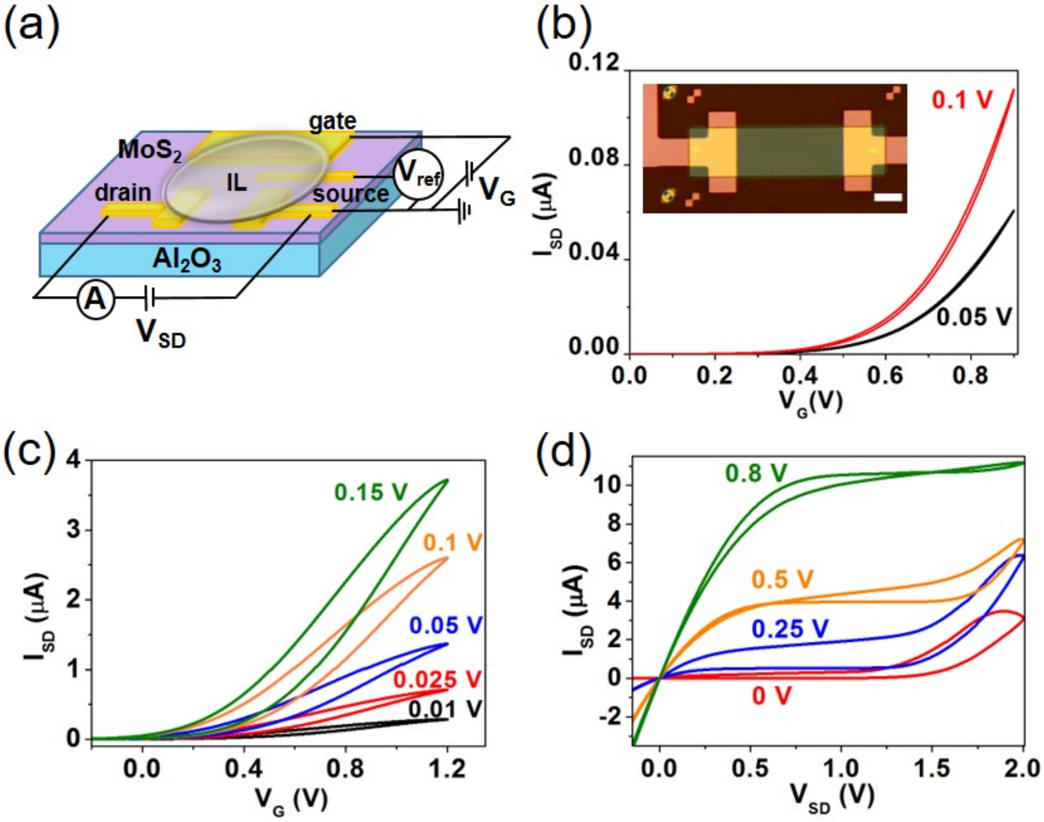

Figure 4.2: Electrical characteristics of monolayer MoS_2 ionic liquid-gated field-effect transistors. (a) Scheme of an ionic liquid-gated field-effect transistor (FET) realized using an as-synthesized MoS_2 monolayer, showing the source and drain contacts, the side gate and the reference electrode. (b) Source-drain current I_{SD} under electron accumulation measured for two values of source-drain bias V_{SD} as a function of gate voltage V_G (FET transfer curves). The inset shows an optical microscope image of a device, in which the channel is defined by a window made in a PMMA layer (so that the IL is in contact with the MoS_2 only in this region). The scale bar in the inset corresponds to 20 μm. (c) Transfer curves of the same device shown in (b), showing a larger gate sweep range (that ultimately results in the occurrence of hysteresis, as commonly seen in devices based on exfoliated MoS_2 monolayers). (d) I_{SD} as a function of V_{SD} for different V_G values (FET output curves) showing the typical behavior observed in an ambipolar transistor (*i.e.*, an upturn in I_{SD} is seen at sufficiently large V_{SD}, past the saturation regime).

4.2d for $V_{SD} = 1.5$ V or larger). It is an experimental manifestation of the onset of the ambipolar injection regime, in which electrons and holes are simultaneously injected at the two opposite contacts in the transistor[115], and it implies the occurrence of ambipolar transport. This observation is interesting because – contrary to monolayers of other semiconducting TMDs – for MoS_2 monolayers the manifestation of ambipolar conduction had not been reported yet (neither on exfoliated nor on CVD-grown material). To confirm the occurrence of ambipolar conduction we measure the full transfer characteristic by sweeping V_G up to large negative values. Figure 4.3a shows the source drain current I_{SD} measured at $V_{SD} = 0.5$

V, as a function of the potential of the reference electrode (V_{ref}), as is necessary to estimate the band gap (see below). The occurrence of hole conduction when V_{ref} exceeds (in absolute value) -2 V is apparent.

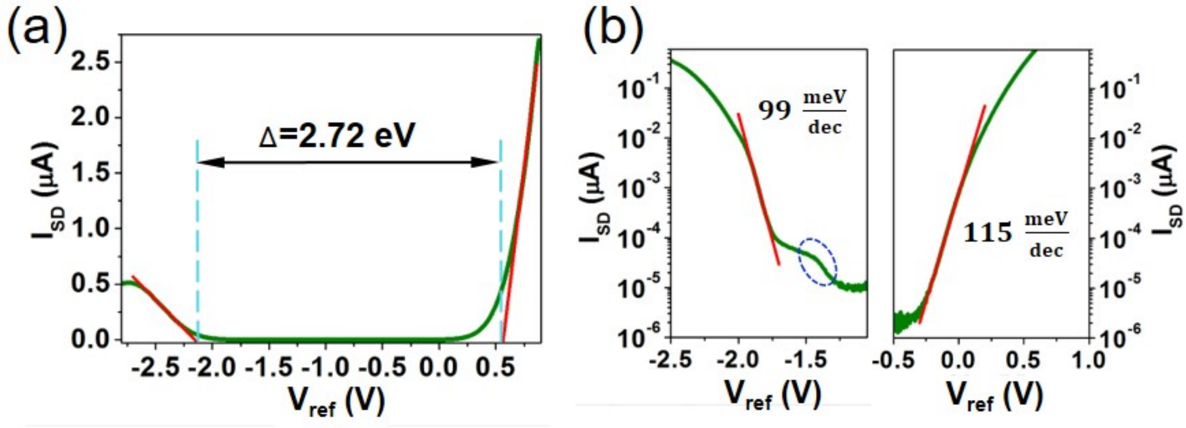

Figure 4.3: Estimation of the band gap of CVD grown monolayer MoS_2 from the transfer curves of an ionic-liquid gated transistor. (a) Source-drain current I_{SD} as a function of reference voltage V_{ref}, measured for $V_{SD} = 0.5$ V. The red lines are an extrapolation of the linear regime to $I_{SD} = 0$ V, as needed to extract the threshold voltage (whose position for holes and electrons is indicated by the vertical blue-dashed lines). The difference between the threshold voltage of holes and electrons provides an estimate of the band gap ($\Delta = 2.7$ eV in the present case). (b) Semi logarithmic plots of the data shown in (a). The red lines are the linear regressions made to estimate the sub-threshold swing. The dashed ellipse emphasizes the presence of an anomalously large contribution to the source drain current very deep in the hole subthreshold regime, due to in-gap states at energies close to the top of the valence band.

We use the data of figure 4.3a to estimate the value of the band gap Δ of CVD-grown MoS_2 monolayers. To this end, we extract the values of the threshold voltages for electron V_{th}^{e} and hole V_{th}^{h} conduction from figure 4.3a, from which we obtain $\Delta = e(V_{th}^{e}-V_{th}^{h})$. Recent work on IL-gated transistors realized on WS_2 bulk[76], mono/bilayers[77], and bulk $MoTe_2$[79,116] has shown that this estimate is reliable to approximately 10% – or better – even when imperfections are present in the devices, mainly thanks to the extremely large geometrical capacitance of the IL gate. In $MoTe_2$ bulk devices, for instance, $\Delta = e(V_{th}^{e}-V_{th}^{h})$ was found to agree with scanning tunnelling data and optical spectroscopy data, even in the presence of significant unintentional doping and of sizeable hysteresis in the device transfer curve[79]. Similarly to the case of bulk $MoTe_2$ devices, in our CVD-grown MoS_2 FETs the subthreshold swing for holes and electrons measured at T= 240 K is respectively 99 and 115 meV/dec (see figure 4.3b). These values, approximately twice larger than the ultimate limit S=kT/e ln(10)=47 meV/dec, are indicative of contact non-ideality or of the presence of trap states inside the band gap. Indeed, in-gap states near the top of the valence band are visible in the left panel of figure 4.3b, where they manifest themselves in the enhancement of I_{SD} measured deep in the hole subthreshold region (put in evidence by the dashed ellipse). Nevertheless, just as in the case of $MoTe_2$, it still makes sense to estimate the band gap from the device transfer curve. Depending on the specific device on which the analysis is done, we find band gap values $\Delta = e(V^e_{th}$-$V^h_{th})$ ranging from 2.4 to 2.7 eV. When compared to existing estimates reported in the literature (2.15-2.5 eV, as obtained from scanning tunnelling spectroscopy[117,118] and frequency-dependent photocurrent measurements[119]), our measurements contribute to constrain the true value of the band gap of MoS_2 monolayers. In this regard we emphasize that, when extracting the gap from the ambipolar FET transfer curves, it easy to understand how different physical processes lead to an overestimation of the value of Δ, but not to an underestimation. Our experiments therefore strongly suggest that the actual value of Δ has to be 2.4 eV or smaller.

4.4 Light-emitting transistor

Having established the occurrence of ambipolar conduction in IL-gated CVD-grown MoS_2 transistors, we go back to the ambipolar injection regime and search for electroluminescence. Figure 4.4a shows the output curve of one of our transistors measured at $V_G = 0.5$ V, in which V_{SD} is swept well past the onset of ambipolar injection (starting at $V_{SD} \sim 3$ V). To detect light emission, we image the device under the microscope using a CCD camera. Images taken when the device is biased at increasingly larger V_{SD} values are shown on the right side of figure 4.4a. For $V_{SD} < 4$ V, no emitted light is detected within the experimental sensitivity. For larger V_{SD}, electroluminescence from spots localized near hole-injecting contact becomes visible. If V_{SD} is increased further, the light intensity emitted from these spots, as well as their number, increases. Light emission, however, continues to occur only near the interface with the hole-injecting contact.

The observed behavior is different from the one expected for ideal operation of light-emitting transistors[120], in which case the location where light is emitted from shifts in the channel upon varying V_{SD}. To ensure that emission does indeed occur from exciton recombination in the MoS_2 monolayer, and not from uncontrolled processes associated to carrier injection from the metal, it is therefore important to measure the electroluminescence energy spectrum. This is shown in figure 4.4b (red curve) together with the PL spectrum measured on the same devices, away from the contact region (blue curve; as discussed above – see figure 4.1d – the large sharp line at 690 nm and the smaller features just above 700 nm originate from PL of the sapphire substrate). The dominant peak in the electroluminescence spectrum coincides with the one in the PL spectrum, confirming that the light emitted from the bright spots indeed originates from exciton recombination in the MoS_2 monolayers. The electroluminescence spectrum shows an additional smaller and broader peak at approximately 770 nm (1.6 eV), whose origin is discussed in detail below (in the PL spectrum acquired at room temperature this peak is absent but it appears after cooling the sample to T = 77 K; see section 4.6.2 figure 4.6) and in *Chapter 5.*

At a first glance, the behavior of the observed electroluminescence appears similar to the phenomenology that has been reported previously[91] in devices realized using exfoliated monolayer MoS_2. A more careful inspection of the data, however, shows that important differences are present in the two cases, in particular in the evolution of EL spectrum upon increasing the applied bias. As we discuss below, the possibility to compare the gate-dependent ambipolar transport data with the bias dependent EL measurements in our devices provides strong evidence for a simple physical scenario that explains virtually all our observations. This scenario enables us to draw consistent conclusions about some aspects of the properties of CVD-grown MoS_2 monolayers, most notably of the in-gap states present at energies just above the top of the valence band.

To understand the behavior of the EL observed in our devices, it is important to realize that under the ambipolar injection conditions leading to light emission, transport occurs in the so-called space charge limited regime[121,122] for both electrons and holes. In this regime the charge carriers responsible for the current flow are not accumulated by the applied gate voltage, but are injected from the contacts (electrons at one contact and holes at the other), due to the large applied bias. As it is well established, the space charge limited transport regime is extremely sensitive to defects acting as trap for charge carriers, whose presence determines the profile of the electrostatic potential inside the material, and therefore the spatial distribution of the injected charge. In particular, a large density of 'deep traps' – *i.e.,* traps having an energy many times larger than kT– can result in the spatial localization of carriers close to the injecting contact at low bias, and charge can penetrate deeper into the material only when a sufficiently high bias is applied (if the density of deep traps is large, the bias required to induce complete detrapping may be too high to be reached

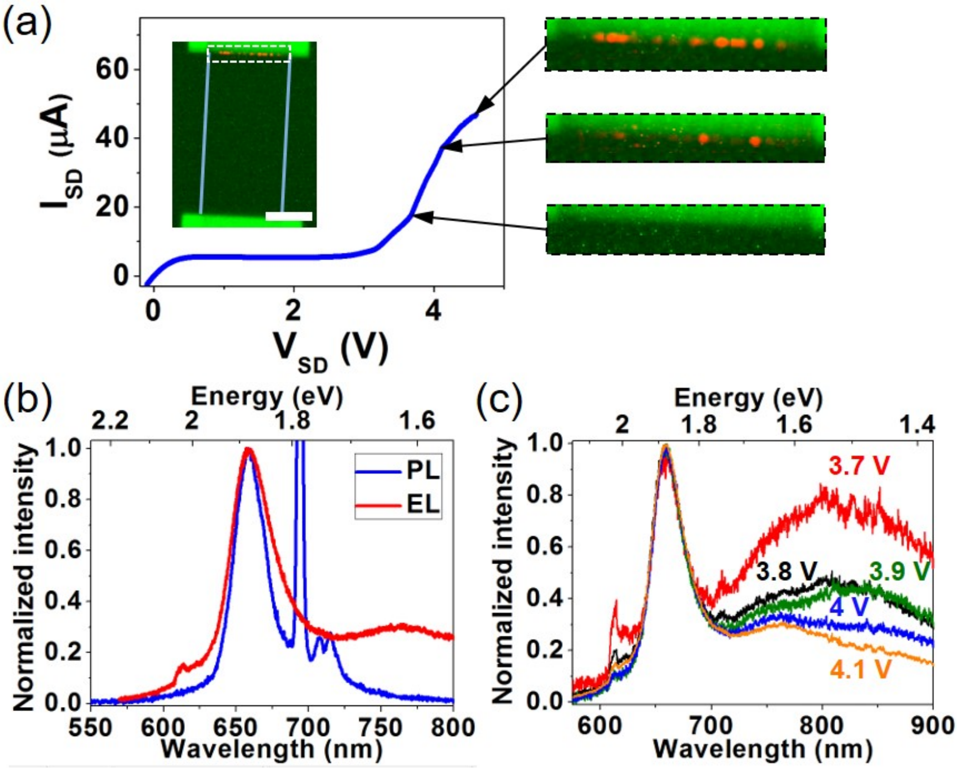

Figure 4.4: Electroluminescence in a CVD-grown MoS_2 monolayer ionic-liquid FET. (a) Source-drain current I_{SD} as a function of source-drain bias extending to large V_{SD} values, as it is needed to drive the device into the light-emission regime. The inset shows an image of the device with the region of the channel close to the hole injecting contact – where light emission occurs – delimited by a white dashed line. The three panels on the right show images of this region for three different values of bias (pointed to by the black arrows). Light emitting spots (red spots in the image) appear upon increasing V_{SD}. The scale bar in the inset corresponds to 20μm. (b) Comparison between the photoluminescence (blue curve) and electroluminescence (red curve) spectra (V_{SD} = 4.1 V) measured in the same device, showing that the electroluminescence peaks at the energy expected from the recombination of A excitons in MoS_2 (the intensities of both curves are normalized to the A-exciton peak). A smaller and broader peak is seen in the EL spectrum originating from trapped excitons; in PL the same peak is observed but only at lower temperature (see Supplementary Information). (c) Normalized electroluminescence spectra recorded for different values of source-drain bias V_{SD} demonstrating the decrease of the lower energy peak with upon increasing bias, consistently with what is expected for trapped excitons.

in the experiments without causing device failure)[121–123]. These considerations are relevant here because, as mentioned earlier, the measurement of I_{SD} as a function of V_{ref} (Figure 4.3a) shows that a large density of states is present in the gap at an energy approximately 250-300 meV above the top of the valence band. At room temperature, these states act as traps for holes with a trapping energy of 10·kT or larger (*i.e.*, they are deep traps), and cause the space charge due to the injected holes to remain localized close to the injecting contact. This explains why the position where electroluminescence originates from does not shift significantly upon increasing

V_{SD}. The exact origin of these trap states is discussed in *Chapter 5.*

In the spectrum of the measured EL, the effect of trapping manifests itself in the shallow peak seen at energies below the peak at 660 nm originating from the recombination of 'free' excitons, as usually observed in MoS_2 (see the red line in figure 4.4b). Indeed, the broad peak is 250-300 meV lower in energy than the free exciton peak, and this difference corresponds quite precisely to the energy of the trap states determined by the analysis of I_{SD} – vs – V_{ref} shown in figure 4.3a (in simple terms, the broad low-energy peak is due to excitons formed by an electron and a trapped hole that emits a photon of lower energy when recombining). The dependence of the amplitude of broad peak on V_{SD} – shown in figure 4.4c – is consistent with the trapping scenario that we have outlined: as the applied bias increases, the amplitude of the shallow peak decreases relatively to the main 'free' exciton peak because a larger V_{SD} tends both to fill trap states and to de-trap holes, thereby increasing the number of free excitons relative to that of trapped ones. Interestingly, the trend shown in figure 4.4c leads to a sharpening of the spectrum upon increasing V_{SD}. This behavior is qualitatively the opposite of what has been observed by Sundaram et al.[91] in the EL of exfoliated MoS_2 monolayers, where the spectrum of the emitted light broadened very significantly in energy upon increasing V_{SD}. The large bias-induced broadening was attributed to hot photoluminescence, a conclusion that certainly appears plausible in those devices, because the power-per-unit-surface injected under the biasing conditions needed to observe EL was approximately 10^4 times larger than in our experiments. These considerations illustrate how electroluminescence in MoS_2 monolayers can exhibit different behavior depending on the transport regime. It is only through the careful combined analysis of detailed aspects of the transport and opto-electronic processes – which in our devices is made possible by the use of an ionic liquid gate – that a consistent microscopic picture of the properties of MoS_2 monolayers can be established.

4.5 Conclusion

In conclusion, we have demonstrated the possibility to realize ionic-liquid gate field-effect transistors on large-area MoS_2 monolayers grown by chemical vapor deposition. Characterization of the material uniformity, of the transistor electrical characteristics, as well as the observation of electroluminescence show that the properties of devices realized on CVD-grown monolayers are as good as those of existing devices based on exfoliated material, and in several regards better. The observation of clear ambipolar conduction in the transfer curves of FETs, which had not been previously reported for exfoliated MoS_2 monolayers, allows us to extract specific information about the electronic properties of the material, including the size of the band gap and the identification of the in-gap states acting as trap for holes. Thanks to this information we have established a clear physical scenario that accounts in a consistent way for the results of transport and electroluminescence measurements. Finally, these results have technological relevance because the use of semiconducting monolayers transition metal dichalcogenides in future opto-electronic applications will necessarily rely on devices fabricated on large-area material produced by a controllable and scalable technique.

4.6 Appendix

4.6.1 Hall effect measurements

As part of the electrical characterization of our CVD-grown MoS_2 monolayers, we have measured the electron mobility using ionic liquid gated field-effect transistors realized as discussed in the main text, comprising multiple contacts disposed in a Hall bar configuration. An optical micrograph of one of such devices is shown in the inset of figure 4.5a. The Hall bar configuration allows us to measure the Hall effect that develops upon the application of a perpendicular magnetic field (see figure 4.5a; V_{SD} = 0.25 V, I_{SD} = 10 μA, V_G-V_{th} = 0.75 V). From the measured Hall resistance we extract the density of accumulated electrons and from the longitudinal resistance the carrier mobility, which are plotted in figure 4.5b as a function of V_G-V_{th} (red up triangles and blue squares, respectively; T=250 K).

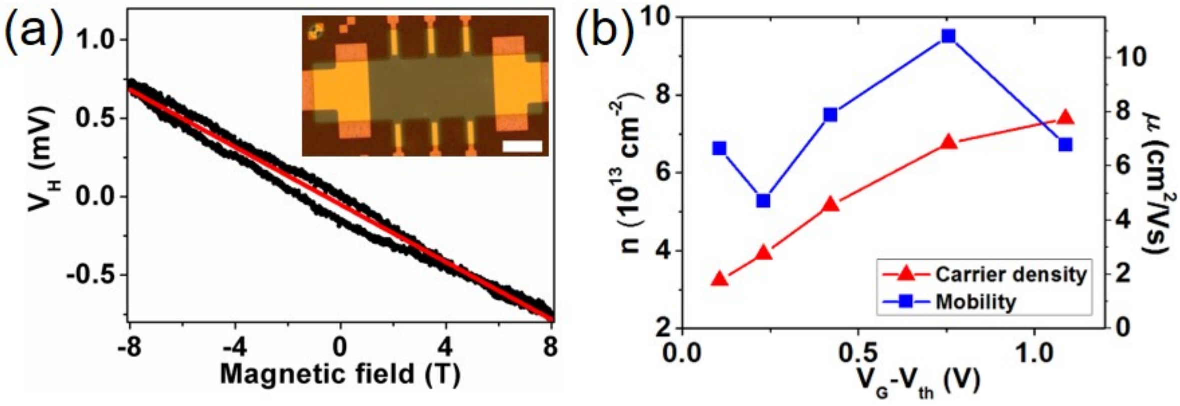

Figure 4.5: Hall effect in MoS_2 monolayer ionic liquid gated FETs. (a) Hall voltage V_H as a function of magnetic field B measured at V_G-V_{th} = 0.75 V and T = 250 K. The red line is a linear fit to the data. (Inset) optical microscope image of a multi terminal Hall bar device. The device geometry is defined by a window made in a PMMA layer, which determines the region where the ionic liquid is in contact with MoS_2 . The scale bar corresponds to 25 μm. (b) Electron density and mobility extracted from the measurement of the Hall and longitudinal resistance for different gate biases at T = 250 K.

4.6.2 Evidence for trap state in photoluminescence measurements

In the main text we have shown clear evidence for the presence of in-gap states close to the top of the valence band, acting as traps for holes. These states manifest themselves in the I_{SD}-vs-V_{ref} curve, in the electroluminescence spectrum and in the bias dependence of this quantity. Somewhat surprisingly, however, these hole trap states are not visible in the photoluminescence spectrum shown in the main text, measured at room temperature (where they should manifest themselves as a broad peak at energy lower than the main emission line). Figure 4.6 shows that, after cooling down the sample to 77 K, a broad peak at lower energy is indeed present, providing clear evidence for the presence of hole trap state also in PL measurements. The data shown in figure 4.6, therefore, confirm the internal consistency of our measurements and of their interpretation (why – contrary to the case of electroluminescence – the peak in PL is only visible at low temperature is currently unclear. Possibly, the difference between EL and PL originates from the way in which excitons are generated in EL and PL measurements: in the first case, electrical injection generates low-energy electrons and holes, whereas in the second case photo-generation generates high-energy carriers and excitons are formed after energy relaxation has occurred).

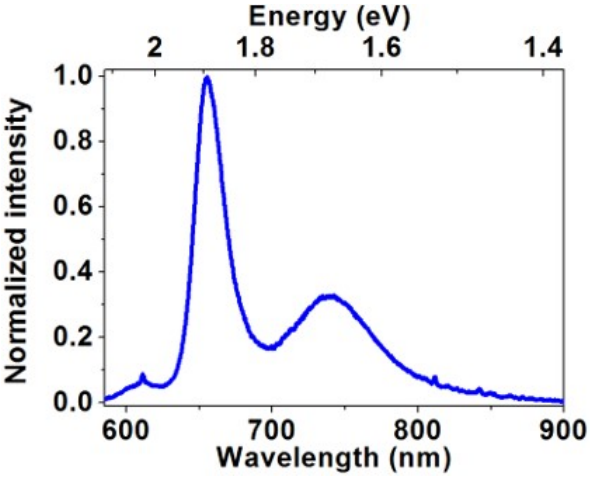

Figure 4.6: Photoluminescence spectrum of CVD-grown monolayer measured at T = 77 K.

Chapter 5: Hole transport in exfoliated monolayer MoS_2

5.1 Introduction

Extensive studies of monolayers (MLs) of group VI semiconducting transition metal dichalcogenides (TMDCs) have demonstrated that all these materials share many electronic properties. For example, they all have a direct band gap at the K and K‘ points,[38,110,124] a finite Berry curvature in the K and K‘ valley[42–45,125] responsible for the occurrence of the valley Hall effect[45,46], an extremely strong spin-orbit coupling (as large as a few hundreds meV in the valence band),[36,39,40] very large exciton binding energies due to the reduced screening characteristic of 2D systems,[20,126,127] stable trion excitations[47,48], and more. Differences are also present, such as the relative sign of the spin orientation at the conduction band minimum (CBM) and valence band maximum (VBM) – the same for Mo-based compounds and opposite for W-based ones – that leads to a different temperature dependence of the measured photoluminescence.[52,53] Although important for specific physical phenomena, these differences mostly concern more subtle aspects of the electronic properties.

Having access to a broad class of semiconducting 2D materials with many similar properties is very attractive because – for instance – it facilitates the realization of van der Waals heterostructures obtained by stacking two or more monolayers of different TMDCs on top of each other. It should be realized, however, that these considerations do not take into account that real materials unavoidably contain defects that are specific to each individual compound, and that drastically affect their electronic response. This is certainly the case for the systems considered here, since in semiconductors defects generally determine crucial characteristics such as the work function,[128] the position of electrochemical potential,[129,130] the transport properties (*e.g.*, the carrier mobility[55,57]), the rate of non-

---

The results presented in this chapter have been published as Evgeniy Ponomarev, Árpád Pásztor, Adrien Waelchli, Alessandro Scarfato, Nicolas Ubrig, Christoph Renner, and Alberto F. Morpurgo, *ACS Nano, **2018**, 12* (3). The STM measurements were done in collaboration with the group of Prof. Christoph Renner by Árpád Pásztor and Adrien Waelchli.

radiative electron-hole recombination,[131] *etc.* That is why an increasing research effort is currently being devoted to the investigation of defects present in all types of semiconducting 2D materials, whose identification, understanding and control will be necessary if these systems will eventually be employed in technological applications (not to mention the possibility to exploit new functionalities that are sometimes offered by defects in 2D materials, such as – for instance – their ability to act as single photon emitters[132–137]).

One important aspect that is seemingly common to semiconducting TMDC monolayers is their ability to support well-balanced ambipolar transport. Measurements done on suitable field-effect transistor (FET) devices upon sweeping the gate voltage show that an equally good conductivity is found in a same monolayer irrespective of whether the chemical potential is in the conduction or in the valence band. This feature is particularly relevant for the realization of opto-electronic devices, since it is the ability to transport simultaneously electrons and holes that allows the controlled generation of electroluminescence from electron-hole recombination or the conversion of light into an electrical signal. Surprisingly, however, if we look at experiments reported on exfoliated monolayers of common group VI semiconducting TMDCs, well-balanced ambipolar transport has been observed in $MoSe_2$,[138] WSe_2,[139] and WS_2,[77] but not in MoS_2. This is unexpected both because exfoliated MoS_2 monolayers are probably the most studied among these compounds (which is why they are often used to benchmark other 2D semiconductors) and because for thick exfoliated MoS_2 multilayers excellent ambipolar conduction is routinely observed.[109,140]

Motivated by these considerations, here we investigate ambipolar conduction in exfoliated MoS_2 monolayers using ionic liquid-gated FETs and demonstrate a systematic and reproducible anomalous behavior of transport upon hole accumulation. Specifically, after the onset of hole conduction a virtually complete suppression of source-drain current is observed in all devices as the gate voltage is biased to shift the chemical potential deeper into the valence band. In contrast, experiments on identical devices realized on exfoliated bi, tri, and tetralayer MoS_2 show excellent ambipolar conduction, demonstrating that the anomalous hole transport is an inherent characteristic of monolayer MoS_2 devices. By combining transistor measurements, gate-dependent optical studies (photo-luminescence and Raman spectroscopy), scanning tunneling imaging and spectroscopy, and a thorough analysis of existing studies based on *ab-initio* calculations, we establish the origin of this phenomenon as due to the presence of atomic-scale defects that induce states inside the band-gap of MoS_2 monolayers, approximately 300-400 meV above the top of the valence band. These defects – whose manifestations are consistent with what is expected from sulfur vacancies[56,141] – act as traps for holes and prevent hole conduction in exfoliated MoS_2 monolayers. The phenomenon is specific to MoS_2 monolayers – and not to monolayers of other semiconducting TMDCs or to MoS_2 bilayers/thicker multilayers – because only in MoS_2 monolayers the states created by chalcogen vacancies near the top of the valence band appear to be inside the band gap.

5.2 Anomalous hole transport in exfoliated monolayer MoS_2

The most effective way to investigate ambipolar transport in TMDC monolayers is by integrating them into a FET employing an ionic liquid top gate, as illustrated schematically in figure 5.1a. The very large capacitance of the ionic gate allows the electrochemical potential to be shifted over a large range – from deep in the conduction band to deep in the valence band – as demonstrated experimentally by the ambipolar conduction observed in WS_2[77], WSe_2[139] and $MoSe_2$[138,142] monolayers. For FETs using exfoliated monolayers of MoS_2, however, a similar observation has not been reported, and our measurements show that an unexpected behavior indeed occurs when the gate is biased to shift the electrochemical potential into the valence band. Specifically, figure 5.1b shows transfer curves (source-drain current I_{SD} as a function of gate voltage V_G at a finite applied source-drain bias V_{SD}) measured on two of our devices representative of the behavior of eight nominally identical devices that we investigated. Upon increasing V_G above the electron threshold voltage (V_{th}^e) carriers are accumulated in the conduction band and the source-drain current increases steeply (the estimated value of electron density n_e at the largest V_G value reached approximately $n_e = C_*(V_G - V_{th}^e)/e = 7 \cdot 10^{12}$ cm^{-2} where $C_* = 7\mu F cm^{-2}$ is the capacitance per unit of the ionic liquid[76,77]; values as large as $n_e = 2 - 3 \cdot 10^{14}$ cm^{-2} can be obtained at larger positive V_G values[143]). This is the behavior that is commonly expected in a field-effect transistor.

As V_G is swept past the onset of hole transport, however, we observe that after an initial increase, I_{SD} exhibits a maximum followed by a steep drop to a virtually vanishing current, with the conductivity $\sigma_\square$ dropping by approximately two orders of magnitude (see the inset in figure 5.1b). De-

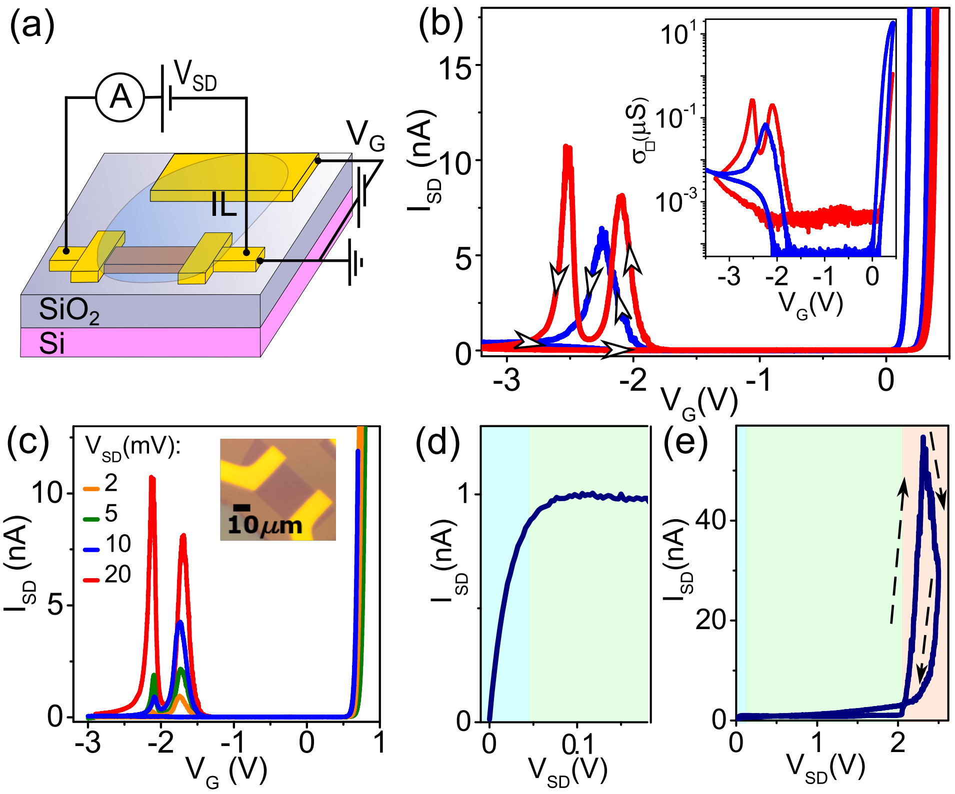

Figure 5.1: Anomalous hole transport in FETs based on exfoliated monolayer MoS$_2$. (a) Schematics of an ionic-liquid gated FET based on monolayer MoS$_2$. (b) Representative FET transfer curves (*i.e.*, I$_{SD}$ versus V$_G$ at fixed V$_{SD}$) showing electron transport for V$_G$ $>$ 0.3V and an anomalous transport behavior upon hole accumulation: for V$_G$ $<$ -1.9V, after an initial increase, the source-drain current decreases to vanishingly small values if V$_G$ is swept to larger negative values. Depending on the device either one (blue curve, V$_{SD}$ = 100mV) or two (red curve, V$_{SD}$ = 20mV) peaks in I$_{SD}$ are seen upon hole accumulation. In all cases, as V$_G$ is swept back from large negative values, I$_{SD}$ remains low (the arrows indicate how V$_G$ is swept). (Inset) Same data shown in panel (b) plotted in terms of conductivity $\sigma_\square$. (c) I$_{SD}$-vs-V$_G$ measured for different values of V$_{SD}$: the measurements, done in sequence, show that the current suppression at large negative V$_G$ does not originate from a permanent device degradation (the inset shows an optical microscope image of a device). In (b) and (c) the relative V$_G$-shift visible in the transfer curves originates from bias stress caused by prolonged measurements done on this specific device. (d,e) Source-drain current I$_{SD}$ as a function of source-drain bias V$_{SD}$. Panel (d) focuses on the linear and saturation regimes (respectively shaded in light blue and light green). Panel (e) shows a much larger V$_{SD}$ range; the large increase in current for V$_{SD}$ $>$ 2V is due to the ambipolar injection regime (light orange shaded region) in which electrons and holes are injected at opposite contacts. The abrupt decrease in I$_{SD}$, occurring just after the onset of hole accumulation, is a manifestation of the same effect seen in panel (b).

pending on the specific device either one or two peaks in I$_{SD}$ are observed, as shown by the red and blue curves in figure 5.1b. With any further increase of gate voltage to more negative values I_{SD} stays low, and remains low as the gate voltage is swept back to V_G = 0V. The phenomenon is reversible upon re-cycling V_G from zero to large negative values and back, implying that the observed behavior is not due to a permanent degradation of the device. This can be concluded from figure 5.1c, which shows transfer curves acquired successively one after the other, by sweeping V_G, for increasingly large V_{SD} values. The phenomenon was observed in FET devices with source and drain contacts made of two different materials (Au and Pt), indicating that the current suppression – and the corresponding anomalous behavior of transport upon hole accumulation – is not due to a contact effect.

The anomalous behavior of hole conduction in MoS_2 monolayers is also clearly visible in the FET output characteristics, *i.e.*, when measuring the source-drain current I_{SD} as a function of source-drain bias V_{SD} at a fixed gate voltage V_G. At low positive V_{SD} values, with the gate biased to have electron accumulation, the usual transistor behavior is observed, with I_{SD} increasing linearly until the onset of the saturation regime, occurring at $V_{SD} \simeq V_G$-V^e_{th}, past which I_{SD} stays constant (figure 5.1d). As V_{SD} is increased up to much higher values, I_{SD} starts to grow again rapidly (figure 5.1e), because the applied source-drain bias causes the channel potential to reverse its polarity and to exceed the threshold for hole accumulation near the drain contact. This is the so-called ambipolar injection regime in which the steep increase in I_{SD} is due to holes injected from the drain contact. In the experiment we see that, sweeping V_{SD} past the point when I_{SD} starts to increase (orange shaded area in figure 5.1e) causes a rapid drop of current, and the current stays low as V_{SD} is swept back. We conclude that, irrespectively of the way in which holes are accumulated in the MoS_2 monolayer channel – either by sweeping the gate voltage or the source-drain bias – an unexpected anomalous suppression of I_{SD} is observed in all cases.

The observed phenomenon is inherent to monolayers, and is absent in ionic liquid gated FETs realized with MoS_2 bilayers or thicker multilayers. Figure 5.2 shows the transfer curves of devices fabricated on bi, tri, and tetra layer MoS_2, in which the measured I_{SD} is excellently balanced (*i.e.*, the magnitude of the measured current is approximately the same upon electron and hole accumulation), with no indication of any anomalous behavior. These observations explain why earlier experiments on ionic liquid gated FETs realized using thick (essentially bulk-like) exfoliated MoS_2 crystals[109,140] have reported high-quality ambipolar transport, despite the absence of hole current in monolayers.

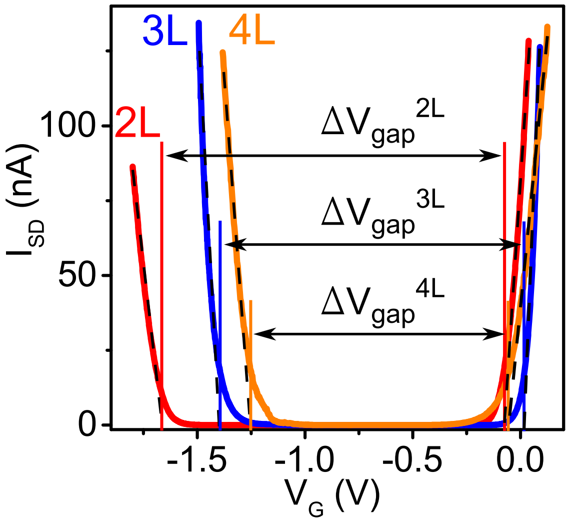

Figure 5.2: Ambipolar transport in MoS_2 multilayers. Source-drain current I_{SD} as a function of gate voltage V_G for FETs fabricated on MoS_2 multilayers, containing respectively two, three, and four monolayers. Well balanced ambipolar transport is seen in all cases. The black dashed lines are the extrapolation of I_{SD} to 0 nA, as required to extract the values of threshold voltage (the thresholds for hole and electron conductions in the layers of different thicknesses are indicated by the vertical solid lines of the corresponding colors). The band gap is obtained from E_{gap} = e (V_{th}^{e} - V_{th}^{h}).

Note that, as the thickness of the MoS_2 layer is increased, the range of gate voltages in which the current vanishes (*i.e.*, in which the electrochemical potential is located inside the band gap) decreases. This is because ionic liquid gating used on systems with a small density of states, such as in the gap of a semiconductor, has spectroscopic capabilities[76,77,79] and the difference in V_G between the threshold voltage for electron and hole conduction is a direct measure of the band gap (to increase the precision with which the gap is determined, data should be plotted as a function of a reference potential – which avoids effects caused by a possible voltage drop at the gate-liquid interface – but in high quality devices the reference potential and the gate voltage nearly coincide). We conclude from these measurements that the band gap is ΔV_{gap}^{2L} = 1.6 eV for MoS_2 bilayers, ΔV_{gap}^{3L} = 1.4 eV for trilayers, and ΔV_{gap}^{4L} = 1.25 eV for tetralayers, in all cases with a precision of approximately 10%. Importantly, since the threshold voltage determines the energy of accumulation of individual charge carriers in the respective band, the values extracted are the actual band gaps of the different multilayers – as measured for instance from scanning tunneling spectroscopy[118]– and not the exciton energies which are commonly measured in optical experiments. Irrespective of these considerations, we re-iterate that these experiments unambiguously show that the suppression of conductivity under hole accumulation is a distinct property of exfoliated MoS_2 monolayers.

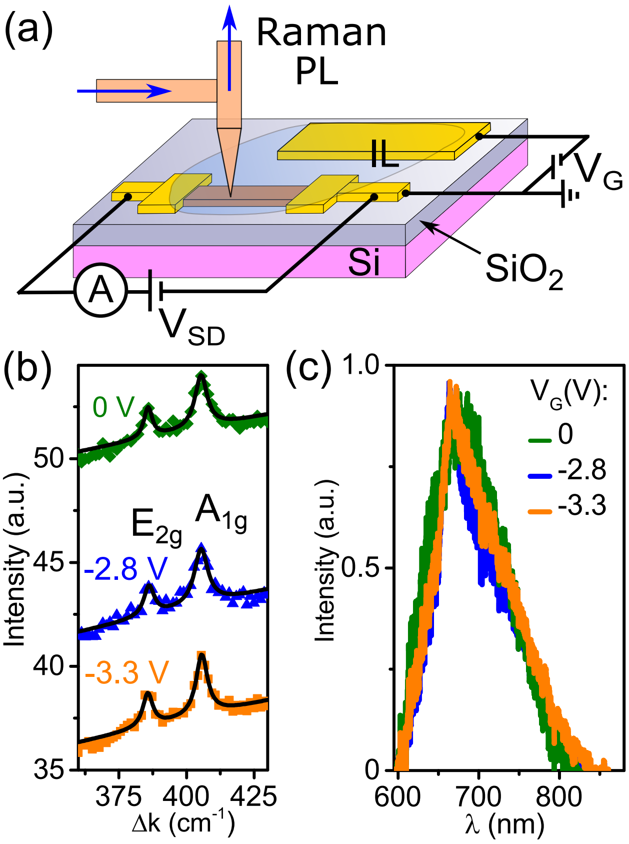

Figure 5.3: *In-situ* optical characterization of an ionic liquid-gated MoS_2 monolayer FET. (a) Measurement scheme to perform gate dependent photoluminescence and Raman spectroscopy on a MoS_2 monolayer. (b) Raman spectra showing the characteristic vibrational modes of MoS_2 monolayers (E_{2g} and A_{1g}) for different V_G values. No significant changes in position or line-width of these modes is seen upon applying a large negative gate voltage, corresponding to values for which holes are accumulated in the channel. (c) Photoluminescence spectra for different values of V_G showing that the A-exciton peak of MoS_2 monolayer remains unchanged.

The systematic anomalous hole transport behavior observed in MoS_2 monolayer devices is unexpected and an explanation is called for. In view of the very large negative gate voltage required to populate the valence band, one may wonder whether the correspondingly large electric field (estimated by dividing the maximum applied gate voltage by the thickness of the ionic liquid double layer, and reaching up to several tens of MV/cm) can actually affect the crystalline structure of the material. Indeed, such a drastic structural effect has been reported previously for $MoTe_2$[144,145], and its occurrence in monolayer MoS_2 cannot be excluded a priori. To address this question we performed Raman and photoluminescence spectroscopy of ionic-liquid gated MoS_2 monolayers *in-situ* , in the presence of a large negative gate voltage (see schematics in figure 5.3a). Selected

Raman spectra collected at different V_G values, from 0 V up to -3.3 V (see figure 5.3b), show no change in the characteristic E_{2g} and A_{1g} modes of 2H MoS_2 throughout the V_G range investigated (the same is true for other parts of the spectrum that we looked at). Results from photoluminescence (PL) spectroscopy are shown in figure 5.3c, with a clear peak centered at about 670nm that originates from the A-exciton recombination in MoS_2 and represents a characteristic signature of MoS_2 monolayers. Remarkably, the peak (broadened by large potential fluctuations generated by the ionic liquid gate) remains unchanged, irrespective of the applied gate voltage. The observed insensitivity of Raman and PL measurements to the gate voltage indicates the absence of significant structural changes in the MoS_2 monolayers, and allows us to exclude that the reentrance of the insulating state observed at large negative V_G has a structural origin.

5.3 In-gap trap states in MoS$_2$ monolayer

What makes the suppression of hole current in exfoliated MoS_2 monolayers even more surprising is that FETs realized on large-area monolayers grown by chemical vapor deposition (CVD) do exhibit good ambipolar characteristics.[80] The top panel of figure 5.4 shows the conductivity ($\sigma_\square$) of a device realized on such a CVD monolayer (blue curve) that, in contrast to what is measured on a device realized using an exfoliated monolayer (green curve), exhibits rather conventional ambipolar conduction. From the data, we first extract the threshold voltage for electrons (which coincides for CVD-grown and exfoliated monolayers) and holes (which can only be determined for the device realized on the CVD-grown monolayer); then we compare transport in the electron and hole subthreshold regimes by looking at the source-drain current I_{SD} on a logarithmic scale (Figure 4, bottom panel). In the electron sub-threshold regime (light-blue shaded region in figure 5.4) the conductivity is higher and the subthreshold slope is less steep for the device realized on the CVD-grown monolayer. This behavior is due to a broader tail of disorder-induced localized states that in CVD-grown monolayers is present inside the band gap near the bottom of the conduction band. It is expected, because CVD-grown monolayers are generally more disordered than exfoliated ones, due to a larger density of grain boundaries.

A very different behavior is observed in the hole subthreshold regime (light yellow shaded region in figure 5.4): the current enhancement extends much more deeply into the gap and it is much larger (by nearly two orders of magnitude) for exfoliated monolayers as compared to CVD-grown material. Furthermore, the very pronounced broad peaks seen in the source-drain current measured on exfoliated monolayers – also present at comparable energy in CVD-grown material, albeit much less pronouncedly – seem to indicate the presence of discrete energy states. These observations indicate that the nature of disorder affecting states near the top of the valence band is qualitatively different from that influencing states near the bottom of the conduction band. Specifically, finding that the effect of disorder near the top of the valence band is much stronger in exfoliated MoS_2 monolayers despite their superior structural quality indicates that the origin of the effect is not due to the presence of grain boundaries, but rather to other kind of defects. These observations also strongly suggest that disorder at energies near the top of the valence band has the same origin in exfoliated and CVD-grown monolayers, since the sub-gap states are present in the same range of energies in the two cases.

5.4 Origin of the anomalous hole transport

To investigate the nature of the discrete in-gap energy states near the top of the valence band we employ scanning tunneling microscopy (STM) and scanning tunneling spectroscopy (STS). These techniques provide detailed information on the local crystalline and electronic structure of a material down to the atomic scale. STM measurements were performed on a CVD-grown monolayer deposited on a dielectric substrate (SiO_2/Si), made conductive by electrostatic accumulation of charge carriers (*i.e.*, by integrating it into a FET device; the set-up scheme and FET transfer characteristics are shown in figure 5.5a and 5.5b respectively). Under these conditions, with a large positive gate voltage applied to the Si back gate, we can successfully establish stable tunneling conditions, as it is needed to take hiqh-quality images and perform tunneling spectroscopy. Figure 5.5c demonstrates that atomic resolution can indeed be achieved through the observation of the triangular atomic lattice of MoS_2. Atomic resolution is further highlighted by the intense six-fold symmetric peak structure in the image Fourier-transform. These results illustrate how STM measurements performed under an applied gate voltage allow the local properties of the material to be investigated.

We probe the spatial distribution of the local density of states (LDOS) by acquiring STS spectra over a dense grid. A map obtained in this way is presented in figure 5.5d, where we plot the differential tunneling conduc-

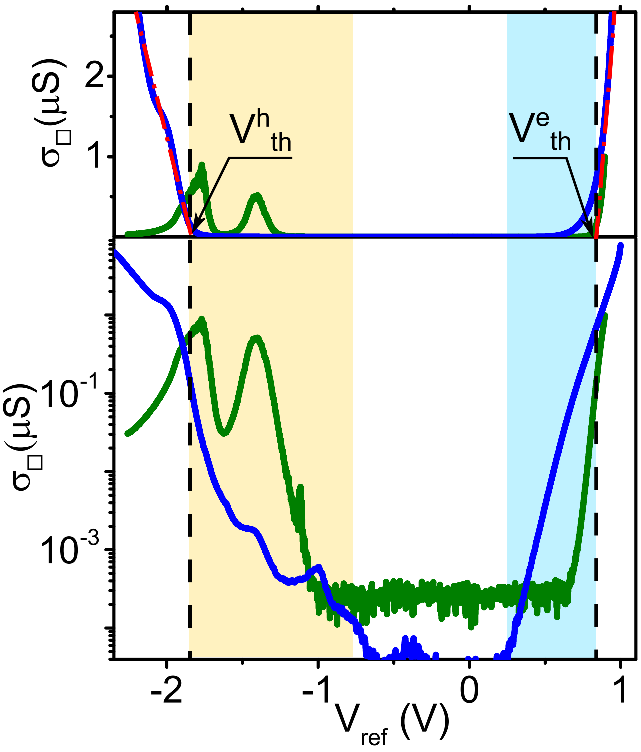

Figure 5.4: Comparison of ambipolar transport in FETs based on CVD-grown and exfoliated MoS_2 monolayers. Top panel: Conductivity $\sigma_\square$ as a function of reference voltage V_{ref} for CVD-grown (blue curve) and exfoliated (green curve) MoS_2 monolayer devices. The red dashed-dotted lines are an extrapolation of the conductivity $\sigma_\square$ measured in the linear regime to 0 S, from which we determine the threshold voltages for electrons and holes. Bottom panel: Semilogarithmic plots of the data shown in the top panel. The subthreshold regimes for electrons and holes correspond to the light blue and the light yellow shaded areas. The higher conductivity of CVD-grown monolayer FET in the electron subthreshold regime originates from the larger density of structural defects present. In the hole subthreshold region the exfoliated monolayer FET exhibits conductivity almost two orders of magnitude higher than the CVD-grown one, as well as a very different qualitative behavior of transport as compared to electrons (subthreshold electron transport is featureless, whereas for holes distinct peaks in conductivity are seen). These observations are indicative of the very different nature of disorder affecting electron and hole transport in the respective subthreshold regimes.

tance dI/dV measured at a fixed dc bias (V_{tip} = -1.5 V). Three regions can be identified. The first region occupies the majority of the scanned area and is composed of semiconducting spectra (such as spectrum 1, on the left side of the figure) with a band gap value of 2.1 eV, or just slightly larger (which is why the differential conductance measured at V_{tip} = -1.5 V vanishes). This value of the gap confirms that the material studied is indeed a monolayer. In the two other regions – delimited by the green (region 2) and red (region 3) dashed lines – additional states are visible, and manifest themselves as an enhanced tunneling conductance inside the gap of monolayer MoS_2. Interestingly, in both cases the image shows that

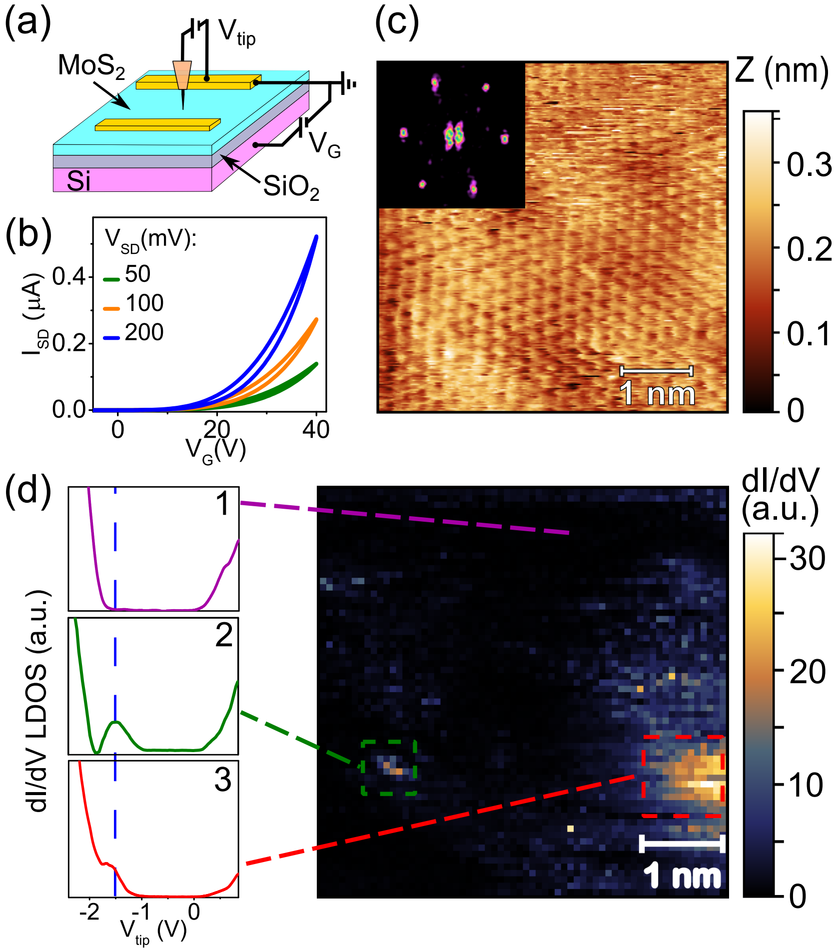

Figure 5.5: Atomic-scale study of monolayer MoS_2. (a) Schematic representation of the configuration used to perform STM/STS measurements on a CVD-grown MoS_2 monolayer. The monolayer is grown on a doped Si substrate acting as a gate covered by a thermally grown SiO_2 285 nm thick layer. STM/STS measurements are done with a positive applied gate voltage that makes the MoS_2 monolayer conductive (see the transfer curves shown in (b), measured on the same structure used for STM/STS experiments) (c) Atomic resolution STM image (V_{tip} = 1V, I_t = 10pA, V_G = 70V) of MoS_2 monolayer showing the triangular atomic lattice, further highlighted in the inset by the six-fold symmetric structure visible in the 2D Fourier transform of the image. (d) Local STS map showing the differential conductance dI/dV measured at V_{tip} = -1.5V as a function of tip position. Three regions are identified: region 1 (which occupies most of the image) with no states inside the band gap (violet STS spectrum); region 2 (delimited by the green dashed line) in which pronounced states are seen in the spectrum, close to the top of the valence band; region 3 (delimited by the red dashed line) with in-gap states visible in the tunneling spectrum close to the top of the valence band that are broader in energy. Note that the sub-nanometer size of regions 2 and 3 indicates that the in-gap states originate from atomic-scale defects and is compatible with sulfur vacancies. The STM image in (c) and the STS map in (d) were collected from different areas of a same sample.

the states have sub-nanometer dimension, indicating that they originate from atomic defects (no more specific fingerprints enabling a direct identification of the defects could be obtained on gated CVD-grown MoS_2 layers on SiO_2, which prevents the direct identification of the defects by STM imaging alone). The states have energy close to the top of the valence band, as illustrated by spectra 2 and 3 on the left side of figure 5.5. Specifically, in region 2 the in-gap states lead to a fully developed, broad peak 400 meV above the top of the valence band, and in region 3 in a shoulder at a comparable energy (again 300-400 meV above the top of the valence band). The energy of these features (*i.e.,* their distance from the top of the valence band) coincide with what we observed in measurements of the source-drain current as a function of gate/reference potential (see figure 5.1b and figure 5.4). From this we conclude the in-gap states created by atomic scale defects are the same states acting as hole traps, which are responsible for the observed anomalous transport properties discussed above.

The combination of all the measurements presented so far (transport experiments on exfoliated and CVD-grown MoS_2 monolayers, their comparison, the comparison with the normal ambipolar behavior observed in other semiconducting TDMCs, photoluminescence and Raman measurements, and the STM and STS measurements just discussed), in conjunction with theoretical investigations based on *ab-initio* calculations reported in the literature[56,130,141,146,147], point to a realistic and fully consistent scenario accounting for the experimental observations. Specifically, we claim that the atomic scale defects that we observe and that are responsible for the anomalous hole transport in exfoliated MoS_2 monolayers are individual or clustered sulfur vacancies, which are known to be present in relative high density in MoS_2 bulk crystals, and therefore also in exfoliated monolayers. Spectroscopy measurements show that they create in-gap states near the top of the valence band acting as traps and strongly affecting hole transport, which is in agreement with expectations based on *ab-initio* calculations[56,141,147]. More specifically, it is known in the context of semiconducting TMDC monolayers that the detailed analysis of the electronic states generated by sulfur and selenium vacancies is complex, as these defects create different types of localized states. However, if we confine our attention exclusively to defect-induced states near the top of the valence band (*i.e.*, those states that can act as effective traps for holes), the results of virtually all existing *ab-initio* calculations[56,130,141,146,147] indicate that only in the case of MoS_2 monolayers these states are inside the band gap. In other semiconducting TMDC monolayers (WS_2, $MoSe_2$, and WSe_2) the energy of states near the top of the valence band generated by sulfur or selenium vacancies is actually in the band. As a result, in these other monolayers the defect states do not act as hole traps, because they can hybridize with delocalized states at the same energy. That is: sulfur vacancies explain why only in MoS_2 monolayers hole transport is anomalous. For MoS_2 bilayers or thicker multilayers the absence of any anomaly in hole transport is explained in a similar way: the decrease of the band gap with increasing the number of layers (by at least 0.5 eV for bilayers as compared to monolayers, and more for thicker multilayers) makes the states induced by sulfur vacancies "fall" into the valence band, preventing them from acting as hole traps.

Sulfur vacancies also accounts for other aspects of our observations. In particular, as we have remarked above, the defects affecting hole transport are the same in exfoliated monolayers and CVD-grown ones, albeit in CVD-grown monolayers their effect is less intense. Sulfur vacancies are compatible with this conclusion, as they are expected to be present in both systems. This is not the case for most other types of atomic defects: indeed, mineral MoS_2 crystals are known to contain a number of different impurities[148], but these same impurities are neither necessarily present in the Mo and S source material used for CVD growth, nor would they be effectively transferred to the monolayer during the growth process if present. That is why finding that the defects responsible for hole trapping are the same in exfoliated and CVD-grown monolayers strongly constraints the number of possibilities, and sulfur vacancies is one of the few. Finally, sulfur vacancies also naturally explain why the effect of disorder on hole transport is much less pronounced in devices fabricated on CVD-grown material, simply because under the conditions at which CVD growth is done a large excess of sulfur is present, which leads to largely reduced density of sulfur vacancies as compared to that present in exfoliated flakes.

5.5 Conclusion

Simple theoretical considerations suggest that monolayers of group VI semiconducting transition metal dichalcogenides all possess very similar electronic properties and functionality. Inasmuch as this may be the case for ideal defect-free systems, actual materials contain defects whose influence on the physical properties can (and do) strongly depend on the compound considered. Here we have shown that this is clearly the case for hole transport, which in monolayer MoS_2 – but not in monolayers of other common TDMCs – is strongly affected by defects naturally present. Our results very strongly support the conclusion that these naturally present defects are sulfur vacancies, and explain why these defects have a different effect in MoS_2 monolayers as compared to monolayers of other similar compounds, *i.e.* the fact that for MoS_2 monolayers sulfur vacancies cause localized defect states at energies inside the band gap. They also illustrate a possible solution to minimize the influence of these defects on the performance of devices realized using monolayer MoS_2, namely the use of material grown in a large excess of sulfur.

There is a broad consensus that 2D semiconducting materials have an important potential for technology in the long term. It is clear that exploiting this potential cannot only rely on properties of the idealized systems, but has to take into account the effect of defects unavoidably present, understand it in detail, and find strategies to minimize it. Our results illustrate how this can be done in a concrete specific case.

Chapter 6: Enhanced electron-phonon interaction in multi-valley materials

6.1 Introduction

The electronic and elastic properties of solids are determined by the interaction between charge carriers and the elementary excitations associated with the vibration of the crystalline lattice, namely the phonons. In view of its fundamental relevance, the nature of the interaction between electrons and phonons has been investigated in great depth in many different contexts[149–151]. In the simplest possible terms, electron-phonon interaction can be understood as originating from the electrostatic potential generated by the lattice distortion associated to the ionic displacement in the presence of a phonon. In other words, exciting a phonon in a crystal displaces the charged ions forming the lattice from their equilibrium positions, thereby generating a local charge imbalance and a corresponding electrostatic potential (known as deformation potential [152,153]), which in turn directly acts on all mobile electrons.

Depending on the specific type of material considered and on the level of detail needed for a precise microscopic understanding, the situation can be more complex. For instance, in some systems (among which, graphene) the coupling between the lattice deformation associated to certain phonon modes and charge carriers is described in terms of a vector potential, rather than an electrostatic one[154,155]. In these cases, the phonon perturbation of the electronic Hamiltonian is formally equivalent to a magnetic field[156]. Also, the influence of electron-phonon interaction on physical phenomena depends strongly on whether the energy and momentum relaxation of electrons is fast or slow relative to the phonon frequency, corresponding to the so-called adiabatic or anti-adiabatic limit of electron-phonon cou-

---

The results presented in this chapter have been submitted to *Physical Review X* and uploaded to https://arxiv.org/abs/1901.08012v1, Evgeniy Ponomarev, Thibault Sohier, Marco Gibertini, Helmuth Berger, Nicola Marzari, Nicolas Ubrig and Alberto F. Morpurgo. The DFT calculations and theoretical analysis were done in collaboration with the group of Prof. Nicola Marzari by Thibault Sohier and Marco Gibertini.

pling[157,158].

Irrespective of the specific situation, what is key to understand electron-phonon interaction (and its strength) in solids is electrostatic screening[151]. Indeed, the deformation potential generated by the excitation of a long wavelength phonon tends to be screened by the spatial redistribution of the electrons present in the system, which self-consistently reduces the strength of the electron-phonon coupling[159–161]. Screening is expected to be much more effective in the adiabatic regime –since then electrons are able to equilibrate sufficiently fast in response to the ionic motion– and a much weaker electron-phonon coupling is accordingly expected in this regime as compared to the antiadiabatic one. Conversely, if the nature of the electron-phonon coupling is described in terms of a vector potential, as we mentioned it is the case for some of the phonons in graphene[162,163], screening cannot influence electron-phonon coupling[155,164] (just like no spatial distribution of charge carriers can screen a magnetic field). In this case, electron-phonon coupling is expected not to be significantly affected by the presence of charge carriers.

In semiconducting materials hosting only a small density of mobile charges, electrostatic screening is poor and a strong electron-phonon interaction is expected. Addition of charge carriers (e.g., by doping) can drastically improve screening and cause the strength of electron-phonon interaction to decrease, as observed in a variety of semiconductors (e.g., $SrTiO_3$[165–167] and other transition metal oxides[168]). For those cases in which electron-phonon interactions cannot be screened, one would expect no effect from the addition of charge carriers, as it happens in graphene[155]. In virtually no case, however, the strength of electron-phonon interaction in a semiconductor is expected to increase significantly upon adding charge carriers.

In contrast with this established understanding, here we uncover a yet unidentified mechanism that causes a very significant strengthening –and not a weakening– of electron-phonon coupling in atomically-thin semiconductors upon increasing electron density. Our work relies on a joint experimental and theoretical investigation of Raman spectroscopy performed on mono and bilayers of different semiconducting transition metal dichalcogenides (TMDs; MoS_2, WS_2, and WSe_2) as a function of density of accumulated charge carriers. By integrating all these atomically-thin layers in ionic-liquid-gated field-effect transistors (FETs) we have measured the evolution of the Raman spectrum as a function of electron and hole density up to approximately 5×10^{13} cm^{-2}. In all investigated mono and bilayers, the experiments reveal unambiguously that the electron-phonon interaction systematically softens out-of-plane vibrational modes only when electrons are accumulated in the FET channel, while leaving them unaffected upon hole doping. To identify the origin of this unexpected electron-hole asymmetry we have performed density-functional-theory (DFT) calculations in the most realistic framework currently available, accounting for the reduced dimensionality of the materials and for the presence of a finite density of charge carriers[169]. The calculations allow us to conclude that the observed phonon softening originates from a pronounced increase in the strength of the electron-phonon coupling that occurs whenever the charge carriers in the systems populate simultaneously two inequivalent valleys. Besides accounting for the observed electron-hole asymmetry (as a direct consequence of the different valley structure in the conduction and valence bands of atomically-thin semiconducting TMDs), this finding reveals an aspect of electron-phonon coupling that had not yet been appreciated. Specifically, the strengthening of the electron-phonon coupling is caused by charge transfer between inequivalent valleys with opposite deformation potentials. Being local in real space, this inter-valley charge transfer decreases the spatial variation of charge associated with the phonon perturbation, making it insensitive to screening. The phenomenon –expected to be of rather general validity– had not been identified so far, most likely because the models commonly used to describe electron-phonon interaction theoretically do not consider the presence of multiple inequivalent valleys. Equipped with the understanding resulting from the work presented here, we discuss how existing experiments on superconductivity in TMDs (both gate-induced[77,170–172] and spontaneously occurring[173–177]) could provide evidence correlating the enhancement in electron-phonon interaction due to multivalley populations to the occurrence of the superconducting state.

6.2 Electron-hole asymmetry of out-of-plane Raman active mode in TMDs

Our experiments consist in measurements of the Raman spectrum of mono and bilayers of different semiconducting TMDs (WSe_2, WS_2, and MoS_2) as a function of carrier density. The density and polarity of charge carriers is varied continuously by employing these atomically-thin crystals as active parts of ionic-liquid-gated FETs (see figure 6.1(a) for a schematic illustration). It has been shown in a multitude of experiments over the last several years that ionic-liquid gating is extremely effective in combination with semiconducting TMDs, as it allows the accumulation of large densities (even in excess of 10^{14} cm^{-2}) of both electrons and holes in a same device[76,77,79,80,170,178–183]. One of the characteristic manifestations of the possibility to vary the charge density and type over such a large interval is the occurrence of ambipolar transport, which can be observed upon sweeping the gate voltage $\mathrm{V_G}$ (see figure 6.1(a) for an example). In the present context, the occurrence of ambipolar transport is useful because it allows us to obtain a fairly accurate estimate of the carrier density in the devices used for the Raman measurements *in-situ*. In practice, in the experiments we record the Raman spectrum at many different values of applied gate voltage and –as we vary $\mathrm{V_G}$– we also apply a small bias voltage, $\mathrm{V_{SD}}$ between the source and the drain electrode to measure the current, $\mathrm{I_{SD}}$, passing through the transistor channel. This allows us to determine the threshold voltage for electron and hole conduction –V_{th}^{e} and V_{th}^{h}– from which we directly estimate the density of electrons and holes at any given value of $\mathrm{V_G}$ as $n_e = \frac{C|V_G - V_{th}^{\mathrm{e}}|}{e}$ and $n_h = \frac{C|V_\mathrm{G} - V_{th}^{\mathrm{h}}|}{e}$ (where C is the capacitance per unit area obtained from previous experiments on analogous devices, in which Hall-effect measurements were performed to determine the density of charge carriers). We estimate the uncertainty in the value of carrier density extracted in this way to be approximately 20-30 %, which is sufficient for the purpose of this work (a more precise determination would require measuring the Hall resistance using a superconducting magnet which cannot be done in the same set-up that we use to perform Raman spectroscopy). For more details concerning the fabrication and operation of ionic-liquid FETs based on atomically-thin TMDs we refer the reader to our earlier work[76,77,80].

Characteristic Raman spectra from bare monolayers of $\mathrm{WSe_2}$ (blue line), $\mathrm{WS_2}$ (orange line), and $\mathrm{MoS_2}$ (green line) are shown in figure 6.1(b). We focus on the most prominent features in these spectra, whose assignment in terms of Raman active vibrational modes has been discussed extensively in the literature[184–188]. Using for simplicity the same nomenclature as in the bulk, these are the in-plane ($\mathrm{E_{2g}}$) and the out-of-plane ($\mathrm{A_{1g}}$) modes, as indicated in figure 6.1(b), which are seen in all group-VI TMDs. The displacement pattern of these phonon modes is schematically reported in figure 6.1(c). For $\mathrm{WS_2}$ and $\mathrm{MoS_2}$ these features are spectrally separated while for $\mathrm{WSe_2}$ the modes hybridize due to an accidental degeneracy in the phonon dispersion relation, and appear as a single peak at about 250 cm^{-1}. The degeneracy is also present in the calculated phonon dispersion relation of $\mathrm{WSe_2}$ in figure 6.1(d), on which we point to the modes observed in the Raman spectroscopy data. For most peaks the observed frequency corre-

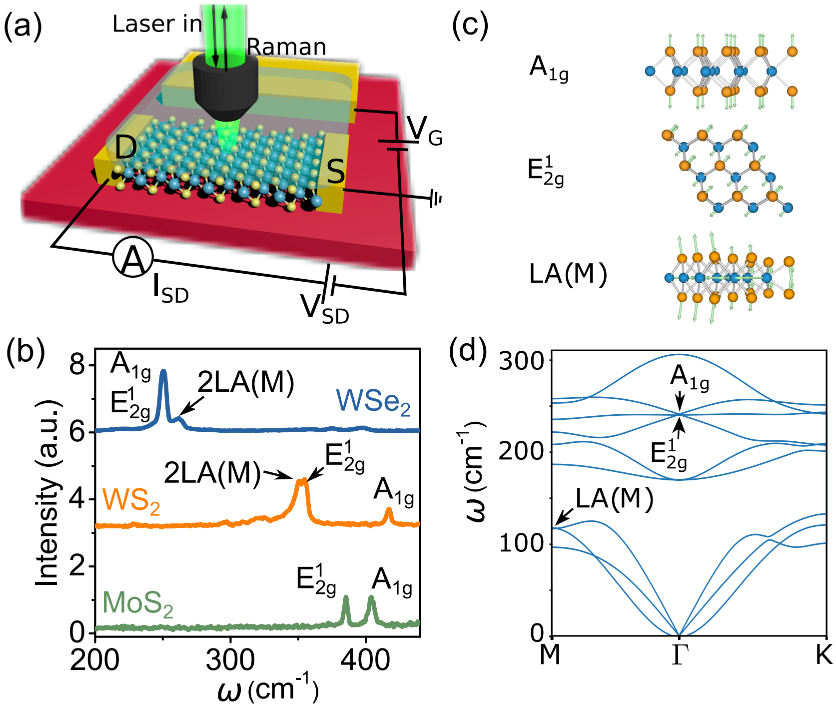

Figure 6.1: (a): Schematics of a ionic-liquid-gated monolayer TMD, showing the biasing configuration employed to operate the device as a field-effect transistor, as well as the microscope objective used to focus the laser light on the device and to couple the light emitted to the spectrometer. (b): Raman spectra measured at room temperature of bare exfoliated monolayers of WSe_2 (blue line), WS_2 (orange line), and MoS_2 (green line). The peaks visible in the curves originate from the A_{1g}, E_{2g}, and 2LA(M) modes, as indicated in the figure. (c) Sketches of the atomic displacement pattern for the different Raman active modes. (d) Phonon dispersions of a pristine WSe_2 monolayer in absence of doping obtained by DFT calculations. In WSe_2 the A_{1g} and E_{2g} modes are degenerate at the Γ-point making them undistinguishable in the Raman spectrum, as can be seen in (b).

sponds to the value of the corresponding mode at the Γ-point. However one of the peaks, visible in the spectra of both WSe_2 and WS_2 and labeled 2LA(M) (see figure 6.1(b)), is due to a double resonant process[189,190], which occurs because the frequency of the laser used in our measurements matches an electronic transition (C absorption for WSe_2 and the B-exciton for WS_2)[191]. Although it is not the main point of interest here, the possibility to observe this mode is relevant because it allows the investigation of the coupling between electrons and phonons at finite momentum, *i.e.*, away from center of the Brillouin zone, as indicated by the corresponding label LA(M) in figure 6.1(d).

To illustrate the results of our Raman spectroscopy measurements as a function of accumulated charge density we start by discussing the case of WSe_2 monolayers. The source-drain current I_{SD} as a function of V_G (for V_{SD} = 50 mV) measured in the device used for the Raman measurements, is presented in figure 6.2(a) and exhibits clear ambipolar behavior. The

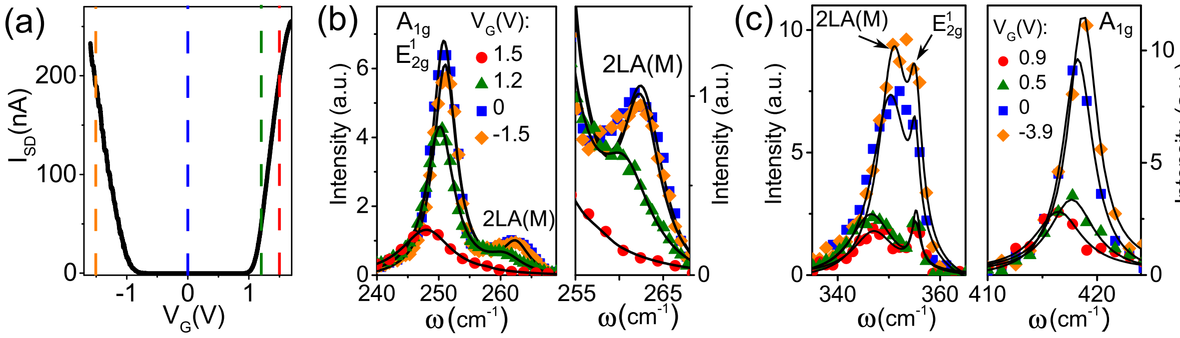

Figure 6.2: (a): Source-drain current I_{SD} as a function of gate voltage V_G measured on a WSe_2 monolayer (source-drain bias V_{SD} = 50 mV), exhibiting clear ambipolar transport. This curve is measured *in-situ*, with the device mounted in the set-up used to perform Raman spectroscopy, and it enables us to estimate the density of carriers at any given value of V_G as discussed in the main text. (b) Left: Raman spectrum of WSe_2 monolayer at selected gate voltages indicated in the legend and corresponding to the values of V_G marked with the dashed lines of different colours in (a). The peak near 250 cm^{-1} originates from the degenerate A_{1g} and E_{2g} modes, and the one near 250 cm^{-1} is due to a resonant electronic process involving the LA(M) mode. In all cases the black lines are fit of the data to Lorentzian-shaped peaks centered around the energy of the different modes identified. Right: zoom in on the spectral region around the peak due to the resonant process involving the LA(M) mode. (c) Left: Peaks in the Raman spectrum of WS_2 bilayer originating from the E_{2g} and 2LA(M) modes for different values of gate voltage (see legend in the right panel). Right: Peak in the Raman spectrum due to the A_{1g} mode measured at the gate voltages indicated in the legend (black lines are fits of the data obtained by introducing a Lorentzian-shaped peak for each one of the modes involved). As for WSe_2 monolayer the spectra are strongly affected upon electron accumulation; the A_{1g} and 2LA(M) modes shift to lower wavenumbers (i.e. softening) and decrease in intensity, whereas they are left virtually unchanged upon hole accumulation. The position of the E_{2g} peak remains constant for both electron and hole accumulation.

increase of I_{SD} at positive values of V_G indicates accumulation of electrons in the FET channel while the increase of I_{SD} at negative V_G corresponds to the accumulation of holes. As explained above, we use these measurements to estimate the density of electrons and holes as a function of V_G. Figure 6.2(b) shows the Raman spectra measured for selected values of V_G indicated by the vertical dashed lines in figure 6.2(a). For positive values of V_G electrons are accumulated (green and red lines, i.e. $V_G = +1.2$ and $+1.5$ V, corresponding respectively to $n_e \sim 1.5 \times 10^{13}$ and 2.5×10^{13} cm^{-2}), for negative V_G values the gate accumulates holes (orange line, i.e. V_G = -1.5 V, corresponding to $n_h \sim 6 \times 10^{13}$ cm^{-2}), whereas for $V_G = 0$ V (blue line) the chemical potential is in the gap and the semiconductor is neutral[192]. Upon electron accumulation the Raman peak originating from the hybridized A_{1g}/E_{2g} mode exhibits a clear softening, shifting towards lower wavenumbers by an amount $\Delta\omega \simeq 3 - 4$ cm^{-1}, as well as a decrease in intensity as compared to $V_G = 0$ V case. In contrast, accumulation of holes leaves the Raman spectrum virtually unchanged: the peak does not exhibit any appreciable shift, and only its height decreases slightly. The same trends upon varying $\mathrm{V_G}$ are observed for the resonant Raman peak originating from the 2LA(M) mode, shown in the right panel of figure 6.2(b) [193].

Since in $\mathrm{WSe_2}$ monolayers the degeneracy of the $\mathrm{E_{2g}}$ and $\mathrm{A_{1g}}$ modes prevents us to study separately the evolution of the two individual Raman peaks upon accumulation of charge carriers, in figure 6.2(c) we show data from bilayer $\mathrm{WS_2}$, in which these modes are well separated in frequency. The corresponding Raman peak positions at $\mathrm{V_G} = 0$ V are located respectively at $\omega = 355\ \mathrm{cm^{-1}}$ – figure 6.2(c), left panel– and $417\ \mathrm{cm^{-1}}$ – figure 6.2(c), right panel. The same figures also show the Raman spectra measured at selected values of $\mathrm{V_G}$, in a range of carrier density somewhat larger than for monolayer $\mathrm{WSe_2}$. For values of $\mathrm{V_G}$ corresponding to hole accumulation only a negligible shift in position, and at most a small change in amplitude, are seen for all peaks. In contrast, upon electron accumulation, the $\mathrm{A_{1g}}$ and the 2LA(M) modes exhibit a clear softening similarly to what is observed in $\mathrm{WSe_2}$ (the position of the $\mathrm{E_{2g}}$ mode remains unaffected even for electron accumulation).

Figure 6.2 reveals a number of clear trends of the Raman active modes in $\mathrm{WSe_2}$ monolayer and $\mathrm{WS_2}$ bilayer, such as the insensitivity of all phonon modes to hole accumulation, and the softening of out-of-plane modes upon electron accumulation. We have performed gate-dependent Raman spectroscopy measurements on mono and bilayers of $\mathrm{WSe_2}$, $\mathrm{WS_2}$ and $\mathrm{MoS_2}$ following a procedure identical to the one described here above for $\mathrm{WSe_2}$ monolayer and $\mathrm{WS_2}$ bilayer, and found that these trends are generically present in all the investigated atomically thin crystals of semiconducting TMDs. To illustrate and compare quantitatively the results of measurements performed on different systems we plot for each one of them the change $\Delta\omega$ in the frequency of the different phonon modes relative to the value measured at threshold for electron or hole accumulation (*i.e.,* , for each system we plot $\Delta\omega$ versus $V_\mathrm{G} - V_\mathrm{th}^\mathrm{e}$ and $V_\mathrm{G} - V_\mathrm{th}^\mathrm{h}$). The results of these measurements for the $\mathrm{A_{1g}}$ modes in all the investigated mono and bilayers are summarized in figure 6.3(a) and 6.3(b). The data for the $\mathrm{E_{2g}}$ modes in monolayers are shown in figure 6.3(c). It is clear from this systematic experimental analysis – which goes well beyond what had been done until now [194,195] – that the same behavior is common to all atomically-thin group-VI TMDs.

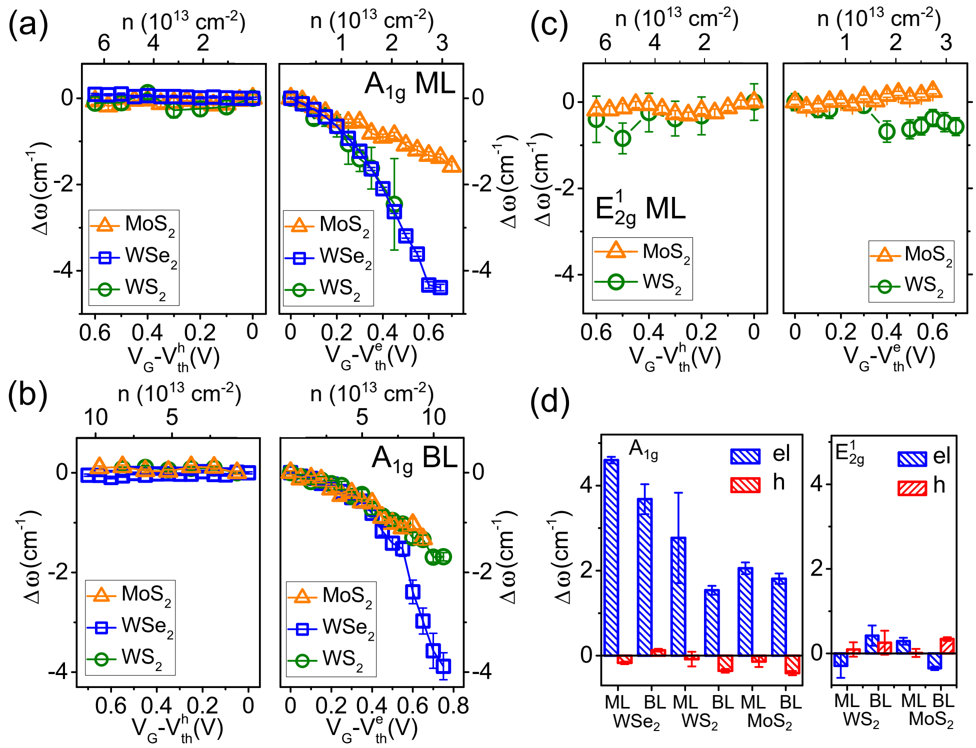

Figure 6.3: (a): Shift $\Delta\omega$ of the A_{1g} peak position in MoS_2 (yellow open triangles), WSe_2 (blue open squares), and WS_2 (green open circles) monolayers as a function of gate voltage (bottom axis), relative to the threshold voltage for hole accumulation (left panel) and for electron accumulation (right panel). The values of electron and hole density corresponding to the applied gate voltage –estimated using the capacitance of the ionic liquid gate, $n_{e,h} = \frac{1}{e}C|V_G - V_{\mathrm{th}}^{\mathrm{e,h}}|$– is indicated on the top axis (the capacitance values are largely determined by the density of states, as discussed in note[192]). The position of the Raman peak originating from the A_{1g} mode remains unchanged for all TMD monolayers upon hole accumulation and shifts upon electron accumulation. (b): Same as (a) for the A_{1g} mode of bilayers of the same TMD compound, MoS_2 (yellow open triangles), WSe_2 (blue open squares), and WS_2 (green open circles). The trends and the order of magnitude of the frequency softening are identical in mono and bilayers. (c): The E_{2g} peak in monolayer MoS_2 (yellow open triangles) and WS_2 (green open circles) remains constant irrespective of the applied gate voltage (the left panel corresponds to hole accumulation and the right one to electron accumulation; for WSe_2 the investigation of the E_{2g} mode is prevented by the degeneracy with the A_{1g} mode). The same insensitivity of the E_{2g} mode to charge accumulation is seen in bilayers (not shown). (d): To summarize the effect of electron and hole accumulation on the softening of the A_{1g} and E_{2g} phonon modes we compare the absolute shift of the peak position at the highest gate voltage value for all different investigated mono and bilayer TMDs, $|V_G\text{-}V_{\mathrm{th}}^{\mathrm{e,h}}| = 0.6$ V. The left and right panels summarize the values measured for the A_{1g} and E_{2g} mode respectively, for either electron (blue bars) or holes (red bars). It is clear from these plots that only the A_{1g} modes (with an out-of-plane motion component of the atomic displacement) are affected by introduction of carriers, and only if electrons are accumulated.

To quantify the strength of the influence of electron and hole accumulation on the frequency of the different phonons, we plot for all systems investigated the frequency shift of the A_{1g} and E_{2g} modes measured at the highest value of applied gate voltage applied (relative to the corresponding threshold voltage), $|V_{\mathrm{G}} - V_{\mathrm{th}}^{\mathrm{e,h}}| = 0.6$ V, for which we have obtained data for both mono and bilayer, as well as for electron and hole accumulation. Figure 6.3d demonstrates clearly that, for both mono and bilayers, only Raman active phonon modes with an out-of-plane component of the atomic displacement are influenced by the presence of charge carriers, whereas the $\mathrm{E_{2g}}$ mode – for which the atomic displacement is in-plane – is left unaffected by the presence of free charge. The data also make the strong electron-hole asymmetry in the softening of the out-of-plane modes very apparent for all the different TMDs investigated. The order of magnitude of the effect – which is what we discuss here – is the same in all cases, corresponding to a shift of 2-4 cm^{-1} for the $\mathrm{A_{1g}}$ mode (for a more detailed quantitative analysis it should be recalled that – since the value of the capacitance used is different for mono and bilayers and for electron and hole accumulation – the same value of gate voltage relative to threshold does not correspond to the same carrier density[192]).

6.3 Theoretical analysis

The experiments discussed in the previous section show unambiguously that a strong electron-hole asymmetry in the softening of the phonon frequency is a generic property of atomically-thin semiconducting TMDs. The microscopic mechanism at the origin of this asymmetry, however, is not known and, especially for monolayers, finding such a pronounced asymmetry is unexpected. Indeed, the low-energy electronic states in $\mathrm{WSe_2}$, $\mathrm{WS_2}$, and $\mathrm{MoS_2}$ monolayers at the bottom of the conduction band and at the top of the valence bands – centered around the K/K' points – are often described in terms of massive Dirac fermions, a conceptual framework that may lead one to expect a high degree of symmetry in the physical response upon accumulation of electrons and holes. Even though the very different strength of spin-orbit interaction in the conduction and valence band limits the validity of these considerations, whether and how spin-orbit interaction can cause such a strong asymmetry in the phonon properties upon electron and hole accumulation is very far from obvious.

The purpose of this section is to present a theoretical analysis showing that the strength of the electron-phonon interaction in these materials is governed by whether or not multiple valleys (the Γ and K valleys in the valence band and the K and Q valleys in the conduction band, see figure 6.4) are simultaneously populated by the accumulated charge carriers. In other words, it is the rather different valley structure of the conduction and the valence bands that is ultimately responsible for the difference in the coupling to phonons of electrons and holes, and that causes the observed electron-hole asymmetry in the softening of the phonon frequencies. In this regard, spin-orbit interaction does play a prime role, because its strongly asymmetric strength between valence and conduction bands governs the energetic alignment of the different valleys, and therefore determines whether – at any given value of carrier density – one or multiple valleys are populated.

This conclusion is based on DFT and density-functional perturbation theory (DFPT) calculations, which provide an extremely powerful tool to identify all trends in the observed dependence of the phonon frequency on the density of accumulated charge. DFT, however, cannot reproduce the experiments at a detailed quantitative level. This is because a full quantitative agreement would require a precise prediction of the relative energetic alignment of the valleys present in the valence and conduction band, which is well-known to be extremely sensitive to multiple parameters[196–200], from the choice of exchange-correlation functional to details of the crystal structure and screening from free carriers or the environment. Indeed, even experimental attempts to determine precisely the energetics of the different valleys seem to give scattered results, depending – for instance – on the substrate employed in the experiments (see Table 2). The situation is even more complex for bilayers, where the electric field associated with the FET doping influences the relative energy of the valleys in a way that cannot be precisely predicted at this stage. As such, our analysis aims exclusively at exploiting the possibility to tune parameters and conditions in the controlled environment of DFT simulations to identify the physical processes that explain our experimental results, and not at reproducing in quantitative detail the observed carrier density dependence of the phonon frequencies. That is also why –in view of the subtle effects caused by the gate electric field in bilayers– we focus our theoretical analysis exclusively on TMD monolayers.

We first note that the softening is expected when describing electron-phonon interactions within the Born-Oppenheimer approximation, where electrons remain at all times in the ground state corresponding to the instantaneous lattice configuration. This implies that phonons can be considered as static perturbations acting on the electrons, which in turn affect the vibrational properties of the system. In this regime, the expression for the change in frequency of a phonon at Γ with respect to the neutral semiconducting case reads (see Refs.[207–209]):

Table 2: Energy separation $\Delta E_{\Gamma\text{K}}$ between the top of the valence band at K and Γ in the monolayer TMDs investigated in this work. Experimental results are taken from angle-resolved photo-emission spectroscopy (ARPES) measurements in the literature. DFT data refer to calculations done in the present work.

	$\Delta E_{\Gamma\text{K}}$ (meV)		
	MoS_2	WS_2	WSe_2
Exp.	150[201], 310[199,202]	510[203], 240[204],300[205]	560[206], 500[15], 890[197]
DFT (this work)	60	230	490

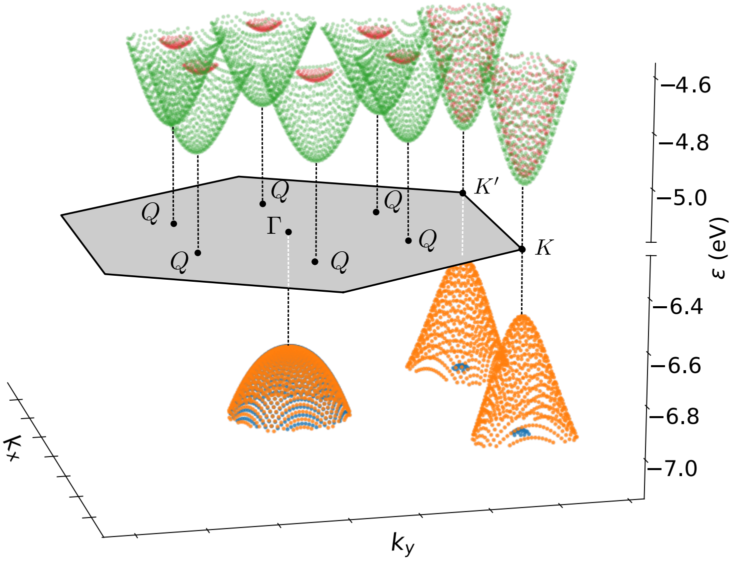

Figure 6.4: The low-energy valley structure of the conduction and valence bands is common to all the TMD monolayers investigated here. This figures illustrates it by showing the low-energy parts of the conduction and valence bands of WS_2 monolayers (the grey shaded hexagon represents the Brillouin zone). The top of the valence band (shown in orange and blue) is formed by a single spin-degenerate valley around Γ and a spin-split, two-fold degenerate valley at the K/K′ point. The bottom of the conduction bands (represent in green and red) is composed of an almost spin-degenerate valley at the K/K′ point (with degeneracy two) and a six-fold degenerate spin-split valley approximately midway between Γ and K, normally referred to as the Q point.

$$\Delta\omega_\nu \approx -N(\varepsilon_F)\langle g_\nu^2\rangle_{FS}. \tag{6.1}$$

Here we assume the limit of zero temperature, $N(\varepsilon_F)$ is the density of states at the Fermi energy, ε_F, and $\langle g_\nu^2\rangle_{FS}$ is the screened electron-phonon coupling (squared) for the ν-th phonon mode averaged over the Fermi surface. It follows that softening ($\Delta\omega_\nu < 0$) is expected only for phonon modes that are strongly coupled with the electronic states on the Fermi surface. For instance, this is not the case of the pure E_{2g} longitudinal optical mode, which affects electrons by generating a long-range scalar potential (known as Fröhlich interaction) that in the presence of free carriers (either electrons or holes) is perfectly screened in the long-wavelength limit, so that $\langle g_\nu^2 \rangle_{FS} \approx 0$.

The Born-Oppenheimer approximation is a good description only for systems that are in the adiabatic limit. This requires the phonon energy $\hbar\omega_\nu$ to be much smaller than the carrier relaxation rate $\hbar/\tau$ ($\omega_\nu\tau \ll 1$), where τ is the carrier momentum-relaxation lifetime. The value of τ can be estimated from the experimentally determined carrier mobility that – under the conditions of the experiments – is typically $\mu \approx 15$ cm^2/Vs for both electrons and holes. When compared to the characteristic phonon frequencies probed in our experiments, the resulting value of $\tau \approx 10$ fs gives $\omega_\nu\tau \leq 1$. The Born-Oppenheimer approximation is therefore fairly well justified. Note also that, even when $\omega_\nu\tau \simeq 1$, theory allows the phonon softening to be estimated as[158,208,210]:

$$\Delta\omega_\nu^{(\tau)} \approx \frac{\Delta\omega_\nu}{1 + (\omega_\nu\tau)^2} \tag{6.2}$$

where $\Delta\omega_\nu$ is given by Eq. (6.1). It follows directly from this expression that the adiabatic limit represents an upper bound for the phonon softening measured in experiments by at most a factor of two.

Since DFT calculations of phonon frequencies are done within the Born-Oppenheimer approximation, they are an appropriate tool to simulate the softening in monolayer TMDs. We first investigate which phonon modes are sensitive to accumulation of charge carriers by computing phonon dispersions of neutral, electron-doped and hole-doped monolayer TMDs using DFPT[211]. Since simulations require overall charge neutrality, the accumulated charge is compensated by the presence of gate electrodes, and the correct boundary conditions for 2D materials are provided by cutting off the Coulomb interactions in the direction perpendicular to the layers[169]. In these initial calculations, spin-orbit coupling is not included and a relatively large electronic temperature is used to smear the Fermi surface.

Representative DFPT results are shown in figure 6.5 for WS_2. When a finite density of carriers is included, we observe a softening in various branches at several phonon wave vectors. In particular, we see that the

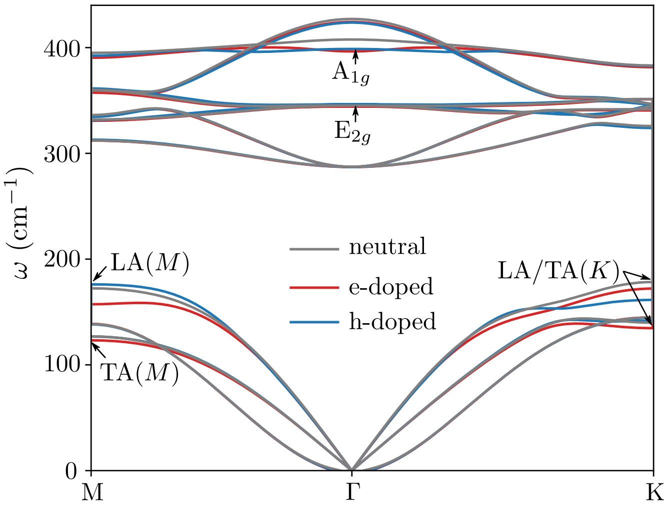

Figure 6.5: Dispersion relations of the different phonons branches, calculated as described in the main text, along the high-symmetry path M-Γ -K of monolayer WS$_2$. Lines of different colours correspond to either neutral (grey lines) monolayers, or monolayers under electron (blue lines), and hole (red lines) accumulation (calculations are done for 0.02 electrons or holes per unit cell).

A$_{1g}$ mode softens at Γ both for electron and hole accumulation, and at M for electron accumulation only. Similarly, the frequencies of the in-plane acoustic modes (LA and TA) decrease at K both upon electron and hole accumulation, and at M exclusively for electron accumulation. On the contrary, the E$_{2g}$ mode remains unaffected. For all the phonon modes detected in the experiments, therefore, the simulations succeed in reproducing which modes soften upon accumulation of charge carriers. However, the overall agreement between calculations and experiments is poor. The magnitude of the softening is largely overestimated, well beyond the factor $[1+(\omega_\nu\tau)^2]$ accounting for deviations from the purely adiabatic approximation of DFT. In addition, softening appears also upon hole-doping for the A$_{1g}$ mode at Γ, in contrast with the experimental results.

To investigate the origin of the discrepancy between measurements and simulations, we focus our attention on the A$_{1g}$ mode[193]. We computed the A$_{1g}$ frequency at Γ as a function of carrier density using a finite-difference DFT scheme for the three monolayer TMDs investigated here. At this stage, we made calculations more realistic by including spin-orbit coupling through fully-relativistic pseudopotentials, and by describing the occupation of electronic states according to the room-temperature Fermi-Dirac distribution (for which we made a much denser sampling of the Brillouin zone). Again, all calculations include a cutoff of the Coulomb interaction to implement the correct periodic boundary conditions, and gates to maintain overall charge neutrality and properly simulate a FET configuration.

Results for monolayers of the three different TMDs investigated experimentally are shown in figure 6.6, both for electron and hole accumulation, in a range of carrier densities comparable to that explored in the experiments. In contrast to the very systematic results of the Raman measurements (see figure. 6.3), the evolution of the calculated phonon frequency upon electron and hole accumulation is different for the individual TMDs, and appears at first sight to offer no systematics. In particular, we find that for WS_2 (figure 6.6a) a large softening occurs on the electrons side, but the A_{1g} mode frequency decreases also upon hole doping (see also figure 6.5). For WSe_2 (figure 6.6b) instead a significant softening is present only for electrons and not for holes, whereas the opposite is true for MoS_2 (figure 6.6c). Despite this seemingly erratic behavior, there is a clear and systematic correlation between the softening and the fractional occupation P of the different valleys plotted in the bottom panels of figure 6.6.

In all cases a strong softening of the A_{1g} mode occurs only when two inequivalent valleys are simultaneously occupied, whereas the frequency of this mode remains constant whenever the accumulated carriers occupy exclusively one of the valleys. Specifically, the rapid decrease of the A_{1g} frequency upon electron doping in WS_2 and WSe_2 originates from the simultaneous occupation of the K and Q valleys (see figure 6.6 a and b, respectively). Consistently with this idea, in MoS_2 only the K-valley is populated, and no significant softening is observed. Analogous trends are seen upon hole accumulation: A large softening is present in MoS_2 , for which the K and Γ valleys are simultaneously occupied, whereas no softening is visible in WSe_2 where holes populate only the K valley (see figure 6.6c and b, respectively). The case of WS_2 monolayers (figure 6.6a) confirms this notion. In this case, the frequency of the A_{1g} mode is insensitive to hole doping for small concentrations –when only the K valley is occupied– and starts to soften past 0.02 holes/unit cell, when holes begin to populate both the K and the Γ valley. In all cases a very pronounced softening is always seen when two distinct valleys are populated, whereas whenever only one valley is populated the change in phonon frequency is typically at least one order of magnitude smaller.

It follows from these considerations that the energy separation between valleys, which governs their relative occupation, plays an essential role in determining the magnitude of the shift in phonon frequencies (i.e., the

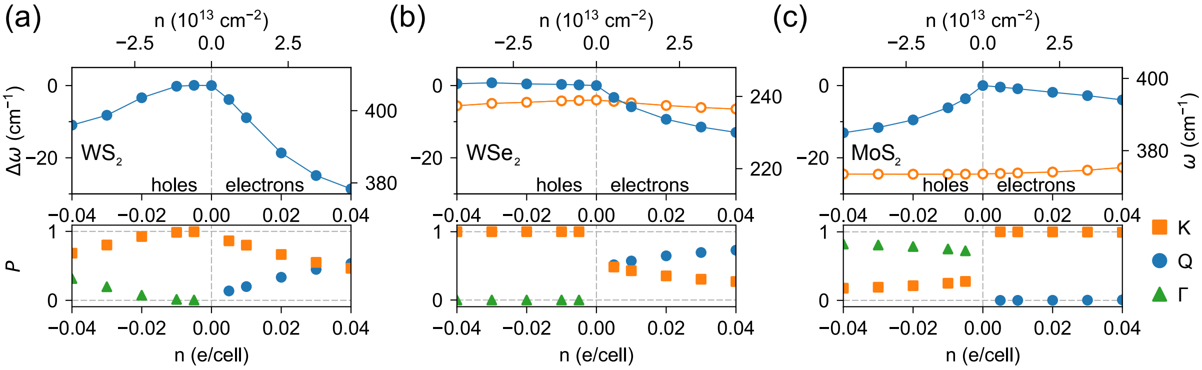

Figure 6.6: Top panels: Results of ab-initio calculations showing the dependence of the A_{1g} mode frequency (blue circles) on carrier density n in monolayer WS_2 (a), WSe_2 (b), and MoS_2 (c), for either electron ($n > 0$) or hole ($n < 0$) accumulation, as indicated in each panel. The range of carrier density considered in the calculations roughly corresponds to that explored in the experiments (see figure fig:raman(a)). For WSe_2 and MoS_2 we also plot the results for the E_{2g} mode (orange empty circles), which is found not to shift, in agreement with experiments (for WS_2 the E_{2g} mode is degenerate with the A_{1g} mode which experimentally prevents its separate determination upon varying carrier density). Lower panels: relative fractional occupation P of the different valleys upon hole and electron accumulation, as extracted from ab-initio calculations done to obtain the density dependence of the phonon frequencies shown in the corresponding top panels. Different symbols refer to the K (orange squares), Q (blue circles), and Γ (green triangles) valleys. Note how in all cases –i.e., for all the different monolayers and upon both electron and hole accumulation– there is a perfect correlation between the shift of the A_{1g} mode and the multiple occupation of valleys (i.e., the K and Γ valley in the valence band upon hole accumulation, and the K and Q valley in the conduction band upon electron accumulation).

strength of the electron-phonon coupling) upon carrier accumulation. To confirm this conclusion – and to provide further support for the effect of multivalley populations – we have performed additional calculations exploiting the extreme sensitivity of TMDs' band structures to the in-plane lattice parameter and the vertical positions of the chalcogen atoms[199]. The goal of these calculations is to artificially tune the energy separation between valleys in order to check whether, as we expect, the softening of the A_{1g} mode is affected significantly. We have analyzed the behavior of MoS_2 monolayers using the experimentally-reported crystal structure (rather than the fully relaxed one obtained by minimizing forces and stresses at the DFT level), for which the energy separation $\Delta E_{\Gamma K}$ between the K and Γ valleys in the valence band increases from 60 meV to 220 meV (see figure 6.7c), and the energy difference ΔE_{KQ} between the K and Q valleys in the conduction band decreases from 230 meV to 30 meV. To reduce the spurious effects of thermal broadening in these calculations, we intentionally determine band occupations by using a cold-smeared distribution[212] with $T = 150$ K, instead of a broad Fermi-Dirac distribution at $T = 300$ K as above.

The outcome of the calculations is illustrated in figure 6.7, where we compare the carrier-density dependence of (a) the frequency of the $\mathrm{A_{1g}}$ mode and (b) the fractional valley occupations obtained with either the DFT-relaxed structure (empty symbols, see also figure 6.6(c)) or the experimentally reported one (full symbols). It is apparent that the results are distinctly different in the two cases. Upon hole accumulation a large frequency shift and a simultaneous population of the K and Γ valleys are present for calculations performed using the DFT-relaxed structure. In contrast, no shift in frequency occurs in the calculations performed with the experimentally-reported crystal structure, where the fractional occupation of the K valley remains equal to one, i.e. only the K valley is populated. This is exactly the behavior that we would have anticipated as a result of the increased $\Delta E_{\Gamma\mathrm{K}}$ for the experimentally-reported crystal structure. Consistently, the reduction in ΔE_{KQ} (see figure 6.7c) in the experimentally-reported structure leads to a non-negligible occupation of the Q valley in addition to the lowest-lying K valley, causing a very large enhancement of the $\mathrm{A_{1g}}$ softening upon electron accumulation.

We therefore conclude that the scenario hypothesized above is correct: for all monolayers investigated here, and for both electron and hole accumulation, a very sizable softening of the $\mathrm{A_{1g}}$ mode occurs only when charge carriers populate multiple inequivalent valleys. Through Eq. (6.1), this directly implies that also the strength of the electron-phonon coupling for the $\mathrm{A_{1g}}$ mode in semiconducting TMDs is large only when two valleys are occupied. Such a mechanism had not been identified earlier. It is nevertheless extremely likely that this mechanism is at play in many other material systems besides semiconducting TMDs, and relevant to explain a variety of physical phenomena (see, e.g., the discussion of superconductivity in section 6.4).

The insight gained on the importance of the simultaneous occupation of multiple valleys can now be exploited to discuss in more detail the results of our Raman spectroscopy experiments (see figure. 6.3). To start with, the complete absence of phonon softening upon hole accumulation indicates that $\Delta E_{\Gamma\mathrm{K}}$ is sufficiently large in TMD monolayers to avoid the partial occupation of the Γ valley (in addition to the dominant K valley), for hole concentrations as large as $\sim 5 \times 10^{13}$ cm^{-2}. According to the same logic, the phonon softening observed upon electron accumulation indicates

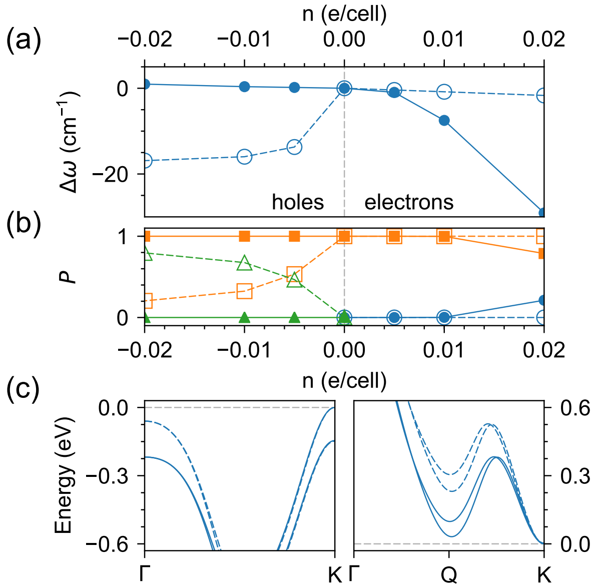

Figure 6.7: Effect of the crystal structure of monolayer MoS_2 on the softening of the A_{1g} mode (a) and on the fractional occupation P of the K (squares), Q (circles), and Γ (triangles) valleys (b) upon carrier accumulation. Empty symbols represent quantities obtained by means of ab-initio calculations performed using the fully relaxed DFT structure of monolayer MoS_2 whereas full symbols represent the same quantities obtained using the experimentally-reported structure. Panel (c): band structure of undoped MoS_2 close to the top of the valence bands (left) or to the bottom of the conduction bands (right) calculated using the experimentally-reported (continuous lines) or the DFT-relaxed (dashed lines) crystal structure. Note how the different structures very significantly change the distance in energy between the top of the K and Γ valleys in the valence band and between the bottom of the K and Q valley in the conduction band. As discussed in the main text, this distance in energy determines whether or not multiple valleys are occupied upon electron or hole accumulation in the calculations, with a corresponding strong effect on the shift of the A_{1g} phonon frequency.

that ΔE_{KQ} in the conduction band is sufficiently small, so that –at room temperature– both the K and Q valleys are populated in monolayers of all TMDs upon accumulation of $\sim 10^{-2}$ electrons per unit cell. Additionally, it is clear from figure 6.3a that phonon softening upon electron accumulation is much more pronounced in W-based TMD monolayers, indicating that ΔE_{KQ} is smaller for WS_2 and WSe_2 than for MoS_2 .

All these conclusions are fully consistent with what is known about monolayers of semiconducting TMDs. The energy difference $\Delta E_{\Gamma\mathrm{K}}$ reported in Tab. 2 from ARPES measurements is consistent with having only the K valley occupied upon accumulation of a density of holes reaching up to $\sim 5 \times 10^{13}$ cm^{-2} [206,213,214]. Similarly, although no sufficiently systematic ARPES study of the conduction band of monolayer TMDs has been reported yet, analogous measurements on the doped surface of bulk TMDs (where doping should be limited to the first few layers) have shown[215] that it is relatively easy to populate both the K and Q valleys in the conduction band (i.e., ΔE_{KQ} in monolayer TMDs is significantly smaller than $\Delta E_{\Gamma\mathrm{K}}$). Moreover, the observation of a larger softening in W-based monolayers, associated with the K and Q valleys being closer in $\mathrm{WS_2}$ and $\mathrm{WSe_2}$ than in $\mathrm{MoS_2}$, is compatible with the fact that ΔE_{KQ} is largely controlled by spin-orbit coupling (stronger in W-based compounds).

These considerations also make clear why the strong sensitivity of the phonon frequencies to the precise energy separation between valleys severely affects the ability of DFT to make reliable quantitative predictions. In particular, the spurious softening predicted on the hole side of $\mathrm{MoS_2}$ (see figure 6.6c) originates from the large underestimation of $\Delta E_{\Gamma\mathrm{K}}$ in DFT as compared to experiments (see Tab. 2), which leads to an erroneous occupation of both the K and Γ valleys even at very small doping concentrations at room temperature. Something similar, although not as severe, happens also for $\mathrm{WS_2}$, for which the DFT prediction for $\Delta E_{\Gamma\mathrm{K}}$ is not much smaller than the experimental results in Tab. 2, but it is still sufficient to lead to a spurious softening at large hole doping. Finally, the discrepancy with experiments might arise also from a partial failure of DFT in accounting for band-structure renormalization effects that influence the doping dependence of $\Delta E_{\Gamma\mathrm{K}}$ and ΔE_{KQ}.

6.4 Multivalley population mechanism of the electron-hole asymmetry

Finding that the strength of the coupling of electrons to phonons is drastically amplified when multiple inequivalent valleys in a given band are populated is a phenomenon that had not been identified in the past, and it is important to build a robust physical understanding. To this end, recall that electron-phonon coupling can be qualitatively understood by considering how the band structure is perturbed by the displacement pattern of the ions associated to the phonon under consideration[152,153,160]. Figure 6.8 shows the effect of the $\mathrm{A_{1g}}$ mode on the band structure of undoped monolayer $\mathrm{MoS_2}$ (for better clarity, spin-orbit coupling is not included; we checked that this has no qualitative consequences on the arguments here below). Although the amplitude (up to 0.12 Å) of the $\mathrm{A_{1g}}$ mode has been intentionally exaggerated with respect to typical room-temperature mean-square displacements to illustrate this effect, the large variation of both the valence and conduction bands signals the presence of a very strong electron-phonon coupling. This strength can be quantified by taking the first derivative of the band energy reported with respect to the atomic displacement, which is proportional to the bare electron-phonon coupling for that band (see the right panel of figure 6.8).

The introduction of free carriers –in our experiments by means of field-effect doping– allows for the possibility of electrostatic screening, and generically tends to decrease the strength of the electron-phonon coupling. In a simple Thomas-Fermi picture, whether or not the bare electron-phonon coupling is screened effectively by the free carriers depends on whether the evolution of the band induced by the phonon displacement pattern leads to a spatial variation of the density of charge carriers. In this regard, the situation can be very different depending on whether one or more valleys are populated.

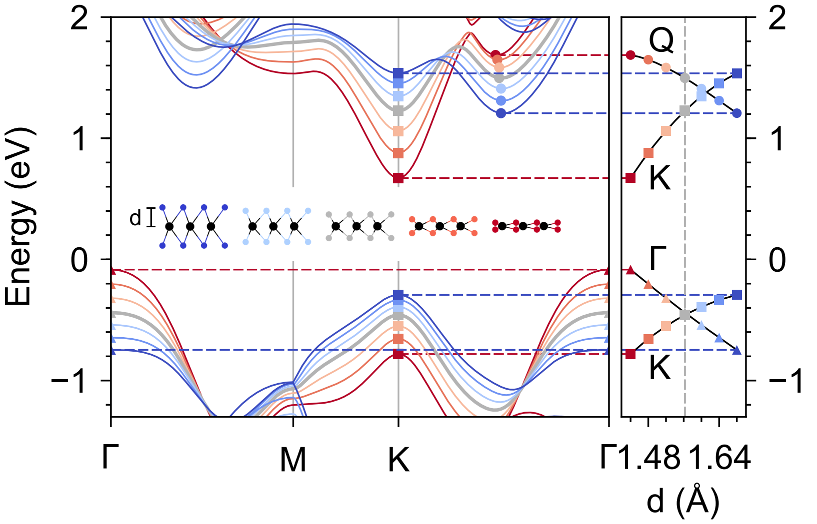

Figure 6.8: Variation of the first-principles energy bands of monolayer MoS_2 induced by the displacement pattern of the A_{1g} mode at Γ (a rigid vertical motion of the chalcogen planes in opposite directions, with a variation of the distance d between the plane of sulphur atoms and that of molybdenum atoms – see inset). To emphasize the effect, the amplitude of the displacement has been set to 0.12 Å, both in compression (red) and dilation (blue), with respect to the equilibrium value $d = 1.57$ Å (gray). On the right we report the evolution of the band edges of the K and Q valley in conduction and of the Γ and K valley in valence, as a function of d. The same colours as in the left panel have been used to identify different values of d. The absolute value of the slope of each curve at the equilibrium value of d (marked with a vertical dashed line) is proportional to the bare electron phonon coupling of the corresponding band with the A_{1g} mode at Γ.

To understand why, we consider a phonon near Γ ($\mathbf{q} \rightarrow 0$) as a frozen atomic displacement with very long, but finite, wavelength. The static displacement associated to such a phonon shifts the valleys up and down in energy locally in space, following the local amplitude of the long-wavelength A_{1g} mode. In the adiabatic limit, the population of the electronic states will change to keep the system in the lowest energy state. Now, if only a single valley is occupied (say the K valley in the conduction band), the only possibility for the free carriers is to follow the spatially varying position of the bottom of the valley to keep the Fermi level constant (or more appropriately the electrochemical potential, since we are considering the atomic displacement as frozen). This implies a spatial variation of the charge of the free carriers that self-consistently screens the potential of the lattice displacement, thereby strongly suppressing electron-phonon coupling.

When at least two valleys are occupied, the situation can be very different if the atomic displacements associated with the phonon mode lead to a relative out-of-phase energy shift. This is indeed so in monolayer TMDs for the Q and K valleys in the conduction band and for the K and Γ valley in the valence band (see figure 6.8). In this case, in the presence of the atomic displacement (and when electrons/holes have the time to relax their energy and momentum during the phonon perturbation, i.e. in the adiabatic limit) charge transfer between the valleys must also occur locally in real space for the system to stay in the ground state. Since part of the charge is now involved in this 'local' process, the charge that can be displaced to screen the spatially varying potential generated by the phonon is reduced, hindering the effectiveness of screening. In other words, in the presence of two valleys that shift out-of-phase in response to long-wavelength phonon excitations, screening becomes much less effective in reducing the strength of the electron-phonon coupling.

Within the controlled environment of our DFT calculations, we know that this is the mechanism responsible for the strong softening of the A_{1g} mode in all cases when two valleys are simultaneously occupied. We conclude that this mechanism also explains the Raman measurements. For this mechanism to have a strong effect, it is essential that the phonon mode considered causes an out-of-phase shift in the energy of the two valleys, because this maximizes the amount of inter-valley charge transfer that occurs locally in real space. For the E_{2g} mode detected in our Raman measurements on semiconducting TMDs, for instance, this is not the case: the long-range Fröhlich potential associated with the E_{2g} phonon near Γ shifts the energy of the two valleys in the same direction and by comparable amounts so that no (or minimal) inter-valley charge transfer occurs locally. As a result, despite the presence of multiple inequivalent valleys, the response of the system to E_{2g} phonons is similar to the canonical case with one single valley populated, with a strong electrostatic screening that suppresses the electron-phonon coupling.

It follows from these considerations that the underlying physical processes responsible for the enhancement of electron-phonon coupling in the presence of simultaneously populated inequivalent valleys is of quite general validity. As such, it is likely to occur in a multitude of materials and to have different experimental manifestations. It is quite remarkable that such a mechanism had not been identified earlier. We believe that this is because the analytic theoretical models commonly employed to treat electron-phonon interaction consider only one family of carriers (i.e., one single valley) coupled to phonons, and in these models the mechanism is simply not present.

Superconductivity provides an example of a physical phenomenon for which the enhanced electron-phonon coupling mechanism that we have identified may be at play. It appears that much of the existing data on gate-induced superconductivity observed in some of the TMDs (e.g., WS_2 and MoS_2) is consistent with having the superconducting instability setting in only when multiple valleys are occupied[172,216]. Having multiple valleys occupied would explain, for instance, why gate-induced superconductivity in WS_2 starts occurring at a lower electron density than in MoS_2 [170,171,182], because, as we discussed here above, the energy difference between the K and Q valley is smaller in WS_2 than in MoS_2 . It also explains why so far gate-induced superconductivity in semiconducting TMDs has been observed only upon electron accumulation and not with holes[170,180]: this is because with the hole concentrations that can be reached by field-effect doping only the K or Γ valleys are filled, so that the strength of the electron-phonon coupling remains weak. Indeed, in $NbSe_2$ –a metal having a similar valence band structure as WS_2 and MoS_2, but the Fermi level very deep relative to the top of the valence band[217,218]– robust superconductivity is observed[175–177] and both the K and the Γ valleys are occupied. The multi-valley mechanism responsible for the enhancement of the electron-phonon coupling is likely at play for other superconducting materials, with MgB_2 providing a notable example. Indeed, also in MgB_2 multiple inequivalent valleys are known to be simultaneously occupied and to move out-of-phase in energy when atoms are displaced according to a specific phonon pattern[219]. More work is needed to fully substantiate the relevance of multivalley population for the occurrence of superconductivity in all these systems, but the known experimental phenomenology does provide significant circumstantial evidence supporting such a scenario.

6.5 Conclusion

In conclusion, we have identified a strong and systematic electron-hole asymmetry in the vibrational properties of mono and bilayers of semiconducting TMDs, by performing Raman measurements on ionic-liquid-gated transistors. The experiments very systematically show that out-of-plane modes – such as the A_{1g} mode near zone center – soften significantly as the concentration of free electrons in the conduction band is increased, while they are left unaffected upon hole accumulation. By performing a theoretical analysis based on first-principles simulations, we have revealed that the phonon softening originates from a previously unidentified mechanism that amplifies pronouncedly the strength of electron-phonon coupling when two inequivalent valleys are simultaneously populated. This mechanism explains the asymmetry in phonon softening observed experimentally in the Raman spectroscopy measurements as due to a much larger energy separation between valleys in the valence bands as compared to the conduction band. As a result, in the range of carrier densities accessed in the experiments, simultaneous occupation of multiple valleys occurs only upon electron accumulation and not for holes.

It is surprising that this mechanism had not been identified earlier. This is most likely due to the fact that analytic theoretical models used in the discussion of electron-phonon interactions commonly treat the case of a single family of carriers (i.e., a single valley) that is coupled the lattice vibrations. It is nevertheless clear from our discussion that the microscopic processes responsible for the enhancement of electron-phonon interaction in multi-valley systems are physically robust. Hence, the same mechanism should be at play in many different material systems (i.e., not only in semiconducting transition metal dichalcogenides), and manifests itself in a variety of physical phenomena. This is likely the case, for example, of superconductivity. Existing experiments on transition metal dichalcogenides appear to indicate that the occurrence of superconductivity –either gate-induced in MoS_2 and WS_2, or intrinsically present in $NbSe_2$– correlates systematically with having multiple valley populated. Similar considerations can be made for other materials, with the case of MgB_2 being particularly notable. Although further evidence will be required, these examples underscore how the identification of a previously unappreciated mechanism enhancing the strength of electron-phonon interaction can have an important impact in the interpretation of many different phenomena observed experimentally.

Chapter 7: Semiconducting van der Waals interfaces as artificial semiconductors

7.1 Introduction

The absence of covalent bonds between the layers of van der Waals (vdW) materials is essential not only to allow the exfoliation of monolayers of excellent electronic quality from bulk crystals, but also to give an unprecedented flexibility in employing these monolayers to assemble new types of heterostructures[22,220,221]. It is because of the absence of covalent bonds that monolayers of different compounds can be stacked on top of each other without constraints imposed by the need to match their crystalline lattices or by chemistry compatibility. As a result, a very rich variety of building blocks – including semiconductors[38,110], semimetals[222], topological insulators[223], magnets[224,225], superconductors[12,226], and more – can be readily combined together to create artificial systems that were impossible to realize until now. That is why 2D materials offer a truly unprecedented potential to discover new physical phenomena or to engineer novel electronic functionalities. First examples are provided by the emergence of minibands and of satellite Dirac points in graphene-on-hBN[24–26], the possibility to induce strong spin-orbit interaction in systems of Dirac fermions in graphene-on-semiconducting transition metal dichalcogenides (TMDs)[227,228], or the occurrence of superconductivity in magic-angle graphene bilayers[27].

Despite the vast scope of possibilities enabled by vdW interfaces, a systematic microscopic understanding allowing the interfacial electronic properties to be predicted in terms of those of the constituent monolayers is missing. Developing such an understanding in general is difficult, because depending on the specific interface considered many different microscopic processes – hybridization of the electronic states in the two monolayers, relaxation of the crystalline structure, interaction effects[23], etc. – can play a prime role. To progress at this stage it is useful to focus our attention on an important class of systems for which we can exploit existing intuition, namely that of semiconducting monolayers forming an interface that also

---

The results presented in this chapter have been published as Evgeniy Ponomarev, Nicolas Ubrig, Ignacio Gutiérrez-Lezama, Helmuth Berger, and Alberto F. Morpurgo, *Nano Lett.*, ***2018***, *18* (8) behaves as a semiconductor, whose properties can be deterministically controlled by selecting the two constituent semiconductors in the vast palette of existing 2D materials.

At the simplest level, the strategy is to choose the constituent monolayers with an appropriate band alignment, so that the conduction band of the interface is inherited from one of the monolayers and the valence band from the other (as it happens in so-called type II semiconducting heterostructures)[229]. Under these conditions, many key interfacial semiconducting properties are distinct from those of the constituents, but uniquely determined by them. These include the size of the band gap (defined by the energetic alignment of the bands in the two monolayers), whether the gap is direct or indirect in $k-$space (determined by appropriately selecting the crystalline lattices of the materials forming the interface), the joint density of states governing absorption and radiative processes (directly linked to the properties of the bands in both constituent monolayers), and more. The interface is therefore a composite system that possesses unique semiconducting properties defined at the assembly stage by the choice of the constituent monolayers, which fully determine the low-energy optoelectronic response of the system detected experimentally. In other words, the interface truly behaves as an artificial semiconductor whose properties – that determine the optoelectronic response – are created by design.

Whereas over the last couple of years considerable experimental effort has focused on vdW interfaces of different semiconducting 2D materials[28,230,231], only a very limited amount of work has been done to probe transport and optical properties on a same structure, enabling a full understanding of the energetics of vdW interfaces. That is why developing the ability to probe the properties of vdW interfaces based on 2D semiconductors to determine quantitatively – directly from experiments – how these properties are related to those of the constituent 2D materials, is now a key priority. Here, we start addressing these issues by means of a systematic investigation of the transport and optoelectronic properties of two prototype vdW interfaces based on semiconducting TMD monolayers, namely $WSe_2/MoSe_2$[28] and WSe_2/MoS_2[232].

Transport investigations rely on ionic liquid gated field-effect transistors[73,75,233,234] realized on structures that enable the individual monolayers, and their interface, to be measured separately on a same device. By exploiting the spectroscopic capabilities of ionic liquid gating[76,77,79,235], these devices enable us to establish a direct relation between the bands of the vdW interface and those of the constituent monolayers, and to determine quantitatively and precisely the offsets between the bands of the different monolayers, as well as the magnitude of the interface band gap. To probe whether interband transitions in the vdW interface are direct or indirect in k-space we perform photoluminescence (PL) and photocurrent (PC) experiments. Radiative decay of interlayer excitons is observed in $WSe_2/MoSe_2$ but not in WSe_2/MoS_2, in agreement with the expectation that the interfacial interband transitions are direct in the first case and not in the second[70]. The binding energy of interlayer excitons in $WSe_2/MoSe_2$ can then be determined by directly comparing the frequency of the light detected in PL with the value of the interface band gap extracted from transport experiments, something that had never been done earlier. All together, the results presented here show that vdW interfaces behave as artificial semiconductors whose response – determined by the choice of the constituent materials – is virtually indistinguishable from that of a naturally existing 2D semiconducting material.

7.2 Band alignment in vdW heterostructures

The device configuration employed for our transport measurements – essential to obtain the results discussed below – is illustrated in figure 7.1 for the MoS_2/WSe_2 system. The MoS_2 and WSe_2 monolayers are exfoliated onto a Si/SiO_2 substrate (see Figure 1a and 1b). Using a by-now conventional "pick-up" technique based on polymer stamps[236], the WSe_2 monolayer is transferred onto the MoS_2 monolayer with the aid of a motorized manipulator stage under an optical microscope. Figures 7.1c and 7.1d show microscope images taken after the transfer and after having attached contacts. The final step is the application of the top ionic liquid, leading to a device structure such as the one represented schematically in figure 7.1e (with the gate and reference electrodes also shown). The important aspect of this device geometry is that the different parts of the structure can be measured independently in a field-effect transistor configuration, while being directly connected to each other. This is key as it allows a direct quantitative comparison of relevant quantities measured in the different parts of the device.

Figure 7.2a shows the source-drain current (I_{SD}) measured on the different parts of a device based on WSe_2 and $MoSe_2$ monolayers, as a function of gate voltage V_G ($V_{SD} = 50$ mV; see the schematics on top). The left, center, and right panels (blue, red, and green curves) show the current flowing through the WSe_2 monolayer, the $WSe_2/MoSe_2$ interface, and the $MoSe_2$ monolayer, respectively. Excellent ambipolar characteristics are observed in all cases, demonstrating that for the monolayers, as well as for the interface, sweeping V_G allows shifting the chemical potential from the conduction to valence band. As discussed earlier in multiple occasions[76,77,79,235], when the current is plotted as a function of reference potential V_{ref}, these measurements provide spectroscopic information. That is because, due to the very large capacitance of the ionic liquid, a change in V_{ref} corresponds to a shift in chemical potential $\Delta\mu = eV_{ref}$ as long as the density of states in the system is small (which is the case if the chemical potential is shifted inside the gap of a semiconductor)[76].

The current I_{SD} measured on the different parts of the structure plotted as a function of V_{ref} is shown in figure 7.2b. The current through the vdW interface – the continuous red curve – quite precisely overlaps with the dashed green curve (*i.e.,* the current flowing through the $MoSe_2$ monolayer) when the conduction band of the interface is populated, and with the blue dashed curve (i.e., the current flowing through the WSe_2 monolayer) when the valence band is populated. It follows from this ob-

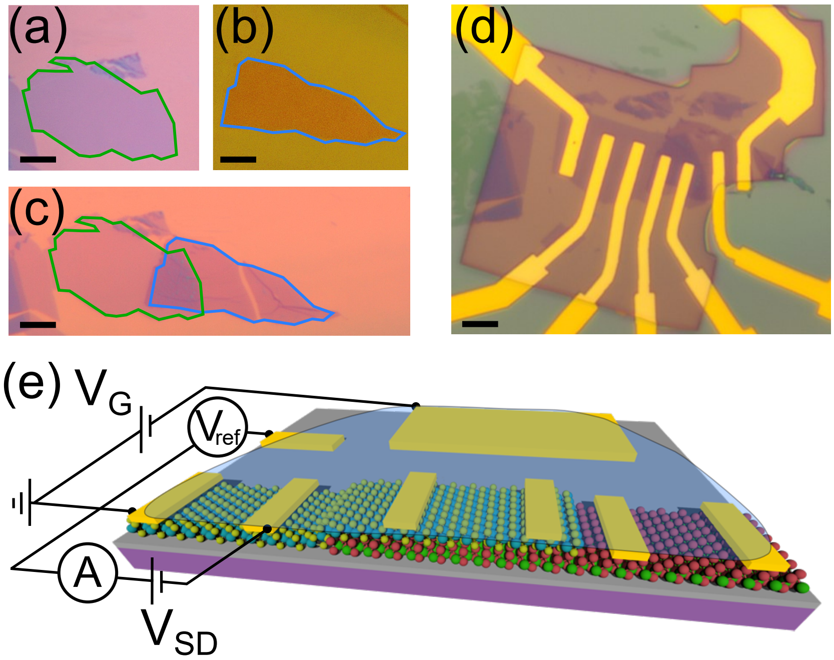

Figure 7.1: Device structure enabling the quantitative characterization of van der Waals interface and of their constituent monolayers. Optical microscope images of a MoS_2 (a), a WSe_2 (b) monolayer (delimited respectively by the green and the blue lines), and of the structure assembled by transferring the WSe_2 monolayer to overlap partly with the MoS_2 one. (d) Optical microscope image of a device based on the structure shown in (c) with Pt/Au contacts enabling separate transport measurements to be done on the three regions (MoS_2 monolayer, WSe_2 monolayer and their interface). The scale bars in all images are 5 μm. (e) Schematics of an ionic-liquid gated FET based on a device structure comprising two monolayers and their interface, such as the one shown in (d). The schematics also shows – not to scale – the gate and the reference electrode, as well as the typical bias/measurement configuration needed to perform the transistor electrical characterization.

servation that the interface conduction and valence bands are respectively the conduction band of the $MoSe_2$ monolayer and the band of the WSe_2 monolayer. This shows directly how the bands of the vdW interface – and therefore all other low energy properties – are fully determined by the choice of the individual constituents. Finding that the overlap is virtually perfect indicates the absence of an energetic shift between the bands of the interface and the corresponding bands of the constituent 2D materials (or of any other significant modifications of bands in the interface region), in agreement with the expected absence of any significant interfacial dipole between the layers forming the vdW interface.

To make these considerations systematic and quantitative, we compare the values of threshold voltage for electron and hole conduction (V_{th}^h and V_{th}^e), for the different parts of the device. At threshold, the chemical po-

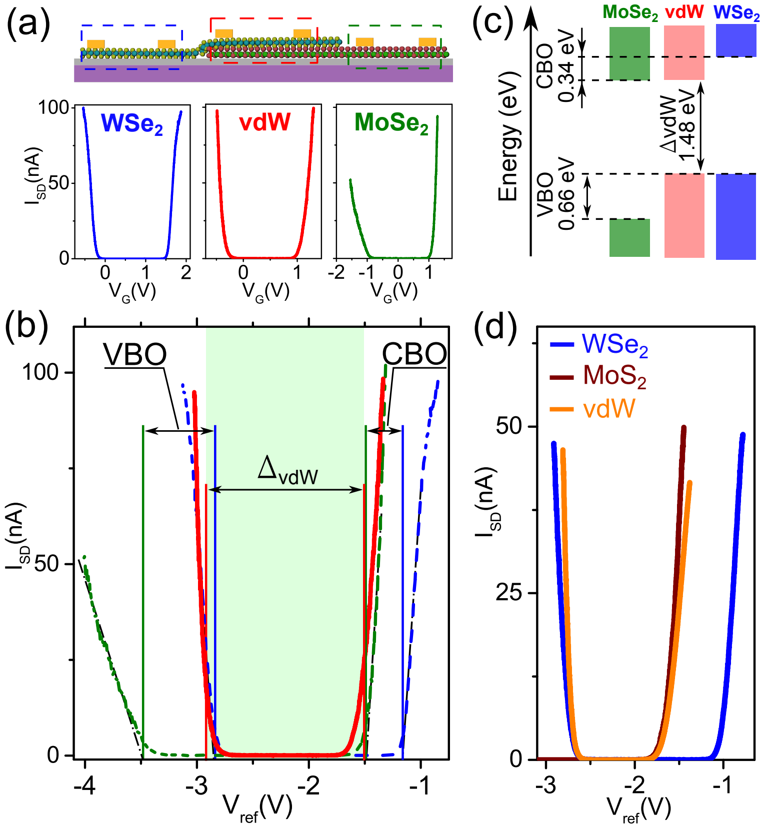

Figure 7.2: Spectroscopic characterization of a vdW interface and its constituents by transport measurements in ionic liquid gated devices. (a) Top panel: Schematic representation of device configuration, showing the three different parts measured (left: WSe$_2$ monolayer; center: vdW interface; right: MoSe$_2$ monolayer). Bottom panels: FET transfer curves (i.e., I_{SD} as a function of V_G at fixed V_{SD}) for the monolayers and the interface (see legends), all exhibiting perfectly balanced ambipolar transport. (b) Same curves shown in (a) plotted versus reference potential V_{ref} (curves of a same color in (a) and (b) represent measurements done on the same part of the structure). The current through the interface (red curve) matches the current through MoSe$_2$ (green curve) when the chemical potential is in the conduction band and the current through WSe$_2$ (blue curve) when the chemical potential is in the valence band. The black dash-dotted lines represent the linear extrapolations done to determine the electron/hole threshold voltages for each curve, from which we obtain the corresponding conduction and valence band offsets (CBO and VBO, respectively), as well as the vdW interface band gap (Δ_{vdW}). (c) shows the resulting band diagram corresponding to a type II (staggered) alignment[4] of the MoSe$_2$ and WSe$_2$ bands. (d) shows similar curves and an identical phenomenology for the WSe$_2$/MoS$_2$ system. In MoS$_2$ monolayers hole transport is suppressed by in-gap states originating from S vacancies[235], and yet the interface exhibits excellent hole transport, because the interfacial valence band originates from WSe$_2$.

tential is located right at the edge of the corresponding band[4], i.e., at the bottom of the conduction band at threshold for electron transport and at the top of the valence band at threshold for hole transport. Therefore, since a shift in reference potential corresponds to an equal shift in chemical potential, the difference of measured threshold voltages provides a measurement of the energetic position of the bands in the different parts of the device. Specifically, the difference between V_{th}^e and V_{th}^h corresponds to the band gap in the part of the device on which the measurements are done; the difference between the values of V_{th}^e (V_{th}^h) measured on two different parts of the devices gives the offset of their conduction (valence) bands.

The threshold voltages V_{th}^h and V_{th}^e are determined by extrapolating to zero the source-drain current I_{SD} measured as a function of V_{ref} (the experimental error depends on the specific device, and is typically less than 5 % (It is this error that is responsible for the experimental uncertainty in the position of the bands, and hence for the band offsets and the band gap extracted from the measurements. What is most strongly affected from this uncertainty are the intra-and interlayer exciton binding energies, which are are small quantities, obtained from the difference of much larger values (that is why the relative error on the extracted exciton binding energy is large).)). We first check the values of the band gap for the $MoSe_2$ and WSe_2 monolayers, and find $\Delta(MoSe_2) = e(V_{th}^e(MoSe_2) - V_{th}^h(MoSe_2)\ ) = 2.06$ eV and $\Delta(WSe_2) = e(V_{th}^e(WSe_2) - V_{th}^h(WSe_2)\ ) = 1.73$ eV, in good agreement with values reported in the literature[206,237,238]. For the $WSe_2/MoSe_2$ interface the band gap is found to be $\Delta(WSe_2/MoSe_2) = e(V_{th}^e(WSe_2/MoSe_2)$ $- V_{th}^h(WSe_2/MoSe_2)\ ) = 1.48$ eV and the same procedure to determine the conduction band offset (CBO) and valence band offset (VBO) between the $MoSe_2$ and the WSe_2 monolayers gives $E_{CBO}(WSe_2/MoSe_2) = 0.34$ eV and E_{VBO} $(WSe_2/MoSe_2) = 0.66$ eV. Figure 7.2c summarizes these values in a single band diagram. The same analysis performed on the WSe_2/MoS_2 system (see figure 7.2d) gives a value of the interface band gap of Δ_{WSe_2/MoS_2} $= 1.08$ eV, comparable to what found in recent scanning tunnelling spectroscopy experiments[239]. For this interface we could only determine the conduction band offset between the two monolayers, $E_{CBO}(WSe_2/MoS_2)$ $= 0.63$ eV, because – as we recently discussed in Ref. 235 – in monolayer MoS_2 the presence of defects states near the top of the valence band prevents good quality hole conduction. In this regard, it is worth emphasizing how remarkable it is that the interface exhibits ideal ambipolar behavior, even though hole transport is drastically suppressed in one of the constituent monolayers.

To finalize our discussion of transport, we complete the analysis of the characteristics of FETs realized on the different vdW interfaces. Representative output curves, *i.e.,* the source-drain current I_{SD} as a function of source-drain voltage V_{SD} for different values of gate voltage V_G, are shown in figure 7.3a for a WSe_2/MoS_2 interface. Except for a small hysteresis,

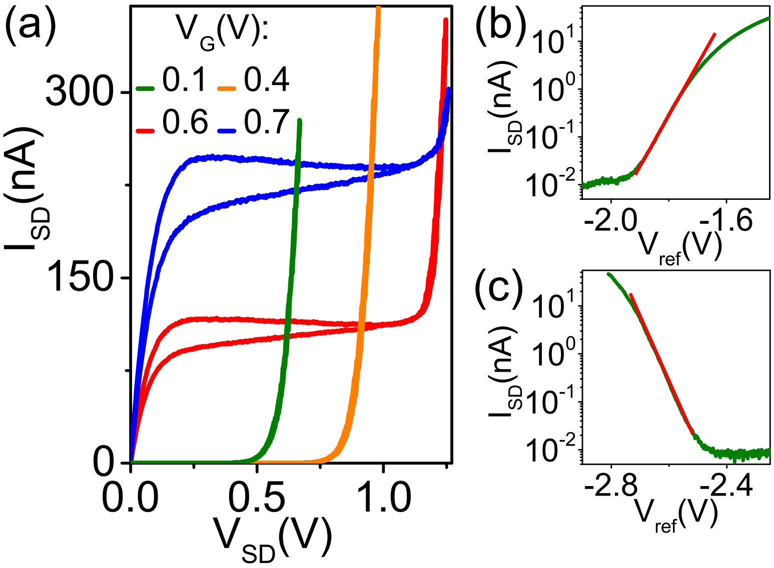

Figure 7.3: Electrical characteristics of a WSe_2/MoS_2 interface FET. (a) Source-drain current I_{SD} as a function of source-drain bias V_{SD} for different V_G values (FET output curves) showing the behavior characteristically observed in devices based on high quality individual semiconducting monolayers. (b,c) FET transfer curves in semi-logarithmic scale in proximity of the electron (b) and hole (c) threshold. The red lines represent the linear regressions made to estimate the subthreshold swing S.

the output curves exhibit a virtually ideal behavior: the linear regime is observed at low V_{SD}, followed at larger positive V_{SD} by a well-defined saturation regime, and by a steep increase in I_{SD} if the source-drain bias is increased further to enter the ambipolar injection regime (*i.e.,* when electrons and holes are injected at opposite contacts)[72]. We also determined the subthreshold swing by looking at the semi-logarithmic plot of the transfer curves, and found $S = 98$ mV/dec and $S = 74$ mV/dec for electron and hole transport, respectively (see figures 7.3b and 7.3c). Both these values are very close to the ultimate room-temperature limit of 66 mV/dec[4]. Together with the ideal ambipolar behavior shown in figure 7.2, these measurements demonstrate that the quality of FETs realized on vdW interfaces is comparable in all regards to that of FETs realized on individual TMD monolayers.

7.3 Optoelectronic properties of vdW interfaces

Next we discuss the optoelectronic properties of the vdW interfaces, starting with PL measurements performed on the $WSe_2/MoSe_2$ system. The room-temperature interface PL spectrum is shown in figure 7.4a (solid red curve). It consists of two main peaks centered around 1.36 eV and 1.6 eV, with the latter exhibiting a shoulder around 1.55 eV (see figure 7.4b). A comparison with the spectra of the $MoSe_2$ (green curve in figure 7.4a) and WSe_2 (blue curve in figure 7.4a) monolayers shows that the 1.55 eV shoulder originates from the recombination of intralayer exctions in $MoSe_2$. The 1.6 eV peak is due to the recombination of charged excitons – i.e., trions – in WSe_2 all in agreement with values reported in the literature[47,240] . Trion formation is responsible for the red shift measured in the vdW interface as compared to the energy of the PL measured in the WSe_2 monolayer part of the same device, which is due to neutral excitons. In the interface region, trions form because a small amount of thermally activated charge is transferred between $MoSe_2$ and WSe_2; indeed the red-shift disappears at low temperature, as we show below for the case of the WSe_2/MoS_2 where the same phenomenon occurs. In short: the 1.55 eV shoulder and the 1.6 eV peak are well accounted for by intralayer transition, consistently with the fact that their energy is larger that the band gap of the $WSe_2/MoSe_2$.

Contrary to these features, the 1.36 eV peak in the interface PL spectrum shown in figure 7.4a is obviously absent in the spectra of either constituent monolayer. This peak is a manifestation of interlayer excitons formed by electrons and holes located in different layers – a hole in WSe_2 and an electron in $MoSe_2$ in the present case – with the corresponding transition represented by the diagonal red arrow in the inset of figure 7.4a[28,69,241]. Consistently with this attribution, the energy of the transition is smaller than the single particle interface band gap, $\Delta(WSe_2/MoSe_2) = 1.48$ eV, as extracted from transport. With the experiments giving us both the interfacial band gap and the interfacial exciton recombination energy E_{PL}, the binding energy of the interfacial exciton (X_i^0) can be determined to be $E_{X_i^0}(WSe_2/MoSe_2) = \Delta(WSe_2/MoSe_2) - E_{PL} = 120$ meV. Despite any possible reduction due to the enhanced screening caused by the presence of the ionic liquid, this is a rather large value, as expected from recent estimates[15]. Importantly, finding that the interfacial exciton (X_i^0) decays through a radiative transition strongly supports the conclusion that the band gap of the $WSe_2/MoSe_2$ interface is direct in $k-$space[70] . That is because the constituent monolayers are nearly perfectly lattice matched and their crystallographic orientations have been intentionally aligned during the device fabrication.

Following the same logic[70] , no PL from interlayer excitons is expected in WSe_2/MoS_2 interfaces irrespective of the alignment of the crystallographic axis of the constituent monolayers, because of a 5 % mismatch in their lattice constants. The mismatch implies that the K/K' points of the WSe_2 and MoS_2 monolayers are located at different points in

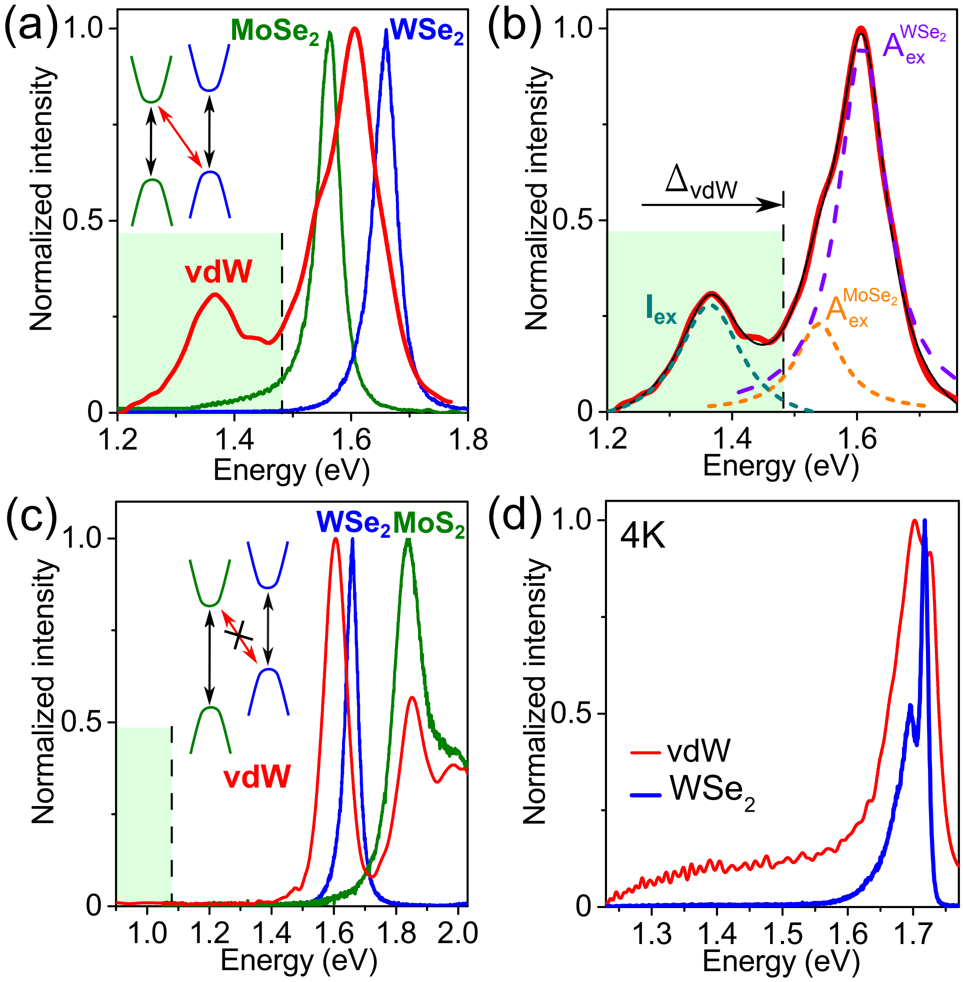

Figure 7.4: Photoluminescence of vdW interfaces and their constituent monolayers. (a) Normalized room-temperature PL spectra of WSe$_2$ (blue curve) and MoSe$_2$ (green curve) monolayers and of their interface (red curve). The peaks at 1.55 eV in MoSe$_2$ and at 1.65 eV in WSe$_2$ originate from intralayer A-exciton recombination. The interface spectrum exhibits an additional peak at 1.36 eV due the recombination of interlayer excitons, formed by electrons in MoSe$_2$ and holes in WSe$_2$. The light-green shaded area represents the interval of energy inside the interface band gap $\Delta(WSe_2/MoSe_2)$, extracted from transport experiments. The inset represents the alignment of the band, and the arrows indicate the optical transitions detected in the PL spectra. (b) Decomposition of WSe$_2$/MoSe$_2$ interface PL spectrum seen in (a) as a sum of the three identified radiative transitions (the formation of trions in the interface region is responsible for the red-shift of the PL peak due WSe$_2$ intralayer exciton recombination; see main text). (c) Same as (a) for the WSe$_2$/MoS$_2$ system. The blue, green and red curves represent the PL of the individual WSe$_2$ and MoS$_2$ monolayers, and of the interface, respectively. No sign of a radiative interlayer transition is seen in this case. Also here, the WSe$_2$ PL peak is red-shifted in the interface region due to the formation of trions, but at $T = 4.2$ K the red-shift disappears, as shown by the PL spectra plotted in (d).

$k-$space, preventing direct interlayer transitions[232]. The PL spectra for the WSe_2/MoS_2 system is shown in figure 7.4c, for a device in which the crystallographic axis of the monolayers have been carefully aligned. The PL from the interface (red line) exhibits two peaks, at 1.59 eV and at 1.84 eV. The latter coincides with the peak originating from direct intralayer exciton transitions in MoS_2, as it can be inferred from the PL spectrum measured on the MoS_2 monolayer (green line in figure 7.4c). Similarly to the case of the $WSe_2/MoSe_2$ interface, the 1.59 eV peak is due to intralayer trion recombination in WSe_2, and is red-shifted relative to the recombination of neutral excitons in the isolated WSe_2 (blue line in figure 7.4c). Here as well, trions in WSe_2 are formed in the interface region due to a small density of thermally activated charge carriers transferred from MoS_2. Indeed, when the PL spectrum of the interface and of WSe_2 are measured at $T = 4.2$ K – with thermal transfer of carriers fully suppressed – the shift disappears and the position of the peak measured in the isolated WSe_2 monolayer coincides with the position of the peak measured in the WSe_2 forming the interface (see figure 7.4d; the only difference is that the peak of the isolated monolayer is sharper).

The most relevant aspect of these measurements is the absence of any features at energy smaller than those originating from intralayer transitions in the individual monolayers. As the single particle band gap extracted earlier from transport experiments is $\Delta(WSe_2/MoS_2) = 1.08$ eV, any possible interlayer transition should be visible below this energy. However, no signal is observed here even though our spectrometer is sensitive down to 0.8 eV. Several devices with different rotational alignment were studied with no significant difference in their PL response: in no case a peak with energy smaller than 1.08 eV was observed. The experimental results therefore fully support the conclusion that the band gap of the WSe_2/MoS_2 interface is indirect in $k-$space.

More information about the interface interband transitions can be obtained from photocurrent spectroscopy[69,242]. Whereas the outcome of PL experiments strongly depends on the competition between radiative and non-radiative decay processes, PC spectroscopy reveals details of optical interband transitions in a way similar to optical absorption measurements[243,244]. Figure 7.5a,b show the short-circuit current I_{SC} –*i.e.*, the PC measured with short-circuited contacts – for the $WSe_2/MoSe_2$ and the WSe_2/MoS_2 interfaces, as function of laser excitation energy. We discuss exclusively the spectral dependence of the PC, and not on its absolute magnitude, which critically depends on details of the experiments (the de-

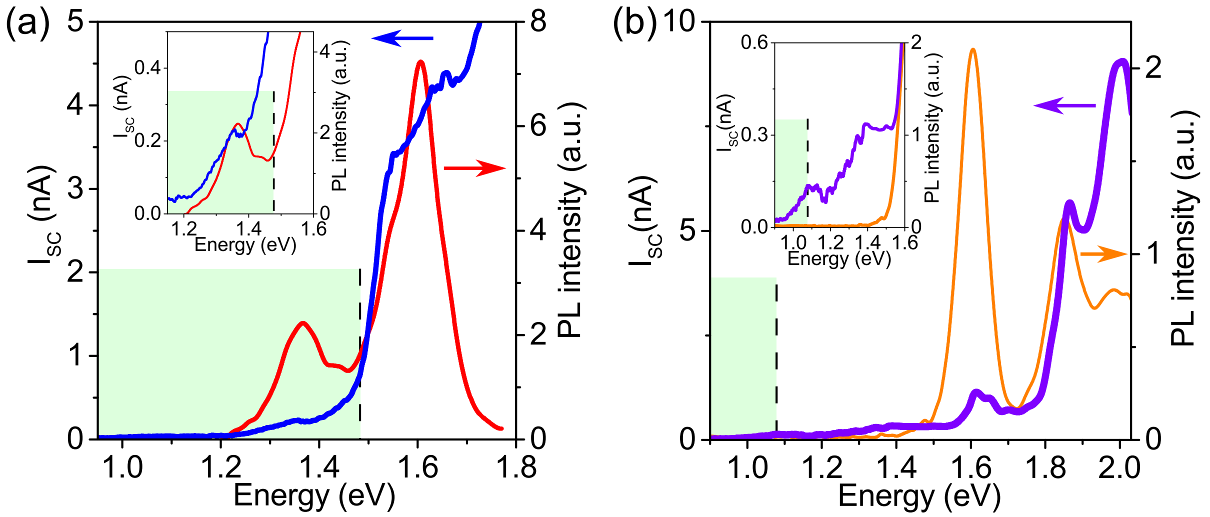

Figure 7.5: Photocurrent spectroscopy. (a) The short-circuit current, I_{SC}, measured on a $WSe_2/MoSe_2$ interface as function of incident photon energy (blue line) is compared to the interface PL spectrum (red line). The light-green shaded region marks the energy interval below the interface band gap, as extracted from transport measurements. The inset zooms-in on the two curves at low energy. It is apparent that the PC onset occurs in correspondence of the interlayer exciton transition and that a steep increase in I_{SC} occurs just below 1.5 eV, *i.e.,* in correspondence of interfacial interband transitions (the interface band gap is $\Delta(WSe_2/MoSe_2)$=1.48 eV). (b) PC spectrum measured on the WSe_2/MoS_2 interface (blue curve) together with the corresponding PL spectrum (orange curve). The inset zooms-in on the photocurrent at energy smaller than the intralayer transitions, showing that a slowly increasing photocurrent is present, starting from approximately 1 eV, close to the interface band gap $\Delta(WSe_2/MoS_2)$=1.08 eV. The slow increase is consistent with the indirect nature of the interlayer transitions.

vice geometry, the applied gate voltage, the spatial profile of the incident light, etc.; see section 7.5.1).

As it is apparent from a direct comparison with the PL spectra (see figures 7.5a,b and their insets), both interfaces exhibit a measurable PC starting at energies well below the energy of the excitonic transition in the constituent monolayers. For the $WSe_2/MoSe_2$ interface, the PC becomes measurable near the onset of the PL line associated to the interlayer exciton radiative decay (exhibiting a shallow maximum near the PL peak, see the inset of figure 7.5a). It then starts to increase steeply in correspondence of the vdW interface gap $\Delta(WSe_2/MoSe_2) = 1.48$ eV. This behavior is expected, since interlayer transitions in the $WSe_2/MoSe_2$ interface are direct in $k-$space. For the WSe_2/MoS_2 interface the PC onset is just under 1.08 eV (Figure 7.5b and its inset), and the PC increases only slowly as the energy is increased up to approximately 1.6 eV, at which point a steeper enhancement is observed due to direct intralayer exciton absorption in WSe_2. Finding that the PC onset energy matches the value of band gap is interesting, since the PL of the WSe_2/MoS_2 interface did not show any feature at $\Delta(WSe_2/MoS_2) = 1.08$ eV. Overall the expected behavior, and in particular the slow increase in PC at energies smaller than the intralayer transitions, is consistent with the interfacial band gap of WSe_2/MoS_2 being indirect in $k-$space. For both interfaces, therefore, the PC measurements fully support the conclusions drawn from transport and from PL measurements.

7.4 Conclusion

In summary, our work demonstrates an approach to characterize systematically the basic properties of semiconducting van der Waals interfaces, enabling a quantitative relation with the corresponding properties of the constituent 2D materials to be established. More specifically, our experiments show directly how the interfacial conduction and valence bands are independently determined by the conduction and valence bands of the constituent monolayers, they allow the full quantitative determination of the energetics of the system (including the single-particle band gaps of the two materials and of the interface, the values of the band offsets, and the exciton binding energies), and provide definite information about the direct/indirect nature of inter-band transitions. These conclusions have been obtained for two specific interfaces, but the experimental method that we have demonstrated can be applied to any other system of the type discussed here. Even more important in the broader context, the experiments show that the opto-electronic response of semiconducting vdW interfaces – including transport in transistor devices, photoluminescence, photocurrent, etc. – is virtually indistinguishable from that of an individual semiconducting monolayer. Nevertheless, there is clearly a very important difference between the two cases, namely that the material properties of an individual monolayer are given and cannot be modified, whereas the properties of interfaces can be deterministically defined by appropriately selecting the constituent monolayers in the vast portfolio of existing semiconducting 2D materials. As such, vdW interfaces are composite systems that behave in all regards as artificial semiconductors with properties that can be engineered by design at the assembly stage.

7.5 Appendix

7.5.1 Scanning photocurrent microscopy

In the main text we have discussed the spectral dependence of the photocurrent measured in our devices, and not the magnitude that – as we mentioned – depends on many experimental details of the structure and of the conditions under which the measurements are done. To illustrate this last point, here in figure 7.6b we show a map of the short-circuit current I_{SC} (i.e., of the photocurrent) obtained by scanning the laser spot over the surface of a representative WSe_2/MoS_2 device (whose optical microscope image is shown in figure 7.6a). The magnitude of the photocurrent depends on the position of the illumination spot and reverts its sign as the illumination spot is displaced from one contact to the other. That is the behavior expected in this measurement configuration, because the net photocurrent is determined from the imbalance of photoexcited carriers that exit the device at the two contacts (for a discussion see, for instance, Ref. 81). This map clearly shows that the magnitude of the photocurrent depends on the way the device is illuminated (it would also depend on many other parameters, such as, for instance, the gate voltage). The spectral dependence of I_{SC}, however, is the same irrespective of these details, as we verified by measuring it at different positions of the illumination spot.

To exclude any possible effect of the contacts on I_{SC} we also probe the photocurrent response of interface FETs in the presence of a p-n junction formed inside the channel away from the contacts. In ionic-liquid gated FET a lateral p-n junction can be defined and controlled electrostatically upon driving the transistor into the ambipolar injection regime (*i.e.,* the regime in which both types of charge carriers are simultaneously present in the FET channel, see figure 7.3a (main text) for $V_G = 0.6$ V) as has been demonstrated for multiple occasions[77,138]. Once the p-n junction is created and its position is defined by the appropriate bias conditions, the device is cooled down to T = 77 K, below the freezing point of the liquid, which immobilizes the ions in such a way that the p-n junction is also "frozen" in the transistor channel. Figure 7.6c shows the I_{SD} vs V_{SD} curve measured after cool down, with the rectifying behavior confirming the presence of the p-n junction. The presence of the p-n junction is also demonstrated by the photocurrent map (figure 7.6d). Indeed the photocurrent is observed to peak in the center of the channel where the p-n junction is, and not anymore at the contact (as shown in figure 7.6b for the unbiased device). We have checked that the photocurrent spectra acquired from the p-n junction region coincide with the ones observed when the contacts are illuminated,

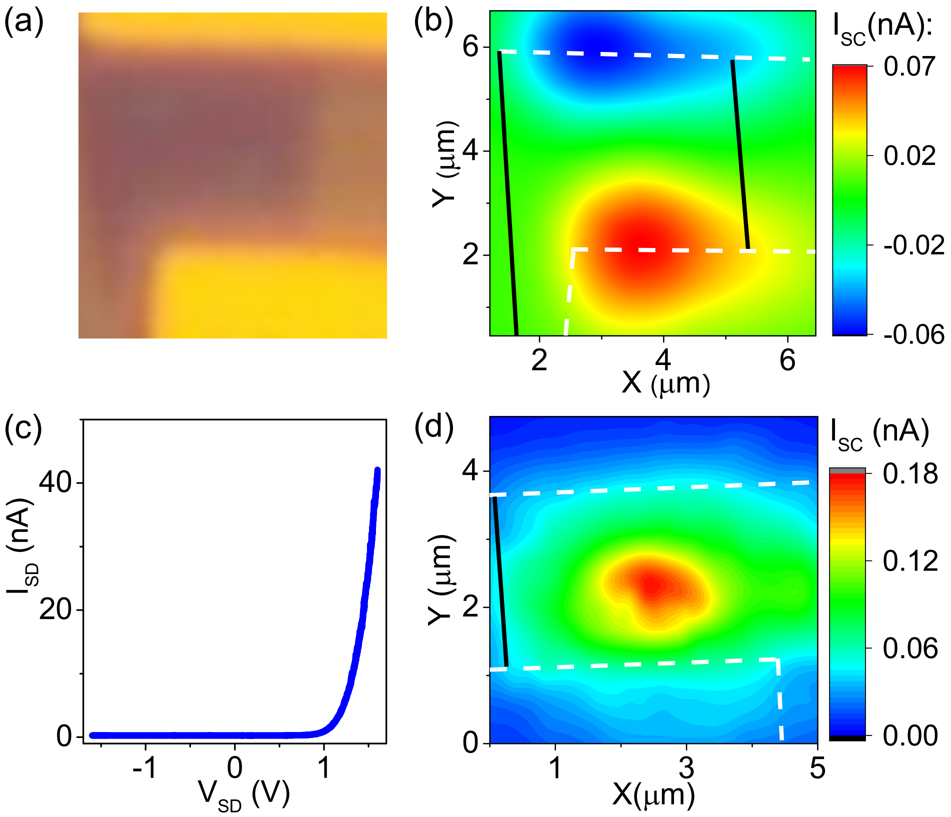

Figure 7.6: (a) Optical microscope image of the sample area from which the PC map shown in panel (b) was collected. (b) Photocurrent map (*i.e.,* I_{SC} as a function of illumination position) measured on a WSe_2/MoS_2 interface transistor upon illumination with a 1125 nm (1.1 eV) excitation wavelength. The edges of the metal contacts and of the WSe_2/MoS_2 interface are indicated with the white dashed and solid black lines respectively. (c) Source-drain current I_{SD} as a function of source-drain voltage V_{SD} acquired after driving the FET into ambipolar injection regime at room temperature and cooling it down to T = 77K. Rectification of the I_{SD} indicates the formation of the p-n junction. (d) Photocurrent map measured on a $WSe_2/MoSe_2$ interface transistor in the presence of a p-n junction formed by cooling down the ionic liquid to T = 77K upon illumination with a 750 nm (1.65 eV) excitation wavelength.

indicating that the photocurrent probes the interface properties and is not influenced by contact effects.

Chapter 8: A universal approach for bright interlayer excitons in van-der-Waals interfaces

8.1 Introduction

Heterostructures of two-dimensional (2D) semiconductors – distinct atomically thin layers held together by *van der Waals* interactions – have shown that it is possible to host and engineer radiative recombination of interlayer excitons (X_0^I)[28,29,69,71]. These excitons, consisting of a bound state between electrons and holes residing in the conduction and the valence bands of different constituents of a heterostructure (see figure 8.1a for an illustrative scheme), have high binding energies and large tunable lifetimes rendering them attractive both for studying coherent quantum states[19] and for the development of excitonic devices[67,68] . Furthermore, the possibility to rotationally align the lattices of the constituent 2D layers introduces a new degree of freedom, which has lead to the discovery of a new type of interlayer excitons, the so-called *moiré excitons*[245–248]. All these remarkable phenomena, however, can be exploited solely if an interlayer exciton recombines radiatively –*i.e.,* is optically bright– which is achieved only when the conduction band minimum (CBM) of one heterostructure component coincides in momentum space with the valence band maximum (VBM) of the other, as illustrated in figure 8.1c. This stringent constraint substantially reduces the number of materials that can be combined to yield radiative interlayer exciton recombination[70,71], in particular given the fact that most of the 2D semiconductors used hitherto have their band edges in the corner of the first Brillouin zone. As illustrated in figures 8.1(e)-(f), in such a case the relative positions of the distinct band edges become very sensitive to lattice mismatch and rotational alignment between the 2D layers. Thus, the experimental observation of interlayer excitons in vdW heterostructures has been reduced so far to very few combinations between layered semiconductors throughout the available possibilities in the immense family of 2D materials.

The results presented in this chapter are currently in preparation for submission, Nicolas Ubrig, Evgeniy Ponomarev, Daniil Domaretskiy, Takashi Taniguchi, Kenji Watanabe, and Alberto F. Morpurgo

However, these strict limitations, linked to the rotational alignment and lattice mismatch between the layers, can be naturally lifted by selecting constituents with respective band extrema in the center of the first Brillouin zone (*i.e.,* where k=0) – at the Γ point. In such a situation CBM and VBM are always superimposed in momentum space no matter the shape, the size, or the alignment of the first Brillouin zones of the constituents (figure 8.1d). Hence, an interlayer exciton formed out of carriers residing in these bands (which we refer to as Γ-Γ exciton in the following for simplicity) has to recombine radiatively, as long as the optical selection rules are respected. Due to the *van der Waals* interaction which holds together the layers, a 2D vdW heterostructure allows to combine compounds with very different structural properties and rotational symmetries. This feature is in clear contrast with what could be done so far with conventional semiconductors[13] and provides the opportunity for unprecedented combination of materials. For instance, all multilayered group VI TMDs have the VBM at the gamma point and can therefore be used as a constituent layer for hosting holes. Among potential candidates which are predicted to align with TMDs and have the CBM located at the Γ point are few layers of InSe[249,250].

Here we report on optical transitions at the Γ-point as robust method for the observation of radiative recombination of interlayer excitons in atomically thin vdW heterostructures. In all presented combinations we observe photoluminescence originating from the recombination process of interlayer excitons formed out of carriers residing at the Γ-point. These experimental findings assert that our approach allows to combine a large number of materials irrespective of their lattice parameter and their rotational alignment in order to yield bright interlayer recombination. We further demonstrate that upon freely interchanging the compounds the emission energy of the exciton can be tuned over a wide spectral range from the visible to the near-infrared. The systematic variation of the constituents and their thickness allows us to identify the relative band positions between the constituents. The resulting band alignment elucidates the main mechanisms of the charge transfer in these heterointerfaces.

8.2 Bright interlayer $\Gamma - \Gamma$ excitons

We first evidence the existence of Γ-Γ excitons in a prototype heterostructure composed of bilayers of WS_2 and InSe, representative of the behavior we observe systematically in all other heterostructures we present here. To

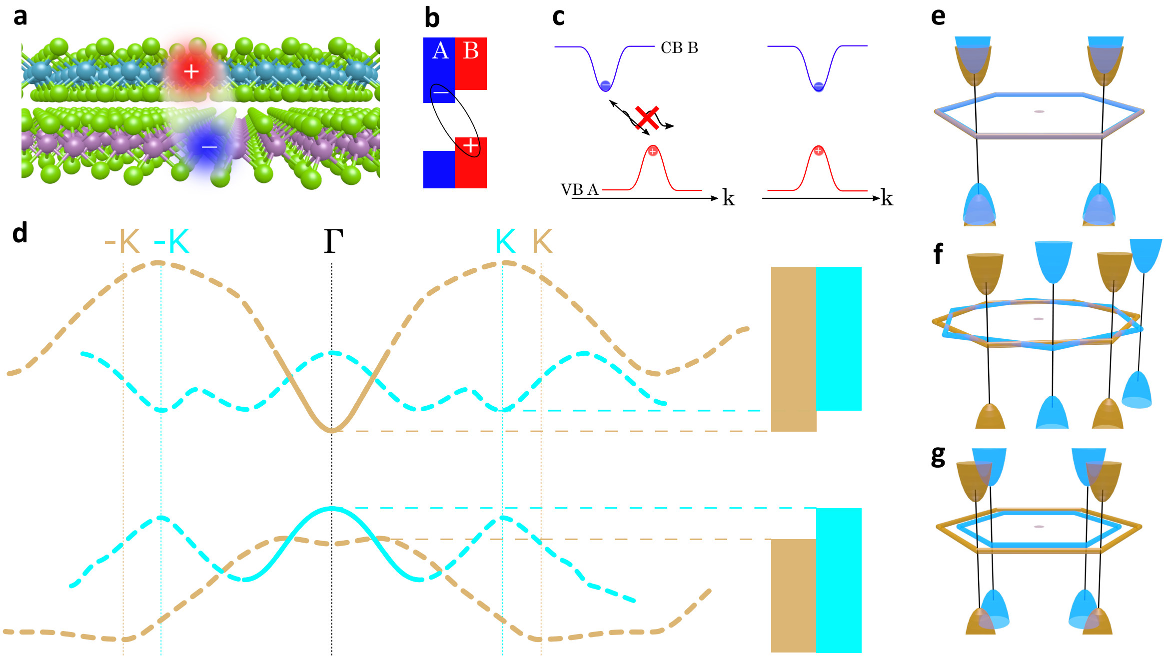

Figure 8.1: (a) Schematic real space representation of an interlayer exciton. (b) Interlayer exciton in type II semiconducting heterostructures. (c) Aligned (right panel) and misaligned (left panel) in the momentum space conduction band minimum and valence band maximum in type II heterostructures. (d) Schematic representation of band structure of InSe bilayer/WS_2 bilayer heterostructure. (e)-(g) Alignment of the first Brillouin zones of heterostructure constituents with CBM and VBM situated at the Brillouin zone corners (the K/-K point). (e) and (f) depict the situation when the heterostructure components have the same lattice parameters and are rotationally aligned (e) and misaligned (f). (g) represents the case when the constituents have different lattice parameters. Only for the alignment shown in (e) CBM and VBM of heterostructure overlap in the momentum space enabling radiative recombination of interlayer excitons.

avoid degradation of the constituents, the heterointerface is assembled by complete encapsulation between thin layers of h-BN. Our samples contains three distinct regions – the interface and the corresponding individual constituents as depicted by a representative specimen in figure 8.2a – which enables each area to be measured and characterized separately. The photoluminescence spectra of every individual region measured at T = 5 K are shown in figure 8.2b. The spectrum of bilayer WS_2 corresponding to the dark blue line in figure 8.2b, includes a higher energy peak ($\sim$ 2 eV) with double structure due to excitons (and trions) formed out of carriers excited at the K point and a low energy peak ($\sim$ 1.7 eV) attributed to indirect K-Γ recombination. In the bilayer InSe sample area only a peak at $\sim$ 1.9 eV corresponding to the so-called A transition in this material is resolved (light blue spectrum in figure 8.2b). The spectrum of the heterostructure region (red line in figure 8.2b) is dominated by a peak at about 1.55 eV and lies at lower energies than any of the spectral features of both individual constituents. The appearance of an additional peak in the heterointerface area strongly indicates the emergence of a radiative interlayer transition developed upon the formation of the interface.

We elucidate the nature of this transition by performing temperature dependent PL measurements in the interface region. The experimental data presented in figure 8.2c show the evolution of the PL peak in the interface region upon lowering the temperature down to 5 K. The integrated intensity of the heterostructure peak (X_0^I) progressively increases while the peak position experiences a blue-shift upon decreasing the temperature from 250 K to 5 K. This behavior is characteristic for a transition which is direct in momentum space. For instance, the direct K-K exciton transition ($X_0^{WS_2}$) in bilayer WS_2 shows qualitatively the same trend. In contrary, as presented in figure 8.2d, the peak due to indirect K-Γ transition ($IX_0^{WS_2}$) in WS_2 drops in intensity with decreasing temperature as expected from phonon mediated indirect transitions. Therefore, we conclude that the low energy peak emerging in the heterostructure originates from a transition which is direct in the momentum space.

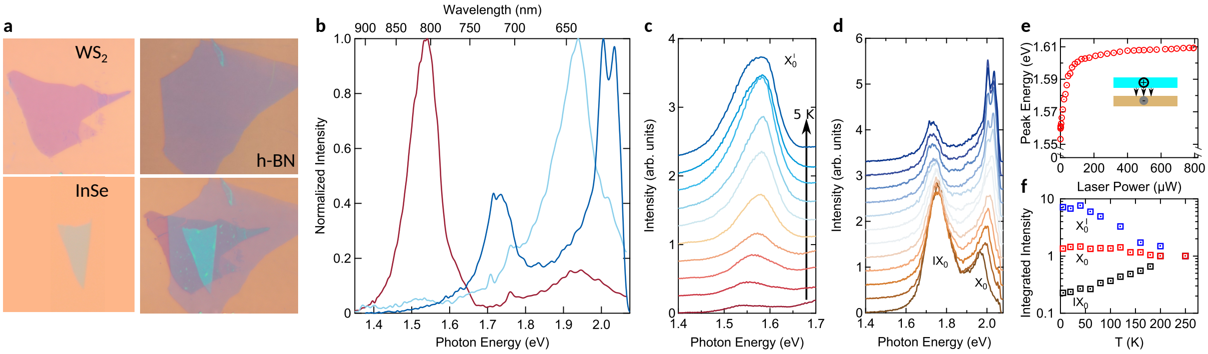

Figure 8.2: (a) Optical microscope images of a WS_2 and a InSe bilayer , of h-BN layer (∼ 10 layers), and of the assembled heterostructure. (b) Normalized photoluminescence spectra of WS_2 (dark blue line), InSe (light blue line) and of their interface (red line) acquired at T=5K. The peaks in WS_2 at 2 eV and 1.7 eV correspond K-K and K-Γ exciton recombination respectively. The feature in the InSe spectrum at 1.9 eV is due to A transition in this material. The heterostructure spectrum is dominated by the peak at 1.55 eV which is absent in the spectra of both of the constituents. (c),(d) Temperature dependence of the PL signal of the heterostructure (c) and of WS_2 (d) regions. The increase of integrated intensity of the heterostructure peak with the decrease of temperature demonstrates that this peak is due to transition which is direct in the momentum space. (e) Dependence of the heterointerface peak position on the laser power. (f) Integrated intensity as a function of temperature of heterointerface (open blue squares), WS_2 K-K (open red squares) and WS_2 K-Γ (open black squares) peaks.

The interlayer nature of the optical transition is demonstrated by the observation of a blue shift of the transition energy with increasing laser power. In figure 8.2e we show that the position of the PL peak shifts to higher energies by more than 50 meV when increasing the laser power before saturating at higher excitation power of about 200 μW. Similar behavior is reported for instance in $MoSe_2/WSe_2$ heterostructure[28], where the shift is a direct manifestation that the dipole of the exciton points out of the 2D planes and electrons and holes are confined in different layers (see also the sketch in the inset of figure 8.2e). The energy blue shift of the PL emission stems from the repulsive Coulomb interaction between excitons when electrons and holes are confined in different layers. The increase of the illumination power leads to an increase of the interlayer exciton density which enhances the repulsive interaction between the dipoles of the interlayer excitons and results in a subsequent blue shift of the PL line. In contrast, the same experiment performed in bare bilayer of WS_2 does not show any detectable shift of the PL lines since, in this case, excitons remain dominantly confined within the atomic plane of the TMD layers. The blue shift of the PL peak of the heterointerface, which is observed in all our investigated samples, is therefore the direct evidence of the formation of interlayer exciton in bilayer $InSe/WS_2$ heterostructures.

The experimental findings combined together allow us to unambiguously establish the nature of the low energy peak in the heterointerface area. This transition is due to radiative recombination of interlayer excitons reproduced in multiple samples (3 in total for bilayer-bilayer heterojunctions). Additional proof for the interlayer nature of these excitons is brought by photoluminescence excitation spectroscopy, presented in section 8.5.1, where the pronounced enhancement of the heterointerface peak intensity occurs at the energies corresponding to the intralayer transitions of both of the heterostructure components. Furthermore, the transition originating from the heterointerface area is direct in momentum space irrespective of rotational alignment between components (in none of the samples the constituent layers have been intentionally aligned with respect to each other) which have an in-plane lattice mismatch of about 15%. Therefore this transition most likely originates from recombination of an exciton formed out of an electron at the CBM of InSe (the Γ point) and a hole at the VBM of WS_2 (the Γ point) – *i.e.,* a Γ-Γ exciton.

8.3 Band alignment probed with Γ-Γ heterointerfaces

We next investigate whether the discussed mechanism of Γ-Γ transition can robustly yield radiative recombination of excitons (as long as CBM and VBM stays at Γ) by modifying the band structure of the constituent materials. Both WS_2 and InSe are known for the sizable change of their band structures when going from bilayers to thicker multilayers[124,249,250]. We, therefore, first start by studying two series of heterostructures in which thickness of either InSe or WS_2 layers are varied. More specifically, in the first series the thickness of the InSe layer is progressively increased from two to seven layers, and the thickness of WS_2 is kept fixed to bilayer. Photoluminescence spectra of this series, acquired at 5 K, are shown in figure 8.3a. In all cases the peak due to Γ-Γ exciton is resolved and the emission energy redshifts from 1.58 to 1.28 eV when increasing the thickness of InSe from 2 to 7 layers (see figure 8.3b). In the second series, where we vary the thickness of WS_2 and keep the number of InSe layers constant at four, the recombination due to Γ-Γ exciton is also solidly preserved. The heterointerface peak redshifts between 2 and 3 layers and remains further constant for thicker WS_2 layers (see figure 8.3c). The omnipresence of a radiative interlayer transition is consistent with having the relevant band extrema of the constituents at the Γ-point and their band alignment is of type II, in all cases.

The systematic observation of the interlayer transition through such a large variation of materials enables us to establish the relative band alignment between the heterostructure constituents. Determining the precise band alignment between two semiconductors is an arduous task but with the independent measurement of the optical transition energies in every individual area of a sample we construct the band diagrams shown in figures 8.3d and e, for varying InSe thickness with bilayer WS_2 and varying WS_2 thickness with four layer InSe, respectively. However, for sake of simplicity we assume that in the conduction band of bilayer WS_2 the K and Q valleys are nearly degenerate in energy and the optical band gap determined from our PL measurements coincides with the single particle band gap. In the first series (figure 8.3d) the increase of the number of InSe layers in the heterostructure – the constituent hosting the electron of the interlayer transition – leads to the decrease of the interlayer peak energy which implies that the energy (with the respect to vacuum level) of the conduction band of InSe itself lowers meanwhile its valence band, whose energy is given by the band gap of InSe, shifts towards higher energies. We note that starting from five layers InSe the valence band of InSe lies between the K- and the Γ-valleys of WS_2 . In the second series, where the constituent providing the hole of the Γ-Γ exciton (*i.e.,* WS_2) is varied, the energy of the interlayer transition remains nearly constant for layer thicknesses larger than bilayer. The position of the VBM in WS_2 , therefore, also stays constant for these thicknesses while the energy of the conduction band decreases rapidly with increasing WS_2 thickness. Remarkably, the same conclusion on the energy position of TMD VBM has been drawn in a recent ARPES experiment[15] (where the band structure up to the Fermi level of WS_2 is experimentally resolved).

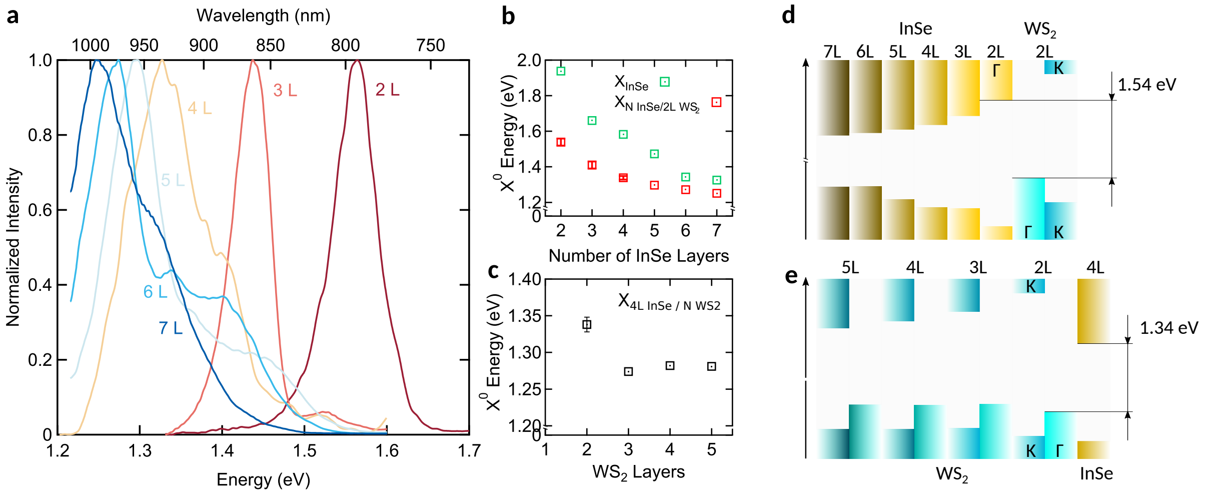

Figure 8.3: (a) PL spectra of Γ - Γ heterointerfaces assembled from bilayer WS_2 and InSe of different thickness. (b), (c) Γ - Γ heterointerface peak position as a function of number of InSe layers used in combination with WS_2 bilayer (b) and number of WS_2 layers combined with four layers of InSe (c). (d), (e) Band diagrams of WS_2 bilayer/ InSe N-layer (d) and WS_2 N-layer/ InSe 4L heterostructure series.

The obtained band diagrams allow to deduce the fundamental mechanism of charge transfer occurring in these heterointerfaces which further help to interprete spectral features resolved in the PL spectra. For all experiments described in figure 8.3 the laser excitation energy is tuned to the energy of the K-K exciton (2.03 eV) of WS_2 (see section 8.5.1). This optical excitation creates an electron and a hole in the K-valley of WS_2. Subsequently, the electron and the hole are transferred to the Γ-valleys of InSe and WS_2, respectively, because these bands represent the lowest local energy states in the system. A momentum direct interlayer Γ-Γ exciton can be formed out of these carriers, which recombines radiatively leading to the main PL peak in figure 8.3a. However, from the inferred band alignment in figure 8.3d, we can see that in heterostructures with bilayer WS_2 and InSe of five or more layers the valence band at Γ-point of InSe is energetically higher than the K valence valley in WS_2. This opens an additional relaxation path for photoexcited holes towards the Γ -point of InSe. This leads to the emergence of a high energy shoulder present in the PL spectrum of heterostructures composed of five layers of InSe seen in figure 8.3a. This additional peak coincides with the intralayer transition of the respective InSe thickness since holes transferred to the Γ -point of InSe form an exciton with electrons transferred to the Γ -conduction valley also in InSe. This scenario demonstrates the very efficient charge tranfer between WS_2 and InSe.

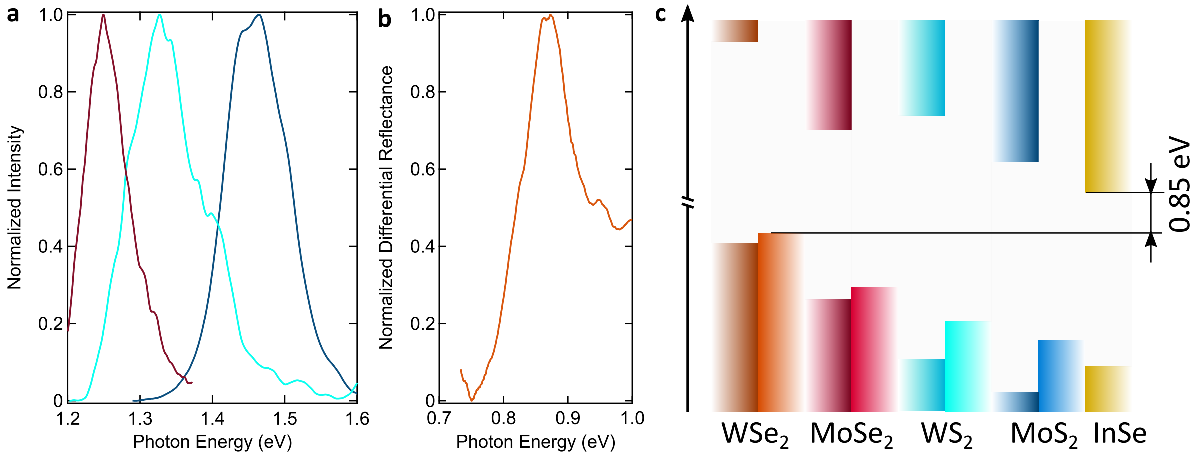

Figure 8.4: (a) PL spectra of Γ - Γ heterointerfaces assembled from 4L InSe combined with 2L $MoSe_2$ (red line), 2L WS_2 (light green line) and 2L MoS_2 (blue line). (b) Differential reflectance spectrum of 4L InSe/2L WSe_2 Γ - Γ heterointerface. (c) Band diagrams obtained from the spectra of (a) and (b).

The Γ-Γ exciton is a general phenomenon and it goes beyond the specific pair of materials discussed above. The combination of semiconductors can be picked out literally at random as long as the type II alignment is preserved and the respective band extrema stay at the Γ-point. For example, selecting MoS_2 or $MoSe_2$ (see figure 8.4a) as a component for the valence band edge or GaSe (see figure 8.6) – as the one for the conduction band edge always yield radiative Γ-Γ peaks resolved in PL. It is surprising in this context that no PL signal could be detected from a InSe/WSe_2 heterojunction. However from the PL measurements performed on the heterostructures shown in figure 8.3d – and assuming similar band offset between different TMD compounds as for monolayers[29] – the interlayer exciton energy in InSe/WSe_2 is expected at about 0.85 eV, as deduced from the reconstructed band diagram shown in figure 8.4c which shows the alignment of an InSe (four layers) with the TMD bilayers investigated in this work. This spectral interval is at the detection limit of this technique and to characterize this heterointerface we measure the differential reflectance of a InSe/WSe_2 (4L / 2L) heterostructure, presented in figure 8.4b. In consistency with our estimation a clear peak at about 0.89 mV is observed in the spectrum, consistent with having a momentum space direct transition at this energy. The possibility to obtain a semiconductor with direct band gap in the near-IR is very remarkable and can be very attractive for application in telecommunication.

8.4 Conclusion

Our work demonstrates a robust approach for the observation of radiative interlayer excitons in van-der-Waals heterostructures. It is based on the use of heterointerfaces in which the CBM of one of the constituents and the VBM of the other are in the center of the first Billouin zone, the Γ -point, which yields artificially created semiconductors with direct band gap. Systematic photoluminescence studies show that these heterointerfaces always host bright interlayer excitons (except for the case when the recombination energy is below the limit of the measurement system) irrespective of lattice parameters, lattice symmetry or rotational alignment of the components combined together. Our approach allows also to probe the band alignment and reveal the main mechanism of charge transfer in van-der-Waals heterostructures.

8.5 Appendix

8.5.1 Photoluminescence excitation spectroscopy

To understand the origin of the low energy peak emerging in the heterostructure region we perform photoluminescence excitation spectroscopy (PLE) measurements. In this experiment photoluminescence of the heterostructure is probed as a function of laser excitation energy. Figure 8.5a shows PLE map of 2L WS_2 /2L InSe heterostructure where pronounced increase of the PL signal is seen at laser energy of 2.45 eV and 2.03 eV. These peaks appear at the energies corresponding to A and B intralayer excitons in WS_2 . The enhancement of the low energy heterostructure peak at the transition energies of one of the heterostructure constituent component strongly suggest that this peak is due to interlayer recombination.

8.5.2 Photoluminescence of WS_2/GaSe heterointerface

Radiative recombination due to Γ - Γ excitons is also observed in heterointerfaces in which GaSe is used as the component for the conduction band edge. Photoluminescence spectrum of heterointerface assembled from bilayer WS_2 and 6 layers GaSe is shown in figure 8.6 (light blue line), where Γ - Γ exciton recombination is resolved as a peak at 1.63 eV.

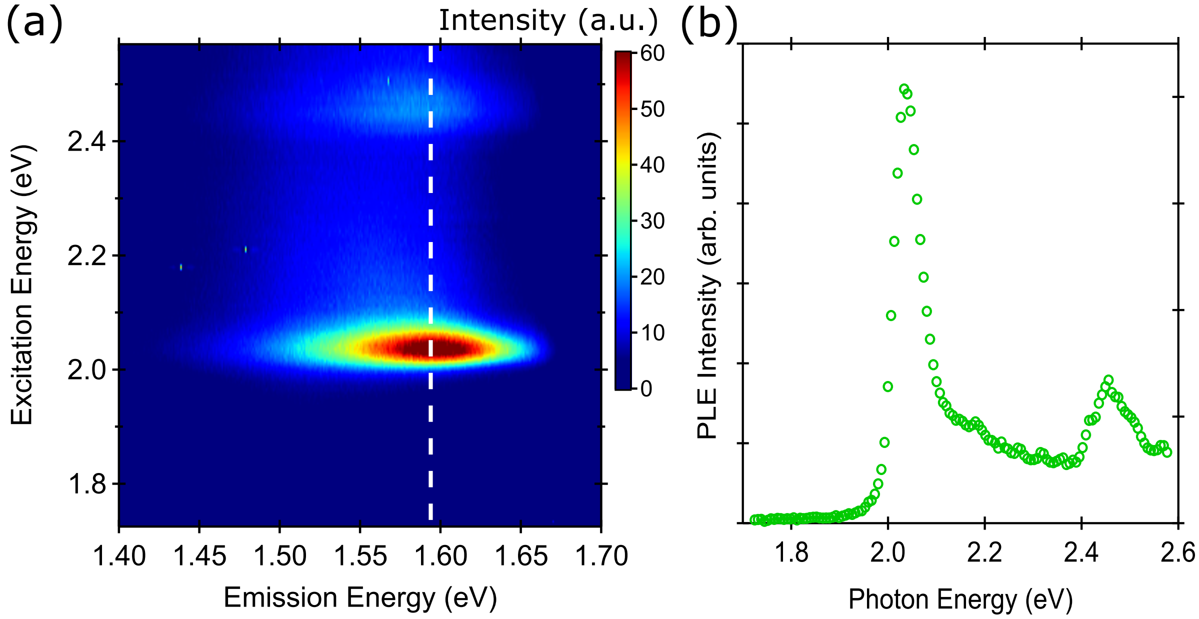

Figure 8.5: (a)Photoluminescence intensity of the heterointerface peak as a function of laser excitation energy (PLE map) for 2L WS_2 /2L InSe heterostructure. The enhancement of the peak occurs at energies corresponding to the intralayer A (2.03 eV) and B (2.45 eV) excitons of WS_2. (b) PL intensity along the white dashed line (panel (a)) shown with open green circles.

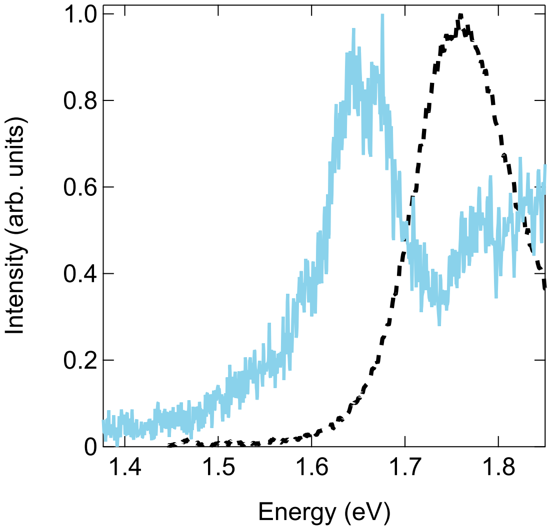

Figure 8.6: Normalized PL spectra of bilayer WS_2 (dashed black line) and of Γ - Γ heterointerface assembled from 2L WS_2 combined with 6L GaSe (light blue line).

References

[1] K S Novoselov, a K Geim, S V Morozov, D Jiang, M I Katsnelson, I V Grigorieva, S V Dubonos, and a a Firsov. Electric Field Effect in Atomically Thin Carbon Films (Suppl. info). *Science*, 306(October):1–12, 2004.

[2] K. S. Novoselov, A. K. Geim, S. V. Morozov, D. Jiang, M. I. Katsnelson, I. V. Grigorieva, S. V. Dubonos, and A. A. Firsov. Two-dimensional gas of massless Dirac fermions in graphene. *Nature*, 438(7065):197–200, 2005.

[3] Yuanbo Zhang, Yan Wen Tan, Horst L. Stormer, and Philip Kim. Experimental observation of the quantum Hall effect and Berry's phase in graphene. *Nature*, 438(7065):201–204, 2005.

[4] Simon M Sze and Kwok K Ng. *Physics of Semiconductor Devices*. John Wiley & Sons, 2006.

[5] R. Dingle, H. L. Störmer, A. C. Gossard, and W. Wiegmann. Electron mobilities in modulation-doped semiconductor heterojunction superlattices. *Applied Physics Letters*, 33(7):665–667, 1978.

[6] Takashi Mimura, Satoshi Hiyamizu, Toshio Fujii, and Kazuo Nanbu. A New Field-Effect Transistor with Selectively Doped GaAs/n-AlGaAs Heterojunctions. *Japanese Journal of Applied Physics*, 19(5):L225–L227, 1980.

[7] A Ohtomo and H Y Hwang. A high-mobility electron gas at the LaAlO 3 / SrTiO 3 heterointerface. *Nature*, 427(January):423–427, 2004.

[8] Nicolas Mounet, Marco Gibertini, Philippe Schwaller, Davide Campi, Andrius Merkys, Antimo Marrazzo, Thibault Sohier, Ivano Eligio Castelli, Andrea Cepellotti, Giovanni Pizzi, and Nicola Marzari. Two-dimensional materials from high-throughput computational exfoliation of experimentally known compounds. *Nature Nanotechnology*, 13(3):246–252, 2018.

[9] C R Dean, A F Young, I Meric, C Lee, L Wang, S Sorgenfrei, K Watanabe, T Taniguchi, P Kim, K L Shepard, and J Hone. Boron

nitride substrates for high-quality graphene electronics. *Nature nanotechnology*, 5(10):722–6, 2010.

[10] Manish Chhowalla, Hyeon Suk Shin, Goki Eda, Lain Jong Li, Kian Ping Loh, and Hua Zhang. The chemistry of two-dimensional layered transition metal dichalcogenide nanosheets. *Nature Chemistry*, 5(4):263–275, 2013.

[11] Alexey A. Soluyanov, Dominik Gresch, Zhijun Wang, Quansheng Wu, Matthias Troyer, Xi Dai, and B. Andrei Bernevig. Type-II Weyl semimetals. *Nature*, 527(7579):495–498, 2015.

[12] Xiaoxiang Xi, Zefang Wang, Weiwei Zhao, Ju Hyun Park, Kam Tuen Law, Helmuth Berger, László Forró, Jie Shan, and Kin Fai Mak. Ising pairing in superconducting NbSe2 atomic layers. *Nature Physics*, 12(2):139–143, 2016.

[13] Claus Klingshirn. *Semiconductor optics.* Springer, Berlin, 2012.

[14] Yi Zhang, Miguel M. Ugeda, Chenhao Jin, Su Fei Shi, Aaron J. Bradley, Ana Martín-Recio, Hyejin Ryu, Jonghwan Kim, Shujie Tang, Yeongkwan Kim, Bo Zhou, Choongyu Hwang, Yulin Chen, Feng Wang, Michael F. Crommie, Zahid Hussain, Zhi Xun Shen, and Sung Kwan Mo. Electronic Structure, Surface Doping, and Optical Response in Epitaxial WSe2 Thin Films. *Nano Letters*, 16(4):2485–2491, 2016.

[15] Neil R. Wilson, Paul V. Nguyen, Kyle Seyler, Pasqual Rivera, Alexander J. Marsden, Zachary P.L. Laker, Gabriel C. Constantinescu, Viktor Kandyba, Alexei Barinov, Nicholas D.M. Hine, Xiaodong Xu, and David H. Cobden. Determination of band offsets, hybridization, and exciton binding in 2D semiconductor heterostructures. *Science Advances*, 3(2):1–8, 2017.

[16] Klaus von Klitzing. The Quantized Hall Effect. *Reviews of Modern Physics*, 58(3), 1986.

[17] K. S. Novoselov, Z. Jiang, Y. Zhang, S. V. Morozov, H. L. Stormer, U. Zeitler, J. C. Maan, G. S. Boebinger, P. Kim, and A. K. Geim. Room-temperature quantum hall effect in graphene. *Science*, 315(5817):1379, 2007.

[18] Shuigang Xu, Junying Shen, Gen Long, Zefei Wu, Zhi Qiang Bao, Cheng Cheng Liu, Xiao Xiao, Tianyi Han, Jiangxiazi Lin, Yingying

Wu, Huanhuan Lu, Jianqiang Hou, Liheng An, Yuanwei Wang, Yuan Cai, K. M. Ho, Yuheng He, Rolf Lortz, Fan Zhang, and Ning Wang. Odd-Integer Quantum Hall States and Giant Spin Susceptibility in p -Type Few-Layer WSe2. *Physical Review Letters*, 118(6):1–6, 2017.

[19] M. M. Fogler, L. V. Butov, and K. S. Novoselov. High-temperature superfluidity with indirect excitons in van der Waals heterostructures. *Nature Communications*, 5(May):1–5, 2014.

[20] Alexey Chernikov, Timothy C. Berkelbach, Heather M. Hill, Albert Rigosi, Yilei Li, Ozgur Burak Aslan, David R. Reichman, Mark S. Hybertsen, and Tony F. Heinz. Exciton binding energy and nonhydrogenic Rydberg series in monolayer WS2. *Physical Review Letters*, 113(7):1–5, 2014.

[21] Gang Wang, Alexey Chernikov, Mikhail M. Glazov, Tony F. Heinz, Xavier Marie, Thierry Amand, and Bernhard Urbaszek. Colloquium: Excitons in atomically thin transition metal dichalcogenides. *Reviews of Modern Physics*, 90(2):21001, 2018.

[22] A K Geim and I V Grigorieva. Van der Waals heterostructures. *Nature*, 499(7459):419–425, jul 2013.

[23] K. S. Novoselov, A. Mishchenko, A. Carvalho, and A. H. Castro Neto. 2D materials and van der Waals heterostructures. *Science*, 353(6298), 2016.

[24] Matthew Yankowitz, Jiamin Xue, Daniel Cormode, Javier D Sanchez-Yamagishi, K Watanabe, T Taniguchi, Pablo Jarillo-Herrero, Philippe Jacquod, and Brian J LeRoy. Emergence of superlattice Dirac points in graphene on hexagonal boron nitride. *Nature Physics*, 8(5):382–386, may 2012.

[25] C R Dean, L Wang, P Maher, C Forsythe, F Ghahari, Y Gao, J Katoch, M Ishigami, P Moon, M Koshino, T Taniguchi, K Watanabe, K L Shepard, J Hone, and P Kim. Hofstadter's butterfly and the fractal quantum Hall effect in moire superlattices. *Nature*, 497(7451):598–602, may 2013.

[26] L A Ponomarenko, R V Gorbachev, G L Yu, D C Elias, R Jalil, A A Patel, A Mishchenko, A S Mayorov, C R Woods, J R Wallbank, M Mucha-Kruczynski, B A Piot, M Potemski, I V Grigorieva, K S Novoselov, F Guinea, V I Fal'ko, and A K Geim. Cloning of Dirac

fermions in graphene superlattices. *Nature*, 497(7451):594–597, may 2013.

[27] Yuan Cao, Valla Fatemi, Shiang Fang, Kenji Watanabe, Takashi Taniguchi, Efthimios Kaxiras, and Pablo Jarillo-Herrero. Unconventional superconductivity in magic-angle graphene superlattices. *Nature*, 556(7699):43–50, 2018.

[28] Pasqual Rivera, John R. Schaibley, Aaron M. Jones, Jason S. Ross, Sanfeng Wu, Grant Aivazian, Philip Klement, Kyle Seyler, Genevieve Clark, Nirmal J. Ghimire, Jiaqiang Yan, D. G. Mandrus, Wang Yao, and Xiaodong Xu. Observation of long-lived interlayer excitons in monolayer MoSe2–WSe2 heterostructures. *Nature Communications*, 6:6242, 2015.

[29] Evgeniy Ponomarev, Nicolas Ubrig, Ignacio Gutiérrez-Lezama, Helmuth Berger, and Alberto F Morpurgo. Semiconducting van der Waals Interfaces as Artificial Semiconductors. *Nano Letters*, 18(8):5146–5152, aug 2018.

[30] Sukang Bae, Hyeong Keun Kim, Youngbin Lee, Xianfang Xu, Jae-Sung Park, Yi Zheng, Jayakumar Balakrishnan, Danho Im, Tian Lei, Young Il Song, Young Jin Kim, Kwang S. Kim, Barbaros Özyilmaz, Jong-Hyun Ahn, Byung Hee Hong, and Sumio Iijima. 30 inch Roll-Based Production of High-Quality Graphene Films for Flexible Transparent Electrodes. 5(June):1–5, 2010.

[31] R. Ribeiro-Palau, F. Lafont, J. Brun-Picard, D. Kazazis, A. Michon, F. Cheynis, O. Couturaud, C. Consejo, B. Jouault, W. Poirier, and F. Schopfer. Quantum Hall resistance standard in graphene devices under relaxed experimental conditions. *Nature Nanotechnology*, 10(11):965–971, 2015.

[32] Arokia Nathan, Arman Ahnood, Matthew T. Cole, Sungsik Lee, Yuji Suzuki, Pritesh Hiralal, Francesco Bonaccorso, Tawfique Hasan, Luis Garcia-Gancedo, Andriy Dyadyusha, Samiul Haque, Piers Andrew, Stephan Hofmann, James Moultrie, Daping Chu, Andrew J. Flewitt, Andrea C. Ferrari, Michael J. Kelly, John Robertson, Gehan A.J. Amaratunga, and William I. Milne. Flexible electronics: The next ubiquitous platform. *Proceedings of the IEEE*, 100(SPL CONTENT):1486–1517, 2012.

[33] Deji Akinwande, Nicholas Petrone, and James Hone. Two-dimensional flexible nanoelectronics. *Nature Communications*, 5:1–12, 2014.

[34] Shideh Kabiri Ameri, Rebecca Ho, Hongwoo Jang, Li Tao, Youhua Wang, Liu Wang, David M. Schnyer, Deji Akinwande, and Nanshu Lu. Graphene Electronic Tattoo Sensors. *ACS Nano*, 11(8):7634–7641, 2017.

[35] Jesse D. Benck, Thomas R. Hellstern, Jakob Kibsgaard, Pongkarn Chakthranont, and Thomas F. Jaramillo. Catalyzing the hydrogen evolution reaction (HER) with molybdenum sulfide nanomaterials. *ACS Catalysis*, 4(11):3957–3971, 2014.

[36] Di Xiao, Gui Bin Liu, Wanxiang Feng, Xiaodong Xu, and Wang Yao. Coupled spin and valley physics in monolayers of MoS 2 and other group-VI dichalcogenides. *Physical Review Letters*, 108(19):1–5, 2012.

[37] Gui Bin Liu, Di Xiao, Yugui Yao, Xiaodong Xu, and Wang Yao. Electronic structures and theoretical modelling of two-dimensional group-VIB transition metal dichalcogenides. *Chemical Society Reviews*, 44(9):2643–2663, 2015.

[38] Andrea Splendiani, Liang Sun, Yuanbo Zhang, Tianshu Li, Jonghwan Kim, Chi-Yung Chim, Giulia Galli, and Feng Wang. Emerging Photoluminescence in Monolayer MoS2. *Nano Letters*, 10(4):1271–1275, apr 2010.

[39] K. Komider, J. W. González, and J. Fernández-Rossier. Large spin splitting in the conduction band of transition metal dichalcogenide monolayers. *Physical Review B - Condensed Matter and Materials Physics*, 88(24):1–7, 2013.

[40] Z. Y. Zhu, Y. C. Cheng, and U. Schwingenschlögl. Giant spin-orbit-induced spin splitting in two-dimensional transition-metal dichalcogenide semiconductors. *Physical Review B - Condensed Matter and Materials Physics*, 84(15):1–5, 2011.

[41] Alejandro Molina-Sánchez, Davide Sangalli, Kerstin Hummer, Andrea Marini, and Ludger Wirtz. Effect of spin-orbit interaction on the optical spectra of single-layer, double-layer, and bulk MoS2. *Physical Review B*, 88(4):045412, 2013.

[42] Hualing Zeng, Junfeng Dai, Wang Yao, Di Xiao, and Xiaodong Cui. Valley polarization in MoS 2 monolayers by optical pumping. *Nature Nanotechnology*, 7(8):490–493, 2012.

[43] Kin Fai Mak, Keliang He, Jie Shan, and Tony F. Heinz. Control of valley polarization in monolayer MoS2 by optical helicity. *Nature Nanotechnology*, 7(8):494–498, 2012.

[44] Ting Cao, Gang Wang, Wenpeng Han, Huiqi Ye, Chuanrui Zhu, Junren Shi, Qian Niu, Pingheng Tan, Enge Wang, Baoli Liu, and Ji Feng. Valley-selective circular dichroism of monolayer molybdenum disulphide. *Nature Communications*, 3(May):885–887, 2012.

[45] K. F. Mak, K. L. McGill, J. Park, and P. L. McEuen. The valley Hall effect in MoS2 transistors. *Science*, 344(6191):1489–1492, 2014.

[46] Nicolas Ubrig, Sanghyun Jo, Marc Philippi, Davide Costanzo, Helmuth Berger, Alexey B. Kuzmenko, and Alberto F. Morpurgo. Microscopic Origin of the Valley Hall Effect in Transition Metal Dichalcogenides Revealed by Wavelength-Dependent Mapping. *Nano Letters*, 17(9):5719–5725, 2017.

[47] Kin Fai Mak, Keliang He, Changgu Lee, Gwan Hyoung Lee, James Hone, Tony F. Heinz, and Jie Shan. Tightly bound trions in monolayer MoS2. *Nature Materials*, 12(3):207–211, 2013.

[48] Jingzhi Shang, Xiaonan Shen, Chunxiao Cong, Namphung Peimyoo, Bingchen Cao, Mustafa Eginligil, and Ting Yu. Observation of excitonic fine structure in a 2D transition-metal dichalcogenide semiconductor. *ACS Nano*, 9(1):647–655, 2015.

[49] M. Manca, M. M. Glazov, C. Robert, F. Cadiz, T. Taniguchi, K. Watanabe, E. Courtade, T. Amand, P. Renucci, X. Marie, G. Wang, and B. Urbaszek. Enabling valley selective exciton scattering in monolayer WSe 2 through upconversion. *Nature Communications*, 8:1–7, 2017.

[50] M. M. Glazov, T. Amand, X. Marie, D. Lagarde, L. Bouet, and B. Urbaszek. Exciton fine structure and spin decoherence in monolayers of transition metal dichalcogenides. *Physical Review B - Condensed Matter and Materials Physics*, 89(20):1–5, 2014.

[51] M. M. Glazov, E. L. Ivchenko, G. Wang, T. Amand, X. Marie, B. Urbaszek, and B. L. Liu. Spin and valley dynamics of excitons in tran-

sition metal dichalcogenide monolayers. *Physica Status Solidi (B) Basic Research*, 252(11):2349–2362, 2015.

[52] Ziliang Ye, Ting Cao, Kevin O'Brien, Hanyu Zhu, Xiaobo Yin, Yuan Wang, Steven G. Louie, and Xiang Zhang. Probing excitonic dark states in single-layer tungsten disulphide. *Nature*, 513(7517):214–218, 2014.

[53] Xiao Xiao Zhang, Yumeng You, Shu Yang Frank Zhao, and Tony F. Heinz. Experimental Evidence for Dark Excitons in Monolayer WSe2. *Physical Review Letters*, 115(25):1–6, 2015.

[54] Wu Zhou, Xiaolong Zou, Sina Najmaei, Zheng Liu, Yumeng Shi, Jing Kong, Jun Lou, Pulickel M. Ajayan, Boris I. Yakobson, and Juan Carlos Idrobo. Intrinsic structural defects in monolayer molybdenum disulfide. *Nano Letters*, 13(6):2615–2622, 2013.

[55] Jinhua Hong, Zhixin Hu, Matt Probert, Kun Li, Danhui Lv, Xinan Yang, Lin Gu, Nannan Mao, Qingliang Feng, Liming Xie, Jin Zhang, Dianzhong Wu, Zhiyong Zhang, Chuanhong Jin, Wei Ji, Xixiang Zhang, Jun Yuan, and Ze Zhang. Exploring atomic defects in molybdenum disulphide monolayers. *Nature Communications*, 6:1–8, 2015.

[56] Péter Vancsó, Gábor Zsolt Magda, János Pető, Ji-Young Noh, Yong-Sung Kim, Chanyong Hwang, László P. Biró, and Levente Tapasztó. The intrinsic defect structure of exfoliated MoS2 single layers revealed by Scanning Tunneling Microscopy. *Scientific Reports*, 6(April):29726, 2016.

[57] Hao Qiu, Tao Xu, Zilu Wang, Wei Ren, Haiyan Nan, Zhenhua Ni, Qian Chen, Shijun Yuan, Feng Miao, Fengqi Song, Gen Long, Yi Shi, Litao Sun, Jinlan Wang, and Xinran Wang. Hopping transport through defect-induced localized states in molybdenum disulphide. *Nature Communications*, 4:1–6, 2013.

[58] Dumitru Dumcenco, Dmitry Ovchinnikov, Kolyo Marinov, Predrag Lazić, Marco Gibertini, Nicola Marzari, Oriol Lopez Sanchez, Yen Cheng Kung, Daria Krasnozhon, Ming Wei Chen, Simone Bertolazzi, Philippe Gillet, Anna Fontcuberta I Morral, Aleksandra Radenovic, and Andras Kis. Large-area epitaxial monolayer MoS2. *ACS Nano*, 9(4):4611–4620, 2015.

[59] Zhores I. Alferov. Nobel lecture: The double heterostructure concept and its applications in physics, electronics, and technology. *Reviews of Modern Physics*, 73(3):767–782, 2001.

[60] Herbert Kroemer. Nobel Lecture: Quasielectric fields and band offsets: teaching electrons new tricks. *Reviews of Modern Physics*, 73(3):783–793, 2001.

[61] Matthew Z. Bellus, Ming Li, Samuel D. Lane, Frank Ceballos, Qiannan Cui, Xiao Cheng Zeng, and Hui Zhao. Type-I van der Waals heterostructure formed by MoS2 and ReS2 monolayers. *Nanoscale Horizons*, 2(1):31–36, 2017.

[62] Ignacio Gutiérrez-Lezama. *Charge transfer and transport in organic single-crystal transistors and interfaces.* Thèse de doctorat, Univeristy of Geneva, 2013.

[63] E. V. Calman, C. J. Dorow, M. M. Fogler, L. V. Butov, S. Hu, A. Mishchenko, and A. K. Geim. Control of excitons in multi-layer van der Waals heterostructures. *Applied Physics Letters*, 108(10):1–5, 2016.

[64] E. V. Calman, M. M. Fogler, L. V. Butov, S. Hu, A. Mishchenko, and A. K. Geim. Indirect excitons in van der Waals heterostructures at room temperature. *Nature Communications*, 9(1):1–5, 2018.

[65] C. Robert, D. Lagarde, F. Cadiz, G. Wang, B. Lassagne, T. Amand, A. Balocchi, P. Renucci, S. Tongay, B. Urbaszek, and X. Marie. Exciton radiative lifetime in transition metal dichalcogenide monolayers. *Physical Review B*, 93(20):1–10, 2016.

[66] Bastian Miller, Alexander Steinhoff, Borja Pano, Julian Klein, Frank Jahnke, Alexander Holleitner, and Ursula Wurstbauer. Long-Lived Direct and Indirect Interlayer Excitons in van der Waals Heterostructures. *Nano Letters*, 17(9):5229–5237, 2017.

[67] L. V. Butov. Excitonic devices. *Superlattices and Microstructures*, 108:2–26, 2017.

[68] A. A. High, A. T. Hammack, L. V. Butov, M. Hanson, and A. C. Gossard. Exciton optoelectronic transistor. *Optics Letters*, 32(17):2466, 2007.

[69] Jason S Ross, Pasqual Rivera, John Schaibley, Eric Lee-Wong, Hongyi Yu, Takashi Taniguchi, Kenji Watanabe, Jiaqiang Yan, David Mandrus, David Cobden, Wang Yao, and Xiaodong Xu. Interlayer Exciton Optoelectronics in a 2D Heterostructure p–n Junction. *Nano Letters*, 17(2):638–643, feb 2017.

[70] Hongyi Yu, Yong Wang, Qingjun Tong, Xiaodong Xu, and Wang Yao. Anomalous Light Cones and Valley Optical Selection Rules of Interlayer Excitons in Twisted Heterobilayers. *Physical Review Letters*, 115(18):1–5, 2015.

[71] Pasqual Rivera, Hongyi Yu, Kyle L. Seyler, Nathan P. Wilson, Wang Yao, and Xiaodong Xu. Interlayer valley excitons in heterobilayers of transition metal dichalcogenides. *Nature Nanotechnology*, 13(11):1004–1015, 2018.

[72] Moon Sung Kang and C. Daniel Frisbie. A pedagogical perspective on ambipolar FETs. *ChemPhysChem*, 14(8):1547–1552, 2013.

[73] Matthew J. Panzer, Christopher R. Newman, and C. Daniel Frisbie. Low-voltage operation of a pentacene field-effect transistor with a polymer electrolyte gate dielectric. *Applied Physics Letters*, 86(10):1–3, 2005.

[74] Hidekazu Shimotani, Haruhiko Asanuma, Jun Takeya, and Yoshihiro Iwasa. Electrolyte-gated charge accumulation in organic single crystals. *Applied Physics Letters*, 89(20):8–11, 2006.

[75] Rajiv Misra, Mitchell McCarthy, and Arthur F. Hebard. Electric field gating with ionic liquids. *Applied Physics Letters*, 90(5):2005–2008, 2007.

[76] Daniele Braga, Ignacio Gutiérrez Lezama, Helmuth Berger, and Alberto F. Morpurgo. Quantitative determination of the band gap of WS 2 with ambipolar ionic liquid-gated transistors. *Nano Letters*, 12(10):5218–5223, 2012.

[77] Sanghyun Jo, Nicolas Ubrig, Helmuth Berger, Alexey B. Kuzmenko, and Alberto F. Morpurgo. Mono- and bilayer WS2 light-emitting transistors. *Nano Letters*, 14(4):2019–2025, 2014.

[78] Bryan D Paulsen and C Daniel Frisbie. Dependence of conductivity on charge density and electrochemical potential in polymer semiconductors gated with ionic liquids. *Journal of Physical Chemistry C*, 116(4):3132–3141, 2012.

[79] Ignacio Gutiérrez Lezama, Alberto Ubaldini, Maria Longobardi, Enrico Giannini, Christoph Renner, Alexey B Kuzmenko, and Alberto F Morpurgo. Surface transport and band gap structure of exfoliated 2H-MoTe2 crystals. *2D Materials*, 1(2), 2014.

[80] Evgeniy Ponomarev, Ignacio Gutiérrez-Lezama, Nicolas Ubrig, and Alberto F. Morpurgo. Ambipolar Light-Emitting Transistors on Chemical Vapor Deposited Monolayer MoS2. *Nano Letters*, 15(12):8289–8294, 2015.

[81] Nicolas Ubrig, Sanghyun Jo, Helmuth Berger, Alberto F. Morpurgo, and Alexey B. Kuzmenko. Scanning photocurrent microscopy reveals electron-hole asymmetry in ionic liquid-gated WS2 transistors. *Applied Physics Letters*, 104(17), 2014.

[82] Hong Li, Qing Zhang, Chin Chong Ray Yap, Beng Kang Tay, Teo Hang Tong Edwin, Aurelien Olivier, and Dominique Baillargeat. From bulk to monolayer MoS 2: Evolution of Raman scattering. *Advanced Functional Materials*, 22(7):1385–1390, 2012.

[83] Hiram J. Conley, Bin Wang, Jed I. Ziegler, Richard F. Haglund, Sokrates T. Pantelides, and Kirill I. Bolotin. Bandgap engineering of strained monolayer and bilayer MoS2. *Nano Letters*, 13(8):3626–3630, 2013.

[84] P J Zomer, M H D Guimarães, J C Brant, N Tombros, and B J van Wees. Fast pick up technique for high quality heterostructures of bilayer graphene and hexagonal boron nitride. *Applied Physics Letters*, 105(1):13101, jul 2014.

[85] Qing Hua Wang, Kourosh Kalantar-Zadeh, Andras Kis, Jonathan N Coleman, and Michael S Strano. Electronics and optoelectronics of two-dimensional transition metal dichalcogenides. *Nature nanotechnology*, 7(11):699–712, 2012.

[86] Sheneve Z. Butler, Shawna M. Hollen, Linyou Cao, Yi Cui, Jay a. Gupta, Humberto R. Gutiérrez, Tony F. Heinz, Seung Sae Hong, Jiaxing Huang, Ariel F. Ismach, Ezekiel Johnston-Halperin, Masaru Kuno, Vladimir V. Plashnitsa, Richard D. Robinson, Rodney S. Ruoff, Sayeef Salahuddin, Jie Shan, Li Shi, Michael G. Spencer, Mauricio Terrones, Wolfgang Windl, and Joshua E. Goldberger. Progress, challenges, and opportunities in two-dimensional materials beyond graphene. *ACS Nano*, 7(4):2898–2926, 2013.

[87] Deep Jariwala, Vinod K Sangwan, Lincoln J Lauhon, Tobin J Marks, and Mark C Hersam. Emerging Device Applications for Semiconducting Two-Dimensional Transition Metal Dichalcogenides. *ACS nano*, 8(2):1102–1120, 2014.

[88] Oriol Lopez-Sanchez, Dominik Lembke, Metin Kayci, Aleksandra Radenovic, and Andras Kis. Ultrasensitive photodetectors based on monolayer MoS2. *Nature nanotechnology*, 8(7):497–501, 2013.

[89] Andreas Pospischil, Marco M Furchi, and Thomas Mueller. Solar-energy conversion and light emission in an atomic monolayer p-n diode. *Nature nanotechnology*, 9(4):257–61, 2014.

[90] Britton W H Baugher, Hugh O H Churchill, Yafang Yang, and Pablo Jarillo-Herrero. Optoelectronic devices based on electrically tunable p-n diodes in a monolayer dichalcogenide. *Nature nanotechnology*, 9(4):262–7, 2014.

[91] R. S. Sundaram, M. Engel, A. Lombardo, R. Krupke, A. C. Ferrari, Ph Avouris, and M. Steiner. Electroluminescence in Single Layer MoS 2. *Nano Letters*, 13(4):1416–1421, apr 2013.

[92] Jason S Ross, Philip Klement, Aaron M Jones, Nirmal J Ghimire, Jiaqiang Yan, D G Mandrus, Takashi Taniguchi, Kenji Watanabe, Kenji Kitamura, Wang Yao, David H Cobden, and Xiaodong Xu. Electrically tunable excitonic light-emitting diodes based on monolayer WSe2 p-n junctions. *Nature nanotechnology*, 9(4):268–72, 2014.

[93] Y J Zhang, T Oka, R Suzuki, J T Ye, and Y Iwasa. Electrically Switchable Chiral Light-Emitting Transistor. *Science*, 344(6185):725–728, 2014.

[94] Keng-Ku Liu, Wenjing Zhang, Yi-Hsien Lee, Yu-Chuan Lin, Mu-Tung Chang, Ching-Yuan Su, Chia-Seng Chang, Hai Li, Yumeng Shi, Hua Zhang, Chao-Sung Lai, and Lain-Jong Li. Growth of Large-Area and Highly Crystalline MoS2 Thin Layers on Insulating Substrates. *Nano Letters*, 12(3):1538–1544, mar 2012.

[95] Yi-Hsien Lee, Xin-Quan Zhang, Wenjing Zhang, Mu-Tung Chang, Cheng-Te Lin, Kai-Di Chang, Ya-Chu Yu, Jacob Tse-Wei Wang, Chia-Seng Chang, Lain-Jong Li, and Tsung-Wu Lin. Synthesis of Large-Area MoS2 Atomic Layers with Chemical Vapor Deposition. *Advanced Materials*, 24(17):2320–2325, may 2012.

[96] Yongjie Zhan, Zheng Liu, Sina Najmaei, Pulickel M Ajayan, and Jun Lou. Large-Area Vapor-Phase Growth and Characterization of MoS2 Atomic Layers on a SiO2 Substrate. *Small*, 8(7):966–971, apr 2012.

[97] Yumeng Shi, Wu Zhou, Ang-Yu Lu, Wenjing Fang, Yi-Hsien Lee, Allen Long Hsu, Soo Min Kim, Ki Kang Kim, Hui Ying Yang, Lain-Jong Li, Juan-Carlos Idrobo, and Jing Kong. van der Waals Epitaxy of MoS2 Layers Using Graphene As Growth Templates. *Nano Letters*, 12(6):2784–2791, jun 2012.

[98] Arend M van der Zande, Pinshane Y Huang, Daniel A Chenet, Timothy C Berkelbach, YuMeng You, Gwan-Hyoung Lee, Tony F Heinz, David R Reichman, David A Muller, and James C Hone. Grains and grain boundaries in highly crystalline monolayer molybdenum disulphide. *Nature materials*, 12(6):554–61, 2013.

[99] Sina Najmaei, Zheng Liu, Wu Zhou, Xiaolong Zou, Gang Shi, Sidong Lei, Boris I Yakobson, Juan-Carlos Idrobo, Pulickel M Ajayan, and Jun Lou. Vapour phase growth and grain boundary structure of molybdenum disulphide atomic layers. *Nature materials*, 12(8):754–9, 2013.

[100] Hennrik Schmidt, Shunfeng Wang, Leiqiang Chu, Minglin Toh, Rajeev Kumar, Weijie Zhao, A. H. Castro Neto, Jens Martin, Shaffique Adam, Barbaros Özyilmaz, and Goki Eda. Transport properties of monolayer MoS2 grown by chemical vapor deposition. *Nano Letters*, 14(4):1909–1913, 2014.

[101] Xingli Wang, Yongji Gong, Gang Shi, Wai Leong Chow, Kunttal Keyshar, Gonglan Ye, Robert Vajtai, Jun Lou, Zheng Liu, Emilie Ringe, Beng Kang Tay, and Pulickel M. Ajayan. Chemical Vapor Deposition Growth of Crystalline Monolayer MoSe2. *ACS nano*, 8(5):5125–5131, 2014.

[102] Jing Xia, Xing Huang, Ling-Zhi Liu, Meng Wang, Lei Wang, Ben Huang, Dan-Dan Zhu, Jun-Jie Li, Chang-Zhi Gu, and Xiang-Min Meng. CVD synthesis of large-area, highly crystalline MoSe2 atomic layers on diverse substrates and application to photodetectors. *Nanoscale*, 6(15):8949–55, 2014.

[103] Yu Zhang, Yanfeng Zhang, Qingqing Ji, Jing Ju, Hongtao Yuan, Jianping Shi, Teng Gao, Donglin Ma, Mengxi Liu, Yubin Chen, Xiuju Song, Harold Y Hwang, Yi Cui, and Zhongfan Liu. Controlled

Growth of High-Quality Monolayer WS 2 Layers on Sapphire. *ACS nano*, 7(10):8963–8971, 2013.

[104] Jing Kai Huang, Jiang Pu, Chang Lung Hsu, Ming Hui Chiu, Zhen Yu Juang, Yung Huang Chang, Wen Hao Chang, Yoshihiro Iwasa, Taishi Takenobu, and Lain Jong Li. Large-area synthesis of highly crystalline WSe2 monolayers and device applications. *ACS Nano*, 8(1):923–930, 2014.

[105] Lili Yu, Yi-Hsien Lee, Xi Ling, Elton J. G. Santos, Yong Cheol Shin, Yuxuan Lin, Madan Dubey, Efthimios Kaxiras, Jing Kong, Han Wang, and Tomás Palacios. Graphene/MoS 2 Hybrid Technology for Large-Scale Two- Dimensional Electronics. *Nano Letters*, 14(6):3055–3063, 2014.

[106] Byungjin Cho, Ah Ra Kim, Youngjin Park, Jongwon Yoon, Young-Joo Lee, Sangchul Lee, Tae Jin Yoo, Chang Goo Kang, Byoung Hun Lee, Heung Cho Ko, Dong-Ho Kim, and Myung Gwan Hahm. Bifunctional Sensing Characteristics of Chemical Vapor Deposition Synthesized Atomic-Layered MoS2. *ACS Applied Materials & Interfaces*, 7(4):2952–2959, 2015.

[107] Jiang Pu, Yohei Yomogida, Keng-Ku Liu, Lain-Jong Li, Yoshihiro Iwasa, and Taishi Takenobu. Highly flexible MoS2 thin-film transistors with ion gel dielectrics. *Nano letters*, 12(8):4013–7, 2012.

[108] Bilu Liu, Mohammad Fathi, Liang Chen, Ahmad Abbas, Yuqiang Ma, and Chongwu Zhou. Chemical Vapor Deposition Growth of Monolayer WSe 2 with Tunable Device Characteristics and Growth. *ACS nano*, 9(6):6119–6127, 2015.

[109] Yijin Zhang, Jianting Ye, Yusuke Matsuhashi, and Yoshihiro Iwasa. Ambipolar MoS2 thin flake transistors. *Nano letters*, 12(3):1136–40, 2012.

[110] Kin Fai Mak, Changgu Lee, James Hone, Jie Shan, and Tony F. Heinz. Atomically thin MoS2: A new direct-gap semiconductor. *Physical Review Letters*, 105(13):2–5, 2010.

[111] Toshiaki Kato and Toshiro Kaneko. Optical Detection of a Highly Localized Impurity State in Monolayer Tungsten Disulfide. *ACS Nano*, 8(12):12777–12785, 2014.

[112] Shinichiro Mouri, Yuhei Miyauchi, and Kazunari Matsuda. Tunable photoluminescence of monolayer MoS2 via chemical doping. *Nano Letters*, 13(12):5944–5948, 2013.

[113] B Radisavljevic, A Radenovic, J Brivio, V Giacometti, and A Kis. Single-layer MoS2 transistors. *Nature nanotechnology*, 6(3):147–150, 2011.

[114] Branimir Radisavljevic and Andras Kis. Mobility engineering and a metal-insulator transition in monolayer MoS2. *Nature materials*, 12(9):815–20, 2013.

[115] E J Meijer, D M de Leeuw, S Setayesh, E van Veenendaal, B H Huisman, P W M Blom, J C Hummelen, U Scherf, J Kadam, and T M Klapwijk. Solution-processed ambipolar organic field-effect transistors and inverters. *Nature materials*, 2(10):678–682, 2003.

[116] Huilong Xu, Sara Fathipour, Erich W. Kinder, Alan C. Seabaugh, and Susan K. Fullerton-Shirey. Reconfigurable Ion Gating of 2H-MoTe2 Field-Effect Transistors Using Poly(ethylene oxide)-CsClO4 Solid Polymer Electrolyte. *ACS Nano*, 9(5):4900–4910, 2015.

[117] Chendong Zhang, Amber Johnson, Chang-Lung Hsu, Lain-Jong Li, and Chih-Kang Shih. Direct Imaging of Band Profile in Single Layer MoS 2 on Graphite: Quasiparticle Energy Gap, Metallic Edge States, and Edge Band Bending. *Nano Letters*, 14(5):2443–2447, may 2014.

[118] Yu Li Huang, Yifeng Chen, Wenjing Zhang, Su Ying Quek, Chang-Hsiao Chen, Lain-Jong Li, Wei-Ting Hsu, Wen-Hao Chang, Yu Jie Zheng, Wei Chen, and Andrew T S Wee. Bandgap tunability at single-layer molybdenum disulphide grain boundaries. *Nature communications*, 6:6298, 2015.

[119] A. R. Klots, A. K. M. Newaz, Bin Wang, D. Prasai, H. Krzyzanowska, Junhao Lin, D. Caudel, N. J. Ghimire, J. Yan, B. L. Ivanov, K. A. Velizhanin, A. Burger, D. G. Mandrus, N. H. Tolk, S. T. Pantelides, and K. I. Bolotin. Probing excitonic states in ultraclean suspended two-dimensional semiconductors by photocurrent spectroscopy. *Scientific Reports*, 4:6608, 2014.

[120] Jana Zaumseil, Richard H. Friend, and Henning Sirringhaus. Spatial control of the recombination zone in an ambipolar light-emitting organic transistor. *Nature Materials*, 5(1):69–74, 2006.

[121] Lampert M.A. and Mark P. *Current Injection in Solids.* Academic Press, New York, 1970.

[122] Pope M. and Swenberg C.E. *Electronic Processes in Organic Crystals and Polymers.* Oxford University Press, New York, 1999.

[123] R. W I De Boer and A. F. Morpurgo. Influence of surface traps on space-charge limited current. *Physical Review B*, 72(7):1–4, 2005.

[124] Weijie Zhao, Zohreh Ghorannevis, Leiqiang Chu, Minglin Toh, Christian Kloc, Ping Heng Tan, and Goki Eda. Evolution of electronic structure in atomically thin sheets of WS2 and WSe2. *ACS Nano*, 7(1):791–797, 2013.

[125] Aaron M. Jones, Hongyi Yu, Nirmal J. Ghimire, Sanfeng Wu, Grant Aivazian, Jason S. Ross, Bo Zhao, Jiaqiang Yan, David G. Mandrus, Di Xiao, Wang Yao, and Xiaodong Xu. Optical generation of excitonic valley coherence in monolayer WSe2. *Nature Nanotechnology*, 8(9):634–638, 2013.

[126] Namphung Peimyoo, Jingzhi Shang, Chunxiao Cong, Xiaonan Shen, Xiangyang Wu, Edwin K L Yeow, and Ting Yu. Nonblinking, intense two-dimensional light emitter: Monolayer WS 2 Triangles. *ACS Nano*, 7(12):10985–10994, 2013.

[127] Keliang He, Nardeep Kumar, Liang Zhao, Zefang Wang, Kin Fai Mak, Hui Zhao, and Jie Shan. Tightly bound excitons in monolayer WSe2. *Physical Review Letters*, 113(2):1–5, 2014.

[128] Rafik Addou, Stephen McDonnell, Diego Barrera, Zaibing Guo, Angelica Azcatl, Jian Wang, Hui Zhu, Christopher L. Hinkle, Manuel Quevedo-Lopez, Husam N. Alshareef, Luigi Colombo, Julia W.P. Hsu, and Robert M. Wallace. Impurities and Electronic Property Variations of Natural MoS2 Crystal Surfaces. *ACS Nano*, 9(9):9124–9133, 2015.

[129] Stephen McDonnell, Rafik Addou, Creighton Buie, Robert M. Wallace, and Christopher L. Hinkle. Defect-DOMINATED DOPING and CONTACT RESISTANCE in MoS2. *ACS Nano*, 8(3):2880–2888, 2014.

[130] Masoud Mahjouri-Samani, Liangbo Liang, Akinola Oyedele, Yong Sung Kim, Mengkun Tian, Nicholas Cross, Kai Wang, Ming Wei Lin, Abdelaziz Boulesbaa, Christopher M. Rouleau, Alexander A.

Puretzky, Kai Xiao, Mina Yoon, Gyula Eres, Gerd Duscher, Bobby G. Sumpter, and David B. Geohegan. Tailoring Vacancies Far beyond Intrinsic Levels Changes the Carrier Type and Optical Response in Monolayer MoSe2-x Crystals. *Nano Letters*, 16(8):5213–5220, 2016.

[131] Haining Wang, Changjian Zhang, and Farhan Rana. Ultrafast dynamics of defect-assisted electron-hole recombination in monolayer MoS2. *Nano Letters*, 15(1):339–345, 2015.

[132] M. Koperski, K. Nogajewski, A. Arora, V. Cherkez, P. Mallet, J. Y. Veuillen, J. Marcus, P. Kossacki, and M. Potemski. Single photon emitters in exfoliated WSe2 structures. *Nature Nanotechnology*, 10(6):503–506, 2015.

[133] Ajit Srivastava, Meinrad Sidler, Adrien V. Allain, Dominik S. Lembke, Andras Kis, and A. Imamoglu. Optically active quantum dots in monolayer WSe 2. *Nature Nanotechnology*, 10(6):491–496, 2015.

[134] Yu Ming He, Genevieve Clark, John R. Schaibley, Yu He, Ming Cheng Chen, Yu Jia Wei, Xing Ding, Qiang Zhang, Wang Yao, Xiaodong Xu, Chao Yang Lu, and Jian Wei Pan. Single quantum emitters in monolayer semiconductors. *Nature Nanotechnology*, 10(6):497–502, 2015.

[135] Chitraleema Chakraborty, Laura Kinnischtzke, Kenneth M. Goodfellow, Ryan Beams, and A. Nick Vamivakas. Voltage-controlled quantum light from an atomically thin semiconductor. *Nature Nanotechnology*, 10(6):507–511, 2015.

[136] Romain Bourrellier, Sophie Meuret, Anna Tararan, Odile Stéphan, Mathieu Kociak, Luiz H.G. Tizei, and Alberto Zobelli. Bright UV single photon emission at point defects in h-BN. *Nano Letters*, 16(7):4317–4321, 2016.

[137] Gabriele Grosso, Hyowon Moon, Benjamin Lienhard, Sajid Ali, Dmitri K. Efetov, Marco M. Furchi, Pablo Jarillo-Herrero, Michael J. Ford, Igor Aharonovich, and Dirk Englund. Tunable and high-purity room temperature single-photon emission from atomic defects in hexagonal boron nitride. *Nature Communications*, 8(1):1–8, 2017.

[138] Masaru Onga, Yijin Zhang, Ryuji Suzuki, and Yoshihiro Iwasa. High circular polarization in electroluminescence from MoSe 2. *Applied Physics Letters*, 073107:2–6, 2016.

[139] Adrien Allain and Andras Kis. Electron and hole mobilities in single-layer WSe2. *ACS Nano*, 8(7):7180–7185, 2014.

[140] Y. J. Zhang, J. T. Ye, Y. Yomogida, T. Takenobu, and Y. Iwasa. Formation of a stable p-n junction in a liquid-gated MoS2 ambipolar transistor. *Nano Letters*, 13(7):3023–3028, 2013.

[141] Shengjun Yuan, Rafael Roldán, M. I. Katsnelson, and Francisco Guinea. Effect of point defects on the optical and transport properties of MoS2 and WS2. *Physical Review B - Condensed Matter and Materials Physics*, 90(4):1–5, 2014.

[142] Ming-Wei Chen, Dmitry Ovchinnikov, Sorin Lazar, Michele Pizzochero, Michael Brian Whitwick, Alessandro Surrente, Michał Baranowski, Oriol Lopez Sanchez, Philippe Gillet, Paulina Plochocka, Oleg V. Yazyev, and Andras Kis. Highly Oriented Atomically Thin Ambipolar MoSe2 Grown by Molecular Beam Epitaxy. *ACS Nano*, 11(6):6355–6361, 2017.

[143] Davide Costanzo, Sanghyun Jo, Helmuth Berger, and Alberto F. Morpurgo. Gate-induced superconductivity in atomically thin MoS2 crystals. *Nature Nanotechnology*, 11(4):339–344, 2016.

[144] Yao Li, Karel-Alexander N. Duerloo, Kerry Wauson, and Evan J. Reed. Structural semiconductor-to-semimetal phase transition in two-dimensional materials induced by electrostatic gating. *Nature Communications*, 7:10671, 2016.

[145] Ying Wang, Jun Xiao, Hanyu Zhu, Yao Li, Yousif Alsaid, King Yan Fong, Yao Zhou, Siqi Wang, Wu Shi, Yuan Wang, Alex Zettl, Evan J. Reed, and Xiang Zhang. Structural phase transition in monolayer MoTe2 driven by electrostatic doping. *Nature*, 550(7677):487–491, 2017.

[146] Ji Young Noh, Hanchul Kim, and Yong Sung Kim. Stability and electronic structures of native defects in single-layer MoS2. *Physical Review B - Condensed Matter and Materials Physics*, 89(20):1–12, 2014.

[147] Bing Huang, Mina Yoon, Bobby G. Sumpter, Su Huai Wei, and Feng Liu. Alloy Engineering of Defect Properties in Semiconductors: Suppression of Deep Levels in Transition-Metal Dichalcogenides. *Physical Review Letters*, 115(12):1–5, 2015.

[148] Rafik Addou, Luigi Colombo, and Robert M. Wallace. Surface Defects on Natural MoS2. *ACS Applied Materials and Interfaces*, 7(22):11921–11929, 2015.

[149] J. M. Ziman. *Electrons and phonons: the theory of transport phenomena in solids.* Clarendon, Oxford, 1960.

[150] G. Grimvall. *The electron-phonon interaction in metals.* North-Holland, Amsterdam, 1981.

[151] G. D. Mahan. *Many-Particle Physics.* Plenum, New York, 3 edition, 2000.

[152] J. Bardeen and W. Shockley. Deformation potentials and mobilities in non-polar crystals. *Phys. Rev.*, 80:72–80, Oct 1950.

[153] W. Shockley and J. Bardeen. Energy bands and mobilities in monatomic semiconductors. *Phys. Rev.*, 77:407–408, Feb 1950.

[154] L. Pietronero, S. Strässler, H. R. Zeller, and M. J. Rice. Electrical conductivity of a graphite layer. *Phys. Rev. B*, 22:904–910, Jul 1980.

[155] Thibault Sohier, Matteo Calandra, Cheol-Hwan Park, Nicola Bonini, Nicola Marzari, and Francesco Mauri. Phonon-limited resistivity of graphene by first-principles calculations: Electron-phonon interactions, strain-induced gauge field, and boltzmann equation. *Phys. Rev. B*, 90:125414, Sep 2014.

[156] M.A.H. Vozmediano, M.I. Katsnelson, and F. Guinea. Gauge fields in graphene. *Physics Reports*, 496(4):109 – 148, 2010.

[157] S. Engelsberg and J. R. Schrieffer. Coupled electron-phonon system. *Phys. Rev.*, 131:993–1008, Aug 1963.

[158] E.G Maksimov and S.V Shulga. Nonadiabatic effects in optical phonon self-energy. *Solid State Communications*, 97(7):553 – 560, 1996.

[159] P Bogulsawski and J Mycielski. Is the deformation potential in semiconductors screened by free carriers? *Journal of Physics C: Solid State Physics*, 10(13):2413, 1977.

[160] F. S. Khan and P. B. Allen. Deformation potentials and electron-phonon scattering: Two new theorems. *Phys. Rev. B*, 29:3341–3349, Mar 1984.

[161] E. Kartheuser and S. Rodriguez. Deformation potentials and the electron-phonon interaction in metals. *Phys. Rev. B*, 33:772–779, Jan 1986.

[162] Andrea C. Ferrari. Raman spectroscopy of graphene and graphite: Disorder, electron–phonon coupling, doping and nonadiabatic effects. *Solid State Communications*, 143(1):47–57, July 2007.

[163] Andrea C. Ferrari and Denis M. Basko. Raman spectroscopy as a versatile tool for studying the properties of graphene. *Nature Nanotechnology*, 8(4):235–246, April 2013.

[164] Simone Pisana, Michele Lazzeri, Cinzia Casiraghi, Kostya S. Novoselov, A. K. Geim, Andrea C. Ferrari, and Francesco Mauri. Breakdown of the adiabatic born–oppenheimer approximation in graphene. *Nature Materials*, 6:198, 02 2007.

[165] D. A. Kirzhnits, E. G. Maksimov, and D. I. Khomskii. The description of superconductivity in terms of dielectric response function. *Journal of Low Temperature Physics*, 10(1):79–93, January 1973.

[166] J. L. M. van Mechelen, D. van der Marel, C. Grimaldi, A. B. Kuzmenko, N. P. Armitage, N. Reyren, H. Hagemann, and I. I. Mazin. Electron-Phonon Interaction and Charge Carrier Mass Enhancement in ${\mathrm{SrTiO}}_{3}$. *Physical Review Letters*, 100(22):226403, June 2008.

[167] Z. Wang, S. McKeown Walker, A. Tamai, Y. Wang, Z. Ristic, F. Y. Bruno, A. de la Torre, S. Riccò, N. C. Plumb, M. Shi, P. Hlawenka, J. Sánchez-Barriga, A. Varykhalov, T. K. Kim, M. Hoesch, P. D. C. King, W. Meevasana, U. Diebold, J. Mesot, B. Moritz, T. P. Devereaux, M. Radovic, and F. Baumberger. Tailoring the nature and strength of electron–phonon interactions in the srtio$_3$(001) 2d electron liquid. *Nature Materials*, 15:835, 04 2016.

[168] Carla Verdi, Fabio Caruso, and Feliciano Giustino. Origin of the crossover from polarons to fermi liquids in transition metal oxides. *Nature Communications*, 8:15769, 06 2017.

[169] Thibault Sohier, Matteo Calandra, and Francesco Mauri. Density functional perturbation theory for gated two-dimensional heterostructures: Theoretical developments and application to flexural phonons in graphene. *Physical Review B*, 96(7):075448, may 2017.

[170] J T Ye, Y J Zhang, R Akashi, M S Bahramy, R Arita, and Y Iwasa. Superconducting Dome in a Gate-Tuned Band Insulator. *Science*, 338(6111):1193–1196, nov 2012.

[171] Jianming Lu, Oleksandr Zheliuk, Qihong Chen, Inge Leermakers, Nigel E. Hussey, Uli Zeitler, and Jianting Ye. Full superconducting dome of strong Ising protection in gated monolayer WS2. *Proceedings of the National Academy of Sciences*, 115(14):3551–3556, April 2018.

[172] Erik Piatti, Domenico De Fazio, Dario Daghero, Srinivasa Reddy Tamalampudi, Duhee Yoon, Andrea C. Ferrari, and Renato S. Gonnelli. Multi-valley superconductivity in ion-gated mos2 layers. *Nano Letters*, 18(8):4821–4830, 2018. PMID: 29949374.

[173] Yoshiaki Hamaue and Ryôzô Aoki. Effects of organic intercalation on lattice vibrations and superconducting properties of 2h–nbs$_2$. *Journal of the Physical Society of Japan*, 55(4):1327–1335, 1986.

[174] I. Guillamón, H. Suderow, S. Vieira, L. Cario, P. Diener, and P. Rodière. Superconducting density of states and vortex cores of 2h-nbs$_2$. *Phys. Rev. Lett.*, 101:166407, Oct 2008.

[175] Xiaoxiang Xi, Zefang Wang, Weiwei Zhao, Ju-Hyun Park, Kam Tuen Law, Helmuth Berger, László Forró, Jie Shan, and Kin Fai Mak. Ising pairing in superconducting nbse2 atomic layers. *Nature Physics*, 12:139, 11 2016.

[176] Miguel M. Ugeda, Aaron J. Bradley, Yi Zhang, Seita Onishi, Yi Chen, Wei Ruan, Claudia Ojeda-Aristizabal, Hyejin Ryu, Mark T. Edmonds, Hsin-Zon Tsai, Alexander Riss, Sung-Kwan Mo, Dunghai Lee, Alex Zettl, Zahid Hussain, Zhi-Xun Shen, and Michael F. Crommie. Characterization of collective ground states in single-layer nbse2. *Nature Physics*, 12:92, 11 2016.

[177] A. W. Tsen, B. Hunt, Y. D. Kim, Z. J. Yuan, S. Jia, R. J. Cava, J. Hone, P. Kim, C. R. Dean, and A. N. Pasupathy. Nature of the quantum metal in a two-dimensional crystalline superconductor. *Nature Physics*, 12:208, 12 2016.

[178] Y. J. Zhang, T. Oka, R. Suzuki, J. T. Ye, and Y. Iwasa. Electrically Switchable Chiral Light-Emitting Transistor. *Science*, 344(6185):725–728, May 2014.

[179] Nicolas Ubrig, Sanghyun Jo, Helmuth Berger, Alberto F. Morpurgo, and Alexey B. Kuzmenko. Scanning photocurrent microscopy reveals electron-hole asymmetry in ionic liquid-gated WS2 transistors. *Applied Physics Letters*, 104(17):171112, April 2014.

[180] Sanghyun Jo, Davide Costanzo, Helmuth Berger, and Alberto F. Morpurgo. Electrostatically Induced Superconductivity at the Surface of WS2. *Nano Letters*, 15(2):1197–1202, February 2015.

[181] Yijin Zhang, Jianting Ye, Yusuke Matsuhashi, and Yoshihiro Iwasa. Ambipolar MoS2 Thin Flake Transistors. *Nano Letters*, 12(3):1136–1140, March 2012.

[182] Davide Costanzo, Sanghyun Jo, Helmuth Berger, and Alberto F. Morpurgo. Gate-induced superconductivity in atomically thin MoS2 crystals. *Nature Nanotechnology*, 11(4):339–344, April 2016.

[183] Ignacio Gutiérrez-Lezama, Bojja Aditya Reddy, Nicolas Ubrig, and Alberto F. Morpurgo. Electroluminescence from indirect band gap semiconductor ReS 2. *2D Materials*, 3(4):045016, 2016.

[184] Changgu Lee, Hugen Yan, Louis E. Brus, Tony F. Heinz, James Hone, and Sunmin Ryu. Anomalous Lattice Vibrations of Single- and Few-Layer MoS2. *ACS Nano*, 4(5):2695–2700, May 2010.

[185] A Molina-Sánchez and L Wirtz. Phonons in single-layer and few-layer mos2 and ws2. *Physical Review B*, 84(15):155413, oct 2011.

[186] Ayse Berkdemir, Humberto R. Gutiérrez, Andrés R. Botello-Méndez, Néstor Perea-López, Ana Laura Elías, Chen-Ing Chia, Bei Wang, Vincent H. Crespi, Florentino López-Urías, Jean-Christophe Charlier, Humberto Terrones, and Mauricio Terrones. Identification of individual and few layers of WS2 using Raman Spectroscopy. *Scientific Reports*, 3:1755, April 2013.

[187] H. Sahin, S. Tongay, S. Horzum, W. Fan, J. Zhou, J. Li, J. Wu, and F. M. Peeters. Anomalous Raman spectra and thickness-dependent electronic properties of wse2. *Physical Review B*, 87(16):165409, April 2013.

[188] R. Saito, Y. Tatsumi, S. Huang, X. Ling, and M. S. Dresselhaus. Raman spectroscopy of transition metal dichalcogenides. *Journal of Physics: Condensed Matter*, 28(35):353002, 2016.

[189] H. Terrones, E. Del Corro, S. Feng, J. M. Poumirol, D. Rhodes, D. Smirnov, N. R. Pradhan, Z. Lin, M. a. T. Nguyen, A. L. Elías, T. E. Mallouk, L. Balicas, M. A. Pimenta, and M. Terrones. New First Order Raman-active Modes in Few Layered Transition Metal Dichalcogenides. *Scientific Reports*, 4:4215, February 2014.

[190] A. A. Mitioglu, P. Plochocka, G. Deligeorgis, S. Anghel, L. Kulyuk, and D. K. Maude. Second-order resonant Raman scattering in single-layer tungsten disulfide ws2. *Physical Review B*, 89(24):245442, June 2014.

[191] A. Carvalho, R. M. Ribeiro, and A. H. Castro Neto. Band nesting and the optical response of two-dimensional semiconducting transition metal dichalcogenides. *Physical Review B*, 88(11):115205, September 2013.

[192] The values of carrier density are estimated using values of the capacitance per unit area obtained from previous experiments (in which the capacitance was obtained using the Hall effect to measure the density of accumulated charge). These past experiments show that in ionic-liquid gated transistors on mono and bilayer semiconducting TMDS –in the range of density explored here– the capacitance value is largely determined by the density of states (i.e., taking into account the quantum capacitance is essential). Since the density of states is different for mono and bilayers and –once the thickness is fixed– for the conduction and valence bands, different values for C have to be used. At room temperature, the capacitance does not depend much on the specific compound considered and here we use the values measured on $\mathrm{WSe_2}$ mono and bilayers, which are: $\mathrm{C}^e_{\mathrm{ML}} = 7.3\ \mu\mathrm{F\,cm^{-2}}$; $\mathrm{C}^h_{\mathrm{ML}} = 17\ \mu\mathrm{F\,cm^{-2}}$; $\mathrm{C}^e_{\mathrm{BL}} = 22.8\ \mu\mathrm{F\,cm^{-2}}$; $\mathrm{C}^h_{\mathrm{BL}} = 24\ \mu\mathrm{F\,cm^{-2}}$ (the subscript ML and BL refer to mono and bilayer; the superscript e and h indicates the value to use for accumulation of electrons and holes, respectively).

[193] In view of the microscopic complexity of the resonant process from which the 2LA(M) Raman peak originates, and of the fact that –as it will be discussed explicitly in Section 6.3 – our main interest here is on long-wavelength phonons, we will not discuss the behavior of the 2LA(M) Raman peak. As a only remark, note that –just like for the $\mathrm{A_{1g}}$ mode– the LA(M) mode corresponds to an out-of-plane motion of the atoms in the lattice (see figure 6.1(c)), and a finite electron-phonon coupling is present, as demonstrated by the sensitivity of the mode frequency to the introduction of charge carriers.

[194] Biswanath Chakraborty, Achintya Bera, D. V. S. Muthu, Somnath Bhowmick, U. V. Waghmare, and A. K. Sood. Symmetry-dependent phonon renormalization in monolayer mos2 transistor. *Physical Review B*, 85(16):161403(R), April 2012.

[195] Xin Lu, M. I. B. Utama, Xingzhi Wang, Weigao Xu, Weijie Zhao, Man Hon Samuel Owen, and Qihua Xiong. Gate-Tunable Resonant Raman Spectroscopy of Bilayer MoS2. *Small*, 13(35):1701039, September 2017.

[196] Alejandro Molina-Sánchez, Kerstin Hummer, and Ludger Wirtz. Vibrational and optical properties of mos_2: From monolayer to bulk. *Surface Science Reports*, 70(4):554 – 586, 2015.

[197] Duy Le, Alexei Barinov, Edwin Preciado, Miguel Isarraraz, Iori Tanabe, Takashi Komesu, Conrad Troha, Ludwig Bartels, Talat S Rahman, and Peter A Dowben. Spin–orbit coupling in the band structure of monolayer wse_2. *Journal of Physics: Condensed Matter*, 27(18):182201, 2015.

[198] Andor Kormányos, Guido Burkard, Martin Gmitra, Jaroslav Fabian, Viktor Zólyomi, Neil D Drummond, and Vladimir Fal'ko. $\mathrm{k} \cdot \mathrm{p}$ theory for two-dimensional transition metal dichalcogenide semiconductors. *2D Materials*, 2(2):022001, 2015.

[199] Hongtao Yuan, Zhongkai Liu, Gang Xu, Bo Zhou, Sanfeng Wu, Dumitru Dumcenco, Kai Yan, Yi Zhang, Sung-Kwan Mo, Pavel Dudin, Victor Kandyba, Mikhail Yablonskikh, Alexei Barinov, Zhixun Shen, Shoucheng Zhang, Yingsheng Huang, Xiaodong Xu, Zahid Hussain, Harold Y. Hwang, Yi Cui, and Yulin Chen. Evolution of the valley position in bulk transition-metal chalcogenides and their monolayer limit. *Nano Letters*, 16(8):4738–4745, 2016. PMID: 27357620.

[200] Luciano Ortenzi, Luciano Pietronero, and Emmanuele Cappelluti. Zero-point motion and direct-indirect band-gap crossover in layered transition-metal dichalcogenides. *Physical Review B*, 98:195313, Nov 2018.

[201] Wencan Jin, Po-Chun Yeh, Nader Zaki, Datong Zhang, Jerzy T. Sadowski, Abdullah Al-Mahboob, Arend M. van der Zande, Daniel A. Chenet, Jerry I. Dadap, Irving P. Herman, Peter Sutter, James Hone, and Richard M. Osgood. Direct measurement of the thickness-dependent electronic band structure of mos_2 using angle-resolved photoemission spectroscopy. *Phys. Rev. Lett.*, 111:106801, Sep 2013.

[202] Jill A. Miwa, Søren Ulstrup, Signe G. Sørensen, Maciej Dendzik, Antonija Grubisc Cabo, Marco Bianchi, Jeppe Vang Lauritsen, and Philip Hofmann. Electronic structure of epitaxial single-layer mos$_2$. *Phys. Rev. Lett.*, 114:046802, Jan 2015.

[203] Maciej Dendzik, Matteo Michiardi, Charlotte Sanders, Marco Bianchi, Jill A. Miwa, Signe S. Grønborg, Jeppe V. Lauritsen, Albert Bruix, Bjørk Hammer, and Philip Hofmann. Growth and electronic structure of epitaxial single-layer ws$_2$ on au(111). *Phys. Rev. B*, 92:245442, Dec 2015.

[204] C Kastl, C T Chen, R J Koch, B Schuler, T R Kuykendall, A Bostwick, C Jozwiak, T Seyller, E Rotenberg, A Weber-Bargioni, S Aloni, and A M Schwartzberg. Multimodal spectromicroscopy of monolayer ws 2 enabled by ultra-clean van der waals epitaxy. *2D Materials*, 5(4):045010, 2018.

[205] Hugo Henck, Zeineb Ben Aziza, Debora Pierucci, Feriel Laourine, Francesco Reale, Pawel Palczynski, Julien Chaste, Mathieu G. Silly, Francois Bertran, Patrick Le Fèvre, Emmanuel Lhuillier, Taro Wakamura, Cecilia Mattevi, Julien E. Rault, Matteo Calandra, and Abdelkarim Ouerghi. Electronic band structure of two-dimensional ws$_2$/graphene van der waals heterostructures. *Phys. Rev. B*, 97:155421, Apr 2018.

[206] Yi Zhang, Miguel M. Ugeda, Chenhao Jin, Su-Fei Shi, Aaron J. Bradley, Ana Martín-Recio, Hyejin Ryu, Jonghwan Kim, Shujie Tang, Yeongkwan Kim, Bo Zhou, Choongyu Hwang, Yulin Chen, Feng Wang, Michael F. Crommie, Zahid Hussain, Zhi-Xun Shen, and Sung-Kwan Mo. Electronic Structure, Surface Doping, and Optical Response in Epitaxial WSe2 thin Films. *Nano Letters*, 16(4):2485–2491, 2016.

[207] Michele Lazzeri and Francesco Mauri. Nonadiabatic kohn anomaly in a doped graphene monolayer. *Phys. Rev. Lett.*, 97:266407, Dec 2006.

[208] A. Marco Saitta, Michele Lazzeri, Matteo Calandra, and Francesco Mauri. Giant nonadiabatic effects in layer metals: Raman spectra of intercalated graphite explained. *Phys. Rev. Lett.*, 100:226401, Jun 2008.

[209] Matteo Calandra, Gianni Profeta, and Francesco Mauri. Adiabatic and nonadiabatic phonon dispersion in a wannier function approach. *Phys. Rev. B*, 82:165111, Oct 2010.

[210] F. Marsiglio, R. Akis, and J. P. Carbotte. Phonon self-energy effects due to superconductivity: A real-axis formulation. *Phys. Rev. B*, 45:9865–9871, May 1992.

[211] Stefano Baroni, Stefano de Gironcoli, Andrea Dal Corso, and Paolo Giannozzi. Phonons and related crystal properties from density-functional perturbation theory. *Rev. Mod. Phys.*, 73:515–562, Jul 2001.

[212] Nicola Marzari, David Vanderbilt, Alessandro De Vita, and M. C. Payne. Thermal contraction and disordering of the al(110) surface. *Phys. Rev. Lett.*, 82:3296–3299, Apr 1999.

[213] Shiyuan Gao and Li Yang. Renormalization of the quasiparticle band gap in doped two-dimensional materials from many-body calculations. *Phys. Rev. B*, 96:155410, Oct 2017.

[214] Jyoti Katoch, Søren Ulstrup, Roland J. Koch, Simon Moser, Kathleen M. McCreary, Simranjeet Singh, Jinsong Xu, Berend T. Jonker, Roland K. Kawakami, Aaron Bostwick, Eli Rotenberg, and Chris Jozwiak. Giant spin-splitting and gap renormalization driven by trions in single-layer ws_2/h-bn heterostructures. *Nature Physics*, 14(4):355–359, 2018.

[215] Mingu Kang, Beomyoung Kim, Sae Hee Ryu, Sung Won Jung, Jimin Kim, Luca Moreschini, Chris Jozwiak, Eli Rotenberg, Aaron Bostwick, and Keun Su Kim. Universal mechanism of band-gap engineering in transition-metal dichalcogenides. *Nano Letters*, 17(3):1610–1615, 2017. PMID: 28118710.

[216] Erik Piatti, Davide Romanin, and Renato S Gonnelli. Mapping multi-valley Lifshitz transitions induced by field-effect doping in strained {MoS}2 nanolayers. *Journal of Physics: Condensed Matter*, 31(11):114002, jan 2019.

[217] S. Lebègue and O. Eriksson. Electronic structure of two-dimensional crystals from ab initio theory. *Phys. Rev. B*, 79:115409, Mar 2009.

[218] Yuki Nakata, Katsuaki Sugawara, Satoru Ichinokura, Yoshinori Okada, Taro Hitosugi, Takashi Koretsune, Keiji Ueno, Shuji Hasegawa, Takashi Takahashi, and Takafumi Sato. Anisotropic band splitting in monolayer nbse2: implications for superconductivity and charge density wave. *npj 2D Materials and Applications*, 2(1):12, 2018.

[219] J. M. An and W. E. Pickett. Superconductivity of mgb$_2$: Covalent bonds driven metallic. *Phys. Rev. Lett.*, 86:4366–4369, May 2001.

[220] K S Novoselov and A H Castro Neto. Two-dimensional crystals-based heterostructures: materials with tailored properties. *Physica Scripta*, 2012(T146):14006, 2012.

[221] Giuseppe Iannaccone, Francesco Bonaccorso, Luigi Colombo, and Gianluca Fiori. Quantum engineering of transistors based on 2D materials heterostructures. *Nature Nanotechnology*, 13(3):183–191, 2018.

[222] Lin Wang, Ignacio Gutiérrez-Lezama, Céline Barreteau, Nicolas Ubrig, Enrico Giannini, and Alberto F Morpurgo. Tuning magnetotransport in a compensated semimetal at the atomic scale. *Nature Communications*, 6:8892, nov 2015.

[223] Zaiyao Fei, Tauno Palomaki, Sanfeng Wu, Wenjin Zhao, Xinghan Cai, Bosong Sun, Paul Nguyen, Joseph Finney, Xiaodong Xu, and David H Cobden. Edge conduction in monolayer WTe2. *Nature Physics*, 13(7):677–682, jul 2017.

[224] Cheng Gong, Lin Li, Zhenglu Li, Huiwen Ji, Alex Stern, Yang Xia, Ting Cao, Wei Bao, Chenzhe Wang, Yuan Wang, Z. Q. Qiu, R. J. Cava, Steven G. Louie, Jing Xia, and Xiang Zhang. Discovery of intrinsic ferromagnetism in two-dimensional van der Waals crystals. *Nature*, 546(7657):265–269, 2017.

[225] Bevin Huang, Genevieve Clark, Efrén Navarro-Moratalla, Dahlia R Klein, Ran Cheng, Kyle L Seyler, Ding Zhong, Emma Schmidgall, Michael A McGuire, David H Cobden, Wang Yao, Di Xiao, Pablo Jarillo-Herrero, and Xiaodong Xu. Layer-dependent ferromagnetism in a van der Waals crystal down to the monolayer limit. *Nature*, 546(7657):270–273, jun 2017.

[226] Y. Cao, A. Mishchenko, G. L. Yu, E. Khestanova, A. P. Rooney, E. Prestat, A. V. Kretinin, P. Blake, M. B. Shalom, C. Woods, J. Chapman, G. Balakrishnan, I. V. Grigorieva, K. S. Novoselov, B. A. Piot, M. Potemski, K. Watanabe, T. Taniguchi, S. J. Haigh, A. K. Geim, and R. V. Gorbachev. Quality Heterostructures from Two-Dimensional Crystals Unstable in Air by Their Assembly in Inert Atmosphere. *Nano Letters*, 15(8):4914–4921, 2015.

[227] Zhe Wang, Dong-Keun Ki, Hua Chen, Helmuth Berger, Allan H MacDonald, and Alberto F Morpurgo. Strong interface-induced

spin–orbit interaction in graphene on WS2. *Nature Communications*, 6:8339, sep 2015.

[228] Feng Wang, Zhenxing Wang, Qisheng Wang, Humberto Terrones, Ruitao Lv, Mauricio Terrones, Wenjing Zhang, Qixing Wang, Yu Chen, Zhong Lin, Bruno R Carvalho, Ethan Kahn, Ruitao Lv, Rahul Rao, and Humberto Terrones. Defect engineering of two-dimensional transition metal dichalcogenides. *2D Materials*, 3(2):1–21, 2016.

[229] The case of a band alignment resulting in either conduction or the valence bands of the two monolayers that are degenerate in energy is not considered here. Despite providing even more possibilities to control the interfacial properties, that case is more complex because the hybridization of the states in the degenerate bands of the two materials can not be neglected.

[230] Xiaoping Hong, Jonghwan Kim, Su-Fei Shi, Yu Zhang, Chenhao Jin, Yinghui Sun, Sefaattin Tongay, Junqiao Wu, Yanfeng Zhang, and Feng Wang. Ultrafast charge transfer in atomically thin MoS2/WS2 heterostructures. *Nature Nanotechnology*, 9:682, aug 2014.

[231] Jonghwan Kim, Chenhao Jin, Bin Chen, Hui Cai, Tao Zhao, Puiyee Lee, Salman Kahn, Kenji Watanabe, Takashi Taniguchi, Sefaattin Tongay, Michael F Crommie, and Feng Wang. Observation of ultralong valley lifetime in WSe2/MoS2 heterostructures. *Science Advances*, 3(7):e1700518, jul 2017.

[232] Haiming Zhu, Jue Wang, Zizhou Gong, Young Duck Kim, James Hone, and X. Y. Zhu. Interfacial Charge Transfer Circumventing Momentum Mismatch at Two-Dimensional van der Waals Heterojunctions. *Nano Letters*, 17(6):3591–3598, 2017.

[233] Hidekazu Shimotani, Haruhiko Asanuma, Jun Takeya, and Yoshihiro Iwasa. Electrolyte-gated charge accumulation in organic single crystals. *Applied Physics Letters*, 89(20), 2006.

[234] Wei Xie and C Daniel Frisbie. Organic Electrical Double Layer Transistors Based on Rubrene Single Crystals: Examining Transport at High Surface Charge Densities. *The Journal of Physical Chemistry C*, 115(29):14360–14368, jul 2011.

[235] Evgeniy Ponomarev, Arpád Pasztor, Adrien Waelchli, Alessandro Scarfato, Nicolas Ubrig, Christoph Renner, and Alberto F Mor-

purgo. Hole Transport in Exfoliated Monolayer MoS2. *ACS Nano*, 12(3):2669–2676, mar 2018.

[236] P J Zomer, S P Dash, N Tombros, and B J van Wees. A transfer technique for high mobility graphene devices on commercially available hexagonal boron nitride. *Applied Physics Letters*, 99(23):232104, dec 2011.

[237] Miguel M Ugeda, Aaron J Bradley, Su-Fei Shi, Felipe H da Jornada, Yi Zhang, Diana Y Qiu, Wei Ruan, Sung-Kwan Mo, Zahid Hussain, Zhi-Xun Shen, Feng Wang, Steven G Louie, and Michael F Crommie. Giant bandgap renormalization and excitonic effects in a monolayer transition metal dichalcogenide semiconductor. *Nature Materials*, 13(12):1091–1095, dec 2014.

[238] Yu Li Huang, Zijing Ding, Wenjing Zhang, Yung Huang Chang, Yumeng Shi, Lain Jong Li, Zhibo Song, Yu Jie Zheng, Dongzhi Chi, Su Ying Quek, and Andrew T.S. Wee. Gap states at low-angle grain boundaries in monolayer tungsten diselenide. *Nano Letters*, 16(6):3682–3688, 2016.

[239] Chendong Zhang, Chih Piao Chuu, Xibiao Ren, Ming Yang Li, Lain Jong Li, Chuanhong Jin, Mei Yin Chou, and Chih Kang Shih. Interlayer couplings, Moire patterns, and 2D electronic superlattices in MoS2/WSe2 hetero-bilayers. *Sci. Adv.*, 3(1):1–8, 2017.

[240] Matthew Z. Bellus, Frank Ceballos, Hsin Ying Chiu, and Hui Zhao. Tightly Bound Trions in Transition Metal Dichalcogenide Heterostructures. *ACS Nano*, 9(6):6459–6464, 2015.

[241] Pasqual Rivera, Kyle L Seyler, Hongyi Yu, John R Schaibley, Jiaqiang Yan, David G Mandrus, Wang Yao, and Xiaodong Xu. Valley-polarized exciton dynamics in a 2D semiconductor heterostructure. *Science*, 351(6274):688–691, feb 2016.

[242] Chul-Ho Lee, Gwan-Hyoung Lee, Arend M. van der Zande, Wenchao Chen, Yilei Li, Minyong Han, Xu Cui, Ghidewon Arefe, Colin Nuckolls, Tony F. Heinz, Jing Guo, James Hone, and Philip Kim. Atomically thin p–n junctions with van der Waals heterointerfaces. *Nature Nanotechnology*, 9(9):676–681, 2014.

[243] David A. B. Miller, D. Chemla, T. Damen, A. Gossard, W. Wiegmann, T. Wood, and C. Burrus. Electric field dependence of optical

absorption near the band gap of quantum-well structures. *Physical Review B*, 32(2):1043–1060, 1985.

[244] R T Collins, K v. Klitzing, and K Ploog. Photocurrent spectroscopy of GaAs/AlGaAs quantum wells in an electric field. *Physical Review B*, 33(6):4378–4381, mar 1986.

[245] Kyle L. Seyler, Pasqual Rivera, Hongyi Yu, Nathan P. Wilson, Essance L. Ray, David G. Mandrus, Jiaqiang Yan, Wang Yao, and Xiaodong Xu. Signatures of moiré-trapped valley excitons in MoSe 2 /WSe 2 heterobilayers. *Nature*, 567(7746):66–70, 2019.

[246] Kha Tran, Galan Moody, Fengcheng Wu, Xiaobo Lu, Junho Choi, Kyounghwan Kim, Amritesh Rai, Daniel A. Sanchez, Jiamin Quan, Akshay Singh, Jacob Embley, André Zepeda, Marshall Campbell, Travis Autry, Takashi Taniguchi, Kenji Watanabe, Nanshu Lu, Sanjay K. Banerjee, Kevin L. Silverman, Suenne Kim, Emanuel Tutuc, Li Yang, Allan H. MacDonald, and Xiaoqin Li. Evidence for moiré excitons in van der Waals heterostructures. *Nature*, 567(7746):71–75, 2019.

[247] Chenhao Jin, Emma C. Regan, Aiming Yan, M. Iqbal Bakti Utama, Danqing Wang, Sihan Zhao, Ying Qin, Sijie Yang, Zhiren Zheng, Shenyang Shi, Kenji Watanabe, Takashi Taniguchi, Sefaattin Tongay, Alex Zettl, and Feng Wang. Observation of moiré excitons in WSe 2 /WS 2 heterostructure superlattices. *Nature*, 567(7746):76–80, 2019.

[248] Evgeny M. Alexeev, David A. Ruiz-Tijerina, Mark Danovich, Matthew J. Hamer, Daniel J. Terry, Pramoda K. Nayak, Seongjoon Ahn, Sangyeon Pak, Juwon Lee, Jung Inn Sohn, Maciej R. Molas, Maciej Koperski, Kenji Watanabe, Takashi Taniguchi, Kostya S. Novoselov, Roman V. Gorbachev, Hyeon Suk Shin, Vladimir I. Fal'ko, and Alexander I. Tartakovskii. Resonantly hybridized excitons in moiré superlattices in van der Waals heterostructures. *Nature*, 567(7746):81–86, 2019.

[249] G. W. Mudd, M. R. Molas, X. Chen, V. Zólyomi, K. Nogajewski, Z. R. Kudrynskyi, Z. D. Kovalyuk, G. Yusa, O. Makarovsky, L. Eaves, M. Potemski, V. I. Fal'Ko, and A. Patanè. The direct-to-indirect band gap crossover in two-dimensional van der Waals Indium Selenide crystals. *Scientific Reports*, 6:1–10, 2016.

[250] Denis A. Bandurin, Anastasia V. Tyurnina, Geliang L. Yu, Artem Mishchenko, Viktor Zólyomi, Sergey V. Morozov, Roshan Krishna

Kumar, Roman V. Gorbachev, Zakhar R. Kudrynskyi, Sergio Pezzini, Zakhar D. Kovalyuk, Uli Zeitler, Konstantin S. Novoselov, Amalia Patanè, Laurence Eaves, Irina V. Grigorieva, Vladimir I. Fal'Ko, Andre K. Geim, and Yang Cao. High electron mobility, quantum Hall effect and anomalous optical response in atomically thin InSe. *Nature Nanotechnology*, 12(3):223–227, 2017.